

**An experimental and numerical investigation on damage evolution
and ductile fracture mechanism of aluminum alloy**

A dissertation submitted to
The University of Tokushima
for the degree of
Doctor of Engineering Science

By
Junhang Guo
The University of Tokushima
June 2013

Abstract

for thesis entitled

An experimental and numerical investigation on damage evolution and ductile fracture mechanism of aluminum alloy

submitted by

Junhang Guo

for the degree of Doctor of Engineering Science

at the University of Tokushima

in June 2013

The aluminum alloy has been used widely during the past decade in many fields for media strength and good formability. During manufacturing and applying, a variety of problems may be caused by fracture, so its ductile fracture mechanism is still a hot spot. The fracture can not be totally explained by the classic damage constitutive models, reflecting that the damage evolution and ductile fracture mechanism of metal under complex loading is insufficient. The damage evolution and ductile fracture mechanism under plastic deformation are systematic studied by theoretical analysis, numerical simulations and experimental study for Al-alloy 5052BD-H14 and 5052P-H34, combining with the latest research results in the continuum damage mechanics.

In chapter 1, both the research background and purpose of this study will be introduced. The constitutive model is the fundamental to deal with its mechanics behavior, while the fracture

criterion is the key technique to judge fracture. So, the conventional ductile fracture criteria are reviewed. Then the state of damage mechanics for metals based on $I_1 - J_2 - J_3$ framework is briefly reviewed. The main research contents and outline are also given in this chapter.

In chapter 2, by analyzing the behavior of metal containing voids under tension and shear deformation, the applicability of original Rousselier model is discussed. A modified Rousselier model is proposed by incorporating the recent extended damage evolution model by Nahshon and Hutchinson, in which the non-dimensional metric $\omega(\underline{\underline{\sigma}})$ (or Lode parameter) and the shear damage coefficient k_ω are employed. The physical meaning of the new damage evolution rule will also be interpreted in theory of probability. The analytical solution of the modified damage evolution equation under shear was obtained, and its ability to describe shear fracture of material is discussed.

In chapter 3, the numerical implementation of modified Rousselier model in finite element analysis (FEA) will be conducted. Firstly, the backward Euler scheme based stress integration algorithm will be briefly developed within computational plasticity framework to solve the proposed model and the kernel derivation is carried out. Secondly, the integration algorithm is implemented and embedded into the commercial finite element software Abaqus/Explicit via its user material subroutine interface VUMAT by using Fortran coding language. Thirdly, some benchmark simulations will also be conducted to verify the stress integration algorithm and correspondingly developed program.

In chapter 4, the tensile tests of smooth round bar and notched round bars of Al-alloy 5052BD-H14 with different sizes were performed and the ductile fracture mechanism was analyzed by the macroscopic fracture phenomenon via scanning electron microscope. The mechanism can be

concluded that the material failure under tension is caused by the nucleation, growth and coalescence of some micro-voids and micro-cracks. While for shear specimen, a shear fracture mechanism combining with void deformation was found. So the kernel of damage evolution is the mechanical behavior of micro-voids under complex stress state. Consequently, the material parameters of the classical Rousselier model were identified by an inverse method using these experimental data. A shear test was also performed to calibrate the new shear damage coefficient in the modified Rousselier model. For the shear test, the simulations show that although shear failure can be predicted by the Rousselier model, the ductility was over-estimated. However, the modified Rousselier model can give more accurate results. The simulations on uniaxial tension of the round bars also confirm that the modified Rousselier model can well predict the cup-cone fracture mode. The results indicate that the Lode parameter in the new damage evolution model is important to capture the cup-cone fracture mode transition.

In chapter 5, the ductile analysis of Al-alloy 5052P-H34 under different loading will be carried out by both physical experiments and numerical simulations. The physical failure mode was concluded and fracture mechanism was analyzed. Consequently, the material parameters were identified by an inverse method using these experimental data. A shear test was performed to calibrate the new shear damage coefficient k_{ω} . The Sandia test was also performed to verify the model's applicability. The crack path was investigated by the modified model, the results show that the fracture process and crack propagation under complex loading can be predicted by the modified model.

In conclusion, the ductile fracture mechanism of Al-alloy 5052BD-H14 and 5052P-H34 are studied by a modified Rousselier mode. The applicability of this model on shear failure is enhanced

by the new damage evolution rule in which possible link-up of nearby voids under shear stress is considered. The simulation results show that the modified model can give more accurate results for both of the tension and shear failure.

Keywords: Damage evolution; Lode parameter; Ductile fracture; Numerical simulation; Aluminum alloy

CONTENTS

Chapter 1 Introduction.....	- 1 -
1.1 Research background and significance.....	- 1 -
1.2 Review of ductile fracture models.....	- 2 -
1.2.1 Classical fracture mechanics models.....	- 3 -
1.2.2 Conventional continuum mechanics models.....	- 3 -
1.2.3 Micro mechanical models.....	- 4 -
1.2.4 Damage mechanics models.....	- 6 -
1.3 State of damage mechanics based on I_1 - J_2 - J_3 framework.....	- 7 -
1.3.1 Plasticity theory concerning triaxiality and Lode parameter.....	- 8 -
1.3.2 Damage theory concerning triaxiality and Lode parameter.....	- 10 -
1.4 Thesis organization.....	- 12 -
Chapter 2 Modified Rousselier model.....	14
2.1 Introduction of the original Rousselier damage model.....	14
2.1.1 Yield function.....	14
2.1.2 Hooke's Law.....	17
2.1.3 Flow rule.....	17
2.1.4 Damage evolution's law.....	17
2.2 The modified Rousselier damage model.....	19
2.2.1 The Lode angle and shear metric of stress tensor.....	20
2.2.2 The non-dimensional metric of stress.....	22
2.2.3 The distribution of shear metric under plane stress.....	23
2.2.4 The modified Rousselier model concerning shear failure.....	25
2.3 The physical meaning of the damage evolution rule.....	26
2.4 Brief summary.....	28
Chapter 3 Numerical implementation in FEA.....	30
3.1 Introduction to framework of computational plasticity.....	30
3.2 Numerical aspect implementation.....	31
3.2.1 Stress integration algorithm.....	31
3.2.2 The element deletion method.....	35
3.3 Test simulations.....	37
3.3.1 Verification under Shear.....	38
3.3.2 Verification under Tension.....	39
3.4 Brief summary.....	41
Chapter 4 Ductile fracture analysis of Al-alloy 5052BD-H14.....	42
4.1 The material and experimental procedure.....	42
4.2 SEM experiments and analysis.....	45
4.3 Calibration material parameters.....	48
4.3.1 Determination of hardening model.....	49

4.3.2 Determination of σ_R and D	50
4.3.3 Determination of f_0 and f_c	50
4.3.4 Determination of k_ω	51
4.4 Cup-cone fracture mode analysis.....	52
4.5 Brief summary	54
Chapter 5 Ductile fracture analysis of Al-alloy 5052P-H34.....	56
5.1 The material and experimental procedure.....	56
5.2 Results and analysis.....	58
5.3 Determination of the materials constants.....	60
5.3.1 Determination of hardening model.....	61
5.3.2 Determination of σ_R and D	63
5.3.3 Determination of f_0 and f_c	63
5.3.4 Determination of k_ω	64
5.4 Verification and Sandia test	66
5.4.1 Verification	66
5.4.2 Sandia test.....	67
5.5 Brief summary	69
Chapter 6 Conclusions and future work	71
6.1 Main conclusions.....	71
6.2 Future work.....	73
References	74
Acknowledgement.....	79
Publications	80

GLOSSARY OF SYMBOL

A, B, C	Material constants for Voce type hardening model
D, σ_R	Material constants in Rousselier model
$\underline{\underline{E}}$	Elastic modulus tensor
$E, \nu,$	Young's modulus, Poisson's ratio
K, G	Bulk modulus, shear modulus
$\underline{\underline{I}}$	Second order identity tensor
I_1, I_2, I_3	First, second, third invariant of stress tensor
J_1, J_2, J_3	First, second, third invariant of deviatoric stress tensor
$R(p)$	Hardening curve
f, f_0, f_c	Void volume fraction, initial value and critical value
k_ω	Shear damage coefficient
$\bar{\varepsilon}^p$ or p	Equivalent plastic stain
s_1, s_2, s_3	Deviatoric principle stresses
$\Delta \underline{\underline{\varepsilon}}$ or $\Delta \varepsilon_{ij}$	Incremental strain tensor
$\Delta \lambda$	Plastic flow multiplier
$\Delta \underline{\underline{\sigma}}$ or $\Delta \sigma_{ij}$	Incremental stress tensor
Φ	Rousselier yield potential
$\underline{\underline{\varepsilon}}$ or ε_{ij}	Strain tensor
$\underline{\underline{\varepsilon}}^e, \underline{\underline{\varepsilon}}^p$	Elastic and plastic strain tensor
$\underline{\underline{\varepsilon}}_d^p, \underline{\underline{\varepsilon}}_m^p$	Deviatoric plastic strain tensor and volumetric strain tensor

$\underline{\underline{\dot{\varepsilon}}}$	Strain rate tensor
θ_L, θ	Lode angle and Azimuth angle
ρ	Relative density
$\sigma_1, \sigma_2, \sigma_3$	Principle stresses
$\underline{\underline{\sigma}}$ or σ_{ij}	Stress tensor
$\underline{\underline{\sigma}}_d$ or s_{ij}	Deviatoric stress tensor
σ_m, σ_{eq}	Mean stress and von Mises Equivalent stress
$\underline{\underline{\dot{\sigma}}}$	Stress rate tensor
$\omega(\underline{\underline{\sigma}})$	Shear metric of stress tensor

Chapter 1 Introduction

The aluminum alloy has been used widely during the past decade, while its ductile fracture mechanism is still a hot spot[1-3]. It is well known that when metal fractures, micro-voids and micro-cracks will experience a complex process, including the nucleation, growth and coalescence[4]. So, the research in this paper is porous plasticity orientated.

1.1 Research background and significance

The phenomenon of fracture occurs almost everywhere in metals manufacturing and applying. For some plastic processing, the fracture should be avoided, e.g. deep drawing, clinching, bending. While for blanking, the fracture should be formed in certain region. Almost every part should keep its integration during working period.

The material strength theory is the basic knowledge to carry out these issues, which is connected with structure characterization, mechanical property, and its processing[1]. The fracture theory is one of the most difficult problem in the science and has not been unified[5] for its interdisciplinary, multi-scale and highly nonlinear. The accurate fracture prediction of structures under loading has been of utmost interest in the scientific and engineering community over the past centuries[6], and is of practical importance in the design and optimization of processes and products[7].

The metals fail can be divided into two broad classes of mechanisms: ductile and brittle failure[4]. The difference is the scale of plasticity. For ductile fracture, the materials experience large plastic deformation before total failure and exhibit high ductility and the fracture surface is

relative macroscopically rough because of the void nucleation-growth-coalescence[6].

So, the investigation on the mechanical behavior of the voids in the metal is the basis of ductile fracture. Some approaches have been proposed to describe the voids behavior, like McClintock[8, 9], Rice [10], Gurson [11], etc. In the view of macroscopic phenomenology, the continuum damage mechanics (CDM) based models like Lemaitre[12], Rousselier[13], etc. These models can give the damage evolution and are widely used to model the global behavior of structures.

It is well known that the mean stress $\sigma_m = \sigma_{kk} / 3$ and effective stress $\sigma_{eq} = \left(3\underline{\underline{\sigma}}_d : \underline{\underline{\sigma}}_d / 2\right)^{1/2}$ play important roles in ductile fracture, but the relation between the effective plastic strain at fracture $\bar{\varepsilon}_f$ and stress triaxiality $\eta = \sigma_m / \sigma_{eq}$ is not generally monotonic[14, 15]. Also, some experiments show that the ductility of metals is also influenced by the third stress invariant[16]. More and more tests show that the void evolution is influenced by shear deformation as well as tension[8, 17]. Usually, the fracture mode of the sheet metal is always shear failure [2, 18]. So the shear deformation also plays an important role in the fracture of metal[19]. However, the conventional damage model was proposed under high stress triaxiality, its applicability under low stress triaxiality (like shear) are seldom discussed[20]. It is necessary to propose a model which can both capture tension and shear failure with solid fundamental of physical behavior meaning, while independent with the void shape or distribution.

1.2 Review of ductile fracture models

The plasticity plays an important role in ductile fracture and is taken into account in conventional fracture criterion. These criterion conclude classical fracture mechanics models, conventional continuum mechanics models and micro mechanical models, etc. It can be reviewed as

following.

1.2.1 Classical fracture mechanics models

These models is represented by J-integral method proposed by Rice[4]. The crack opening displacement testing was widely used. But their is some restrict, it can only be used for existing crack, not for predicting crack initiation.

1.2.2 Conventional continuum mechanics models

Some empirical fracture models are proposed by taking accounts of the stress state effect, like Cockcroft and Latham[21], Oyane[22], Ayada[23], Johnson and Cook[24], etc. They have the similar mathematical type like:

$$D = \int_0^{\bar{\varepsilon}_f} f(\sigma_{ij}, \varepsilon_{ij}) d\bar{\varepsilon}^p \quad (1-1)$$

where, D is the damage factor, σ_{ij} is the stress tensor, ε_{ij} is the strain tensor, $\bar{\varepsilon}^p$ is the equivalent plastic strain, $\bar{\varepsilon}_f$ is the equivalent plastic strain when fracture occurs. The representative models can be concluded as table 1-1.

Table 1-1 Brief summary of selected typical ductile fracture criterion

Criterion	Formula
Cockcroft and Latham	$D = \int_0^{\bar{\varepsilon}_f} \langle \sigma_1 \rangle / \sigma_{eq} d\bar{\varepsilon}^p$
Oyane	$D = \int_0^{\bar{\varepsilon}_f} \langle 1 + A \frac{\sigma_m}{\sigma_{eq}} \rangle d\bar{\varepsilon}^p$
Ayada	$D = \int_0^{\bar{\varepsilon}_f} \sigma_m / \sigma_{eq} d\bar{\varepsilon}^p$
Johnson and Cook	$D = \int_0^{\bar{\varepsilon}_f} \frac{1}{D_1 + D_2 \exp(D_3 \sigma_m / \sigma_{eq})} d\bar{\varepsilon}^p$

here, σ_1 is the maximum principle stress, σ_{eq} is the equivalent stress, σ_m is the mean stress, A, D_1, D_2, D_3 are the material constants, $\langle \dots \rangle$ is the Mac Auley bracket, $\langle x \rangle = x$ if $x > 0$, $\langle x \rangle = 0$ if $x \leq 0$.

The fracture criterion can be present unified as:

$$D \geq D_c \quad (1-2)$$

here, D_c is the critical damage factor. It means failure occurs when the damage factor D exceeds some given critical value D_c .

So, these criterion are uncoupled with the constitutive model, the damage accumulation is formulated in terms of certain macroscopic variables such as the equivalent plastic strain, principle stress and mean stress, which are most relevant to fracture initiation and propagation. These approaches has been widely used due to its simple formulation and ease of calibration[25-27], despite the limitation in describing the deterioration process of materials.

1.2.3 Micro mechanical models

The effect of micro-voids in ductile fracture was first noticed by McClintock in [8, 9]. McClintock analyzed a cylindrical hole in a hardening material subjected to tensile stresses[8]. The growth of the cavity was given as:

$$\frac{dR}{d\varepsilon} = \frac{\sqrt{3}R}{2(1-n)} \sinh \left[\frac{\sqrt{3}}{2}(1-n) \frac{(\sigma_a + \sigma_b)}{\bar{\sigma}} \right] + \frac{d(\varepsilon_a + \varepsilon_b)}{2d\varepsilon} \quad (1-3)$$

here, R is the mean radius of the cylindrical hole with a initial value of R_0 , $\bar{\sigma} = K\bar{\varepsilon}^n$ is the power law hardening, $\bar{\sigma}$, $\bar{\varepsilon}$, n and K are the effective stress, effective strain, hardening coefficient and hardening modulus, respectively. σ_a , σ_b , ε_a and ε_b are the principle stress and strain in plane stain problem.

McClintock also analyzed a of spherical hole pulled by axisymmetric tensile stress[9], the growth ratio was given as:

$$\frac{\dot{V}}{\dot{\varepsilon}V} = \sqrt{3} \sinh \left[\frac{\sqrt{3}\sigma_m}{\sigma} \right] \quad (1-4)$$

here, V is the volume the hole, \dot{V} is the growth rate, $\dot{\varepsilon}$ is the effective strain rate.

Rice considered the growth of a spherical void in a non-hardening material subjected to remote uniaxial tension[10]. Rice and Tracey showed that for high stress triaxiality, the growth rate of the void radius can be written as an analytical expression as:

$$\frac{\dot{R}}{R_0} = 0.283 \exp \left(\frac{3\sigma_m}{2\sigma_y} \right) \dot{\varepsilon} \quad (1-5)$$

here R is the radius of the spherical hole with a initial value of R_0 , σ_m is the mean stress of remote tension stress, σ_y is the yield stress of the material, $\dot{\varepsilon}$ is the strain rate. It can be seen that the growth of void is effected by stress triaxiality from equation (1-5).

For a metal containing a dilute concentration of voids, based on a rigid-plastic upper bound solution for spherically symmetric deformations of a single spherical void, Gurson[11] proposed a yield condition with the damage accumulation of the form:

$$\phi = \left(\frac{\sigma_{eq}}{\sigma_M} \right)^2 + 2q_1 f \cosh \left(\frac{3}{2} \frac{q_2 \sigma_m}{\sigma_M} \right) - (1 + q_3 f^2) = 0 \quad (1-6)$$

here, f is the void volume fraction with a initial value of f_0 , σ_M is the yield stress of the undamaged material as a function of the equivalent plastic strain of the matrix material. The other parts conclude flow rule, evolution of the plastic strain and f . Tvergaard[28] introduced the constants q_1 , q_2 , $q_3 = q_1^2$, to make the predictions of Gurson model agree with numerical studies. And this model was further developed by Needleman[28] as Gurson-Tvergaard-Needleman (GTN) model.

A lot of researches were carried out to calibration the parameters of GTN model and numerous applications. In [29], a computational cell approach was proposed to model ductile fracture in surface-cracked. The research in [30] shows that the element size should be estimated first by compact test (CT), follow by initial void volume fraction f_0 . The common values is between 50 ~ 300 μm for element size, 0.001~0.005 for f_0 , 0.10~0.20 for critical fraction f_E . In [31], the volume fraction at final failure f_F was suggested to be estimated as:

$$f_F = 0.15 + 2f_0 \quad (1-7)$$

Then, for some materials that follow the cluster nucleation law, f_F can be fixed as 0.15, then the only unknown parameter is f_0 [31]. Then the calibration can be conducted by few test such as CT, uniaxial tension test[32], etc.

And the calibration method for void is to use the metallurgical graph and it is hard to measure the actual value of void volume fraction[33, 34].

1.2.4 Damage mechanics models

Damage is defined as the creation and growth of micro-voids or micro-cracks in solid materials in its mechanical sense[12]. Damage mechanics was firstly proposed by Kachanov, developed by Rabotnov and Lemaitre[12]. The main research concludes the mechanical behavior of materials with damage, the damage evolution process and the ultimate destruction of material. The coupled damage constitutive models which can describe the derivation process are the fundamental to deal with its plasticity and damage behavior.

Lemaitre introduced the famous strain equivalence hypothesis and the damage D can be defined as the loss of stiffness[12]:

$$D = 1 - \frac{\tilde{E}}{E} \quad (1-8)$$

here, E is the Young's modulus of undamaged elasticity and \tilde{E} is the actual modulus of damaged elasticity. Then the damage measurement can be performed easily by loading-unloading tests. The Hooke's law coupled with damage was given as:

$$\sigma = \mathbf{C}_0 \varepsilon^e (1 - D) \quad (1-9)$$

here, σ is the stress tensor, ε^e is the elastic strain, \mathbf{C}_0 is the initial elasticity stiffness matrix.

Then the yield condition written is

$$\phi = \left(\frac{\sigma_{eq}}{1 - D} \right)^2 - (\sigma_y)^2 \leq 0 \quad (1-10)$$

The damage evolution law is given as:

$$\frac{dD}{d\varepsilon^p} = \frac{D_c}{\varepsilon_R - \varepsilon_D} \left[\frac{2}{3} (1 + \nu) + 3(1 - 2\nu) \left(\frac{\sigma_m}{\sigma} \right)^2 \right] \left(\frac{\varepsilon^p}{\varepsilon} \right)^{2n} \quad (1-11)$$

here, the three damage constants, D_c , ε_R and ε_D , are generally determined by the repetitive loading-unloading tensile test proposed by Lemaitre[12, 35].

1.3 State of damage mechanics based on \mathbf{I}_1 - \mathbf{J}_2 - \mathbf{J}_3 framework

Here, some new plasticity and damage theory are briefly reviewed. The stress theory is the fundamental of elasticity and plasticity. A lot of strength theories were established in the principal stress space. A particular stress state can be represented by a point in a three-dimensional Cartesian coordinate system with $(\sigma_1, \sigma_2, \sigma_3)$ — the so-called Haigh-Westergaard stress space as shown in Figure 1-1(a)[16, 36]. The stress tensor can be decomposed into deviatoric stress and mean stress as:

$$\sigma_{ij} = s_{ij} + \sigma_m \delta_{ij} \quad (1-12)$$

here, s_{ij} is the deviatoric stress tensor, δ_{ij} is the Kroeneker delta, $\sigma_m = \frac{1}{3}(\sigma_1 + \sigma_2 + \sigma_3)$ is the mean stress. According to the definition of stress invariant:

$$I_1 = \sigma_1 + \sigma_2 + \sigma_3 \quad (1-13)$$

$$J_2 = \frac{1}{2}(s_1^2 + s_2^2 + s_3^2) \quad (1-14)$$

$$J_3 = s_1 s_2 s_3 \quad (1-15)$$

The stress state $(\sigma_1, \sigma_2, \sigma_3)$ corresponds to a particular coordinate in (I_1, J_2, J_3) framework as shown in Figure 1-1(b). The angle θ is J_3 related, which is ignored in von Mises theory[37-39].

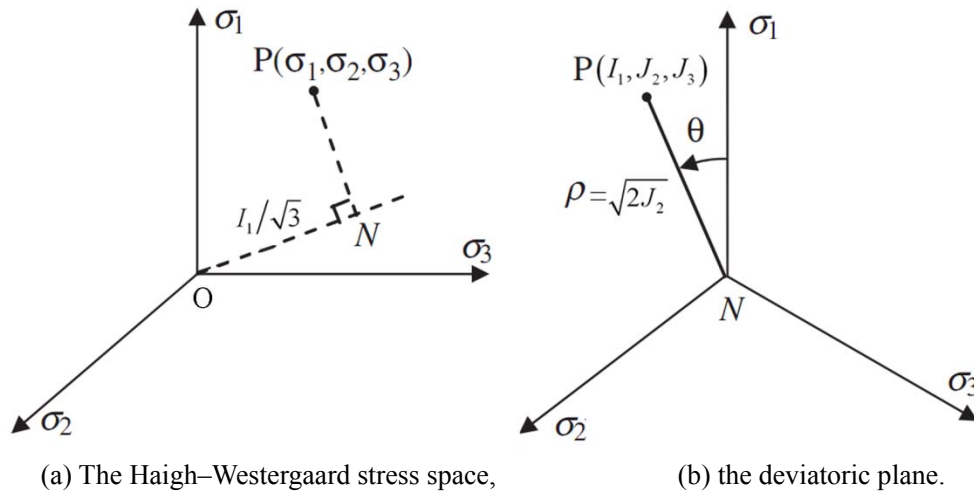


Figure 1-1 Two types of coordinate system in the space of principal stresses.

Some plasticity and damage theories were established in the (I_1, J_2, J_3) framework as complete understanding of stress.

1.3.1 Plasticity theory concerning triaxiality and Lode parameter

In soil mechanics, rock mechanics and other disciplines, σ_m or I_1 are usually considered. While the research of Bridgman show that yielding does not depend on hydrostatic stress and that the yielded material is incompressible[40, 41]. Classical plasticity theory was largely built on these

observations[37-39]. However, Richmond's research show that the yield strength was a linear function of hydrostatic pressure for 4330 steel[42]. Wilson's research on Al-alloy 2024-T351 point out that hydrostatic tensile stress effects yielding[41]. The von Mises yield theory results overestimated experimental load-displacement curves by 10–65 percent. But the Drucker-Prager[43] theory (Equation (1-16))results essentially matched the experimental results.

$$\sigma_{eq} = \sigma_0(\bar{\epsilon}^p) - aI_1 \quad (1-16)$$

here, $\sigma_0(\bar{\epsilon}^p)$ is the hardening curve when $\sigma_m = 0$, a is the material constant.

The research [16] from Impact and Crashworthiness Lab of Massachusetts Institute of Technology show that the yielding for Al-alloy 2024-T351 is not only effected by the stress triaxiality, but also Lode parameter. Figure 1-2(a) shows the Lode parameter related yield loci in the deviatoric stress plane. The proposed 3D yield surface in the space of principal stresses is not a cylindrical surface, but with a possible vertex when $\sigma_1 > 0, \sigma_2 > 0, \sigma_3 > 0$.

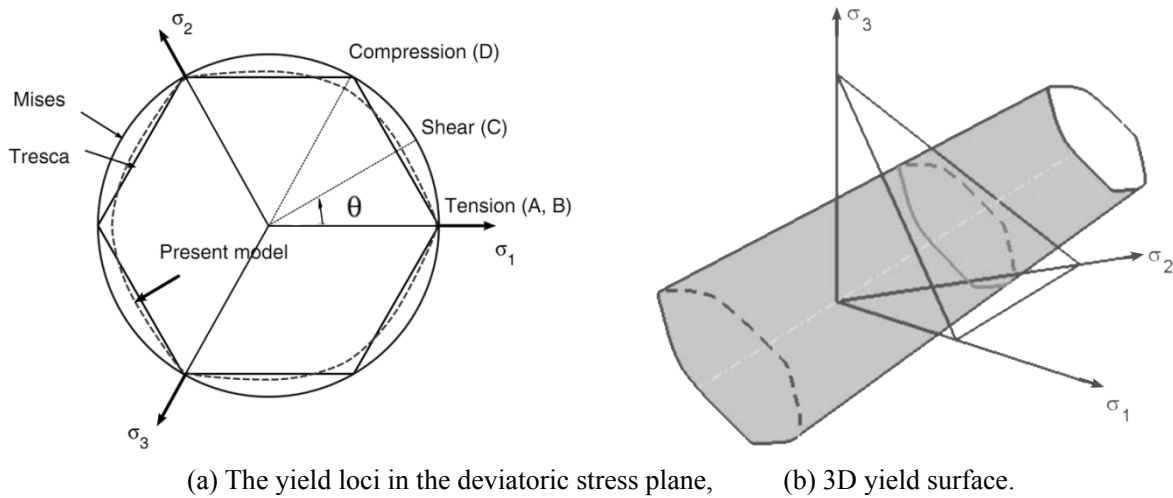


Figure 1-2 The yield surface proposed by Bai[16] in the space of principal stresses.

Increasing experimental evidence shows that the classical J_2 plasticity theory may not fully describe the plastic response of metals, which is pressure sensitivity and Lode dependence[16, 36, 44, 45]. Some new general forms of the yield function for isotropic materials are assumed to be

functions of I_1, J_2, J_3 [36, 45]. This new modeling idea has become a hot spot recently[44], at the same time some experimental tests are also established systemically[14-16, 46]. The constitutive equation of Al-alloy 5083 was established in the (I_1, J_2, J_3) framework by Tingting Zhang[36].

1.3.2 Damage theory concerning triaxiality and Lode parameter

The experimental researches on Al-alloy 2024T351 by Tomasz Wierzbicki [14, 46] show that the stress triaxiality is the most important factor that controls initiation of ductile fracture. In the range of negative stress triaxiality, shear fracture dominates, e.g. in the upsetting tests. For high stress triaxiality, fracture occurs due to void formation, e.g. in tensile tests. While at stress triaxiality between above two regimes, fracture may develop as a combination of shear and void growth mode. The fracture mechanism varies with the stress triaxiality, can be seen in Figure 1-3.

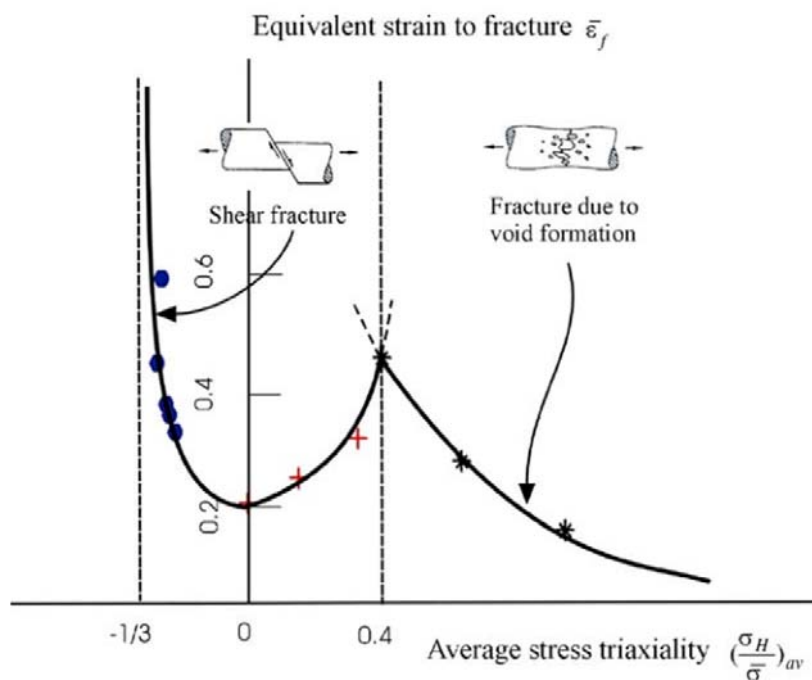


Figure 1-3 Dependence of the fracture mechanism and strain on the stress triaxiality[14].

Similar with the plasticity, it is found that the fracture mechanism and mode are also influenced by the J_3 invariant or Lode parameter by Tomasz Wierzbicki[16]. The fracture locus in the plane

of stress triaxiality and Lode parameter is also proposed as a surface[16], as shown in Figure 1-4. It can be concluded that the fracture locus in Figure 1-3 is only a curve on the fracture surface in Figure 1-4, indicated as "plane stress".

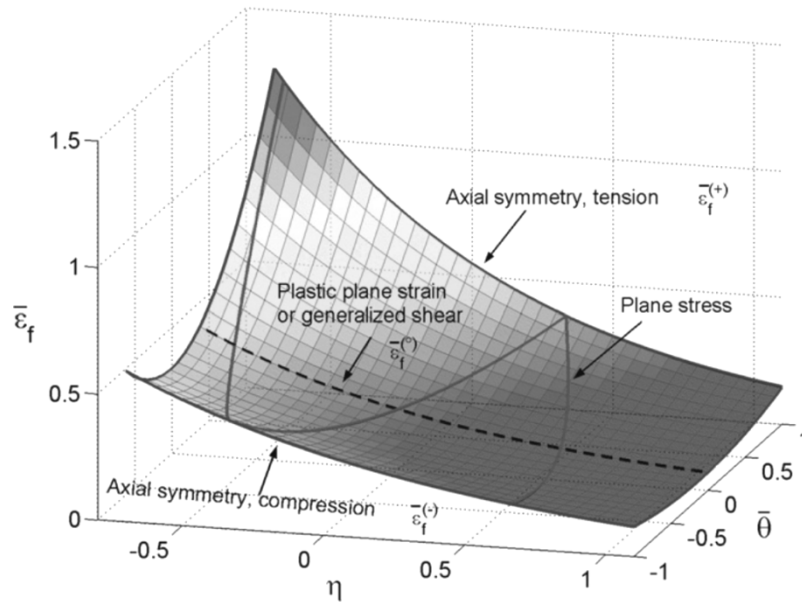


Figure 1-4 The newly postulated 3D asymmetric fracture locus[16].

A coupled damage constitutive model was proposed as a parallel research by Xue [6], showing the combined effects of the mean stress and the deviatoric state as shown in Figure 1-5. The typical results predicted by the proposed damage plasticity model in [47] are the realistic “cup-cone” fracture mode of a smooth round bar, the slant fracture of a doubly grooved flat plate (transverse plane strain) and compact tension specimen, and diffused necking of tensile flat specimen. The shear lip in three point bending specimen was also explained in [48]. Even for upsetting test, the fracture patterns can be obtained [49].

As mentioned above, the widely used GTN model shows its inherent drawbacks, especially for low stress triaxiality, for it was conceived and derived with high stress triaxiality. The damage in GTN model is limited to void volume fraction[6]. So it is difficult to compare damage with Lemaître model or Xue's model, although the aim of the variables are the same. So, it is necessary

to model the damage as a more universal metric of deterioration in material. The Rousselier model[4, 13, 50] derived in the framework of thermodynamics of irreversible processes is selected in this thesis.

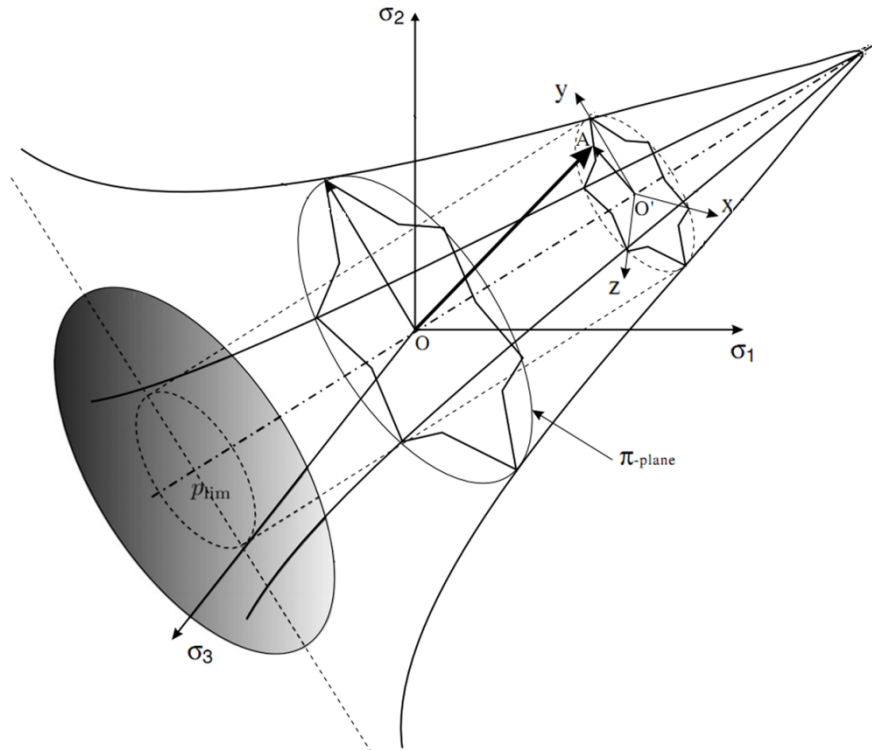


Figure 1-5 A three-dimensional sketch of the fracture envelope in the space of the principal stresses[47].

1.4 Thesis organization

Chapter 1 gives background, review of ductile fracture models, damage mechanics and presents an outline of the thesis.

In Chapter 2, the applicability of original Rousselier model on shear will be discussed. A modified model which can both predict tension and shear failure will be proposed. The physical meaning of the new damage evolution rule will also be interpreted. The analytical solution of the modified damage evolution equation under shear will be developed, and its applicability on describing shear fracture of material will be discussed.

In Chapter 3, the numerical implementation of the modified model will be discussed. The key subject is the stress integration algorithm within computational plasticity framework. Some necessary benchmark tests will also be conducted to verify the stress integration algorithm and correspondingly developed VUMAT subroutine.

In chapter 4, the ductile fracture mechanism of Al-alloy 5052BD-H14 will be analyzed by a series of test. The mechanical behavior of micro-voids under complex stress state will be discussed. The material constants will be calibrated consequently by simulations and experiments. The cup-cone fracture mode will be studied in this chapter.

In chapter 5, the Al-alloy 5052P-H34 will be selected as the testing material for it is widely used nowadays and in the future. Both physical experiments and numerical simulations will be performed to identify the material constants. A benchmark test will be carried out to verify the prediction ability of the modified model.

Chapter 6 concludes the present thesis and suggests future research topics.

Chapter 2 Modified Rousselier model

In chapter 2, a modified Rousselier model [51] was proposed by incorporating the recent extended damage evolution model by Nahshon and Hutchinson[20]. The applicability of modified model on shear will be discussed.

2.1 Introduction of the original Rousselier damage model

The Rousselier model for porous metal plasticity in the frame of continuum damage mechanics (CDM) is a local approach to fracture[13]. The rate independent, isotropic hardening and isotropic damage are assumed. Two internal variables are used to quantify the deterioration process of material, one is the equivalent plastic strain p and the other is the so-called damage variable or void volume fraction f . The model contains four parts, namely yield function, Hook's law, flow rule and damage evolution's law, which could be summarized as below.

2.1.1 Yield function

The yield potential is written as Eq.(2-1) [4, 13, 50], so it is a coupled constitutive equation in which the damage accumulation and hydrostatic stress are incorporated:

$$\Phi = \frac{\sigma_{eq}}{\rho} - R(p) + Df \sigma_R \exp\left(\frac{\sigma_m}{\rho \sigma_R}\right) = 0 \quad (2-1)$$

Here, $\underline{\underline{\sigma}} = \underline{\underline{\sigma}}_d + \sigma_m \underline{\underline{I}}$ is the Cauchy stress tensor, $\underline{\underline{\sigma}}_d$ is the deviatoric stress tensor, σ_m is mean stress, $\underline{\underline{I}}$ is the second order unity tensor, $\sigma_{eq} = \left(3\underline{\underline{\sigma}}_d : \underline{\underline{\sigma}}_d / 2\right)^{1/2}$ is the von Mises equivalent stress, $\rho = (1-f)/(1-f_0)$ is the relative density, f is the void volume fraction (damage variable), f_0 is the initial void volume fraction, $R(p)$ is the hardening function,

$p = \left(\frac{2\varepsilon^p : \varepsilon^p}{3} \right)^{1/2}$ is the equivalent plastic strain. D and σ_R (originally written as σ_1) are material constants, usually $D = 2$ [4, 13, 50].

According to [4], σ_R can be determined by tensile test as

$$\sigma_R = \frac{2}{3} \frac{\int_0^{p_F} R(p) dp}{p_F} \quad (2-2)$$

Here, p_F is the fracture strain. If the hardening obeys a power function $R(p) = Kp^n$, then

$$\sigma_R = \frac{2}{3} \frac{K p_F^n}{n+1} [4]. \text{ If the material obeys voce type hardening[52],}$$

$$R(p) = A - (A - B) \exp(-Cp) \quad (2-3)$$

Here A , B and C are constants, when p_F is greater than some constants, σ_R can be determined as

$$\sigma_R = \frac{2}{3} \left\{ A - \frac{A-B}{C p_F} [1 - \exp(-C p_F)] \right\} \approx \frac{2}{3} A \quad (2-4)$$

For von Mises yield criterion, yield radius $\sigma_{eq}/\sigma_0 = 1$, implying the yield or flow is independent of mean stress [37-39]. While for Rousselier model, at the initial yield condition, $f = f_0$, $\rho = 1$ and $R(p) = \sigma_0$, yield radius [53] is

$$\frac{\sigma_{eq}}{\sigma_0} = 1 - D f_0 \left(\frac{\sigma_R}{\sigma_0} \right) \exp \left(\frac{\sigma_m/\sigma_0}{\sigma_R/\sigma_0} \right) \quad (2-5)$$

It can be plotted as Figure 2-1, for $\sigma_R = 180\text{MPa}$, $\sigma_0 = 209.6\text{MPa}$ (Al-alloy 5052) with a series of assumed f_0 . It can be seen that the yield radius decreased with increasing mean stress or f_0 . $f_0 = 1$ gives von Mises yield condition. By Eq. (2-5), the yield surface in the principle stresses space can also be postulated as Figure 2-2, showing a revolved bell as the same as Figure 2-1. The intersecting line of yield locus with deviatoric plane is always circular, for the isotropy assumption in Eq. (2-1).

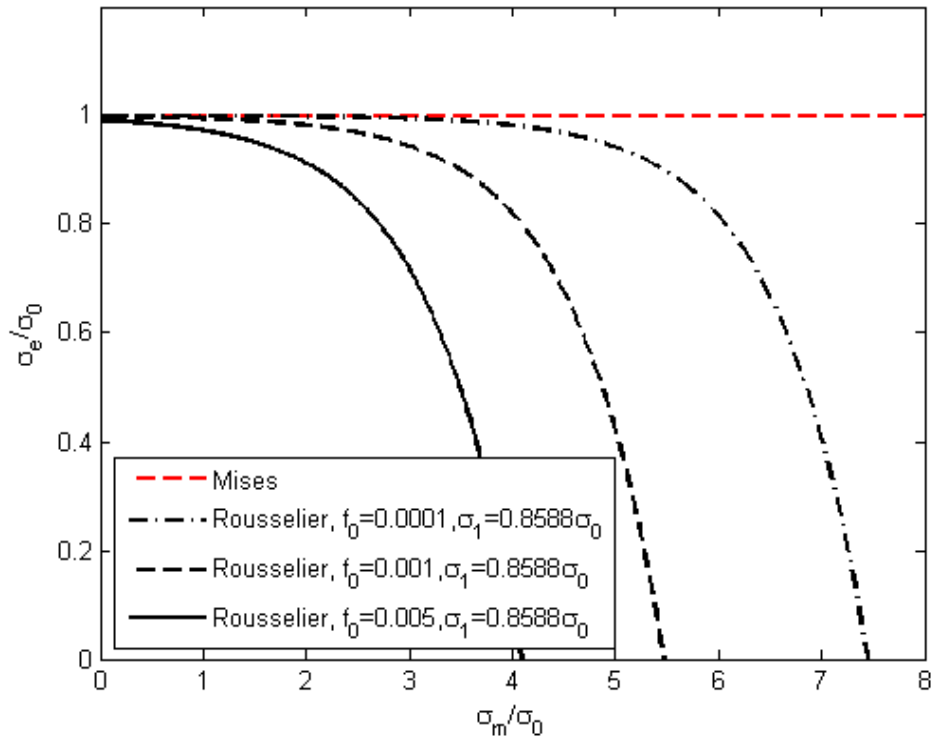


Figure 2-1 The yield surfaces of Rousselier and von Mises models on the $\sigma_{eq} - \sigma_m$ plane

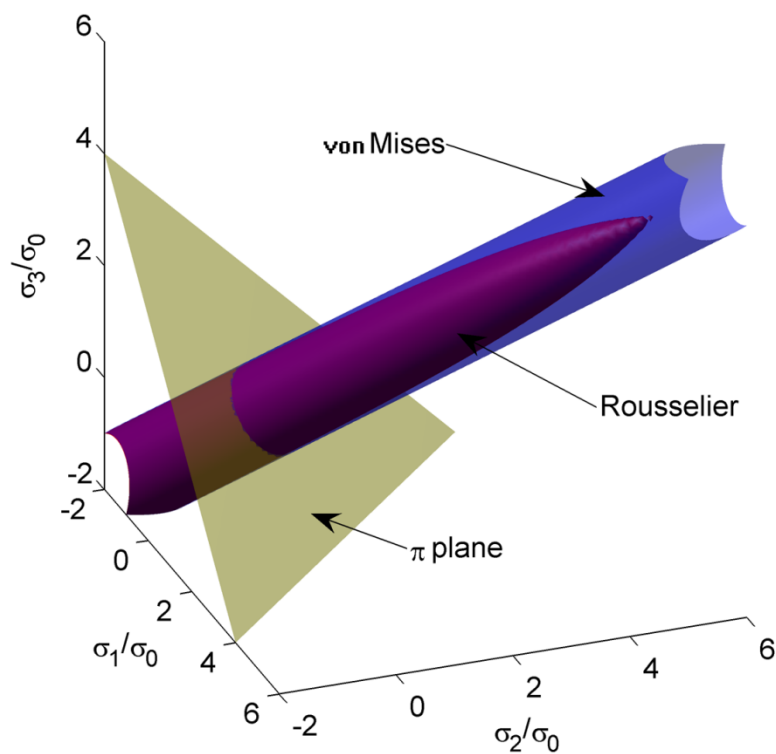


Figure 2-2 The yield surfaces of Rousselier and von Mises models in the principle stresses space, noting that

isotropy is assumed, the cross section is circular.

2.1.2 Hooke's Law

The stress strain relation or Hooke's Law is written as the following equation[4]:

$$\underline{\underline{\sigma}} = \rho \underline{\underline{E}} : \underline{\underline{\varepsilon}}^e = \rho \underline{\underline{E}} : (\underline{\underline{\varepsilon}} - \underline{\underline{\varepsilon}}^p) \quad (2-6)$$

Here, $\underline{\underline{E}}$ is the elastic modulus tensor, $\underline{\underline{\varepsilon}}$ is the strain tensor, $\underline{\underline{\varepsilon}}^e$ and $\underline{\underline{\varepsilon}}^p$ are the elastic and plastic part of strain tensor, respectively. So the additive decomposition $\underline{\underline{\varepsilon}} = \underline{\underline{\varepsilon}}^e + \underline{\underline{\varepsilon}}^p$ is also included in Eq. (2-6).

2.1.3 Flow rule

The plastic strain rate tensor can be expressed using the normality rule:

$$\dot{\underline{\underline{\varepsilon}}}^p = \dot{p} \frac{\partial \Phi}{\partial (\underline{\underline{\sigma}}/\rho)} = \dot{p} \left[\frac{3\underline{\underline{\sigma}}_d}{2\underline{\underline{\sigma}}_{eq}} + \frac{1}{3} Df \exp\left(\frac{\underline{\underline{\sigma}}_m}{\rho\underline{\underline{\sigma}}_R}\right) \underline{\underline{I}} \right] \quad (2-7)$$

So that the plastic part of strain tensor can be divided into a deviatoric part and a volumetric part by $\underline{\underline{\varepsilon}}^p = \underline{\underline{\varepsilon}}_d^p + \underline{\underline{\varepsilon}}_m^p \underline{\underline{I}}$, therefore, the deviatoric part of plastic strain rate tensor can be given as:

$$\dot{\underline{\underline{\varepsilon}}}_d^p = \dot{p} \frac{3\underline{\underline{\sigma}}_d}{2\underline{\underline{\sigma}}_{eq}} \quad (2-8)$$

And the volumetric plastic strain rate was derived as following:

$$\dot{\underline{\underline{\varepsilon}}}_m^p = \frac{1}{3} \dot{p} Df \exp\left(\frac{\underline{\underline{\sigma}}_m}{\rho\underline{\underline{\sigma}}_R}\right) \quad (2-9)$$

The derivative is always positive, indicating the volumetric plastic strain $\underline{\underline{\varepsilon}}_m^p$ is positive.

2.1.4 Damage evolution's law

The relation between the damage variable with the volumetric plastic strain rate used in Rousselier model was derived by mass conservation as the following equation:

$$\dot{f} = 3(1-f) \dot{\underline{\underline{\varepsilon}}}_m^p \quad (2-10)$$

By substituting Eq. (2-9) into Eq. (2-10), the evolution rate of the damage variable can be written as a function of the equivalent plastic strain rate and mean stress:

$$\dot{f} = Df(1-f) \exp\left(\frac{\sigma_m}{\rho\sigma_R}\right) \dot{p} \quad (2-11)$$

The damage is influenced by mean stress, showing good result for tension failure [53-55]. The special form of Eq. (2-11) can give a damage evolution at $\sigma_m = 0$, e.g. simple shear in Figure 2-3. Supposing the initial damaged material with initial void volume fraction f_0 and the elasticity can be neglected.

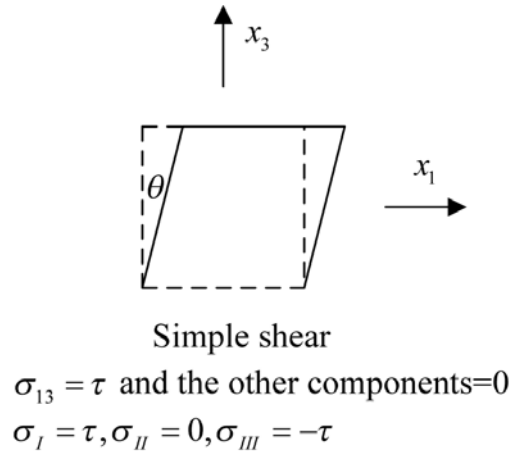


Figure 2-3 Initial damaged material under simple shear.

Then the Eq. (2-11) can be simplified as:

$$\dot{f} = Df(1-f) \dot{p} \quad (2-12)$$

Taking the boundary condition $f|_{p=0} = f_0$, the solution is:

$$f = \frac{f_0}{(1-f_0)e^{-Dp} + f_0} \quad (2-13)$$

By substituting different f_0 as $10^{-4}, 10^{-3}, 5 \times 10^{-3}, 10^{-2}$ and $D=2$, the damage increases with the equivalent plastic strain as shown in Figure 2-4. However, this result is the instinct of original model, lacking of verification. The mean stress sensitivity and Lode parameter dependence will be considered in the following discussions.

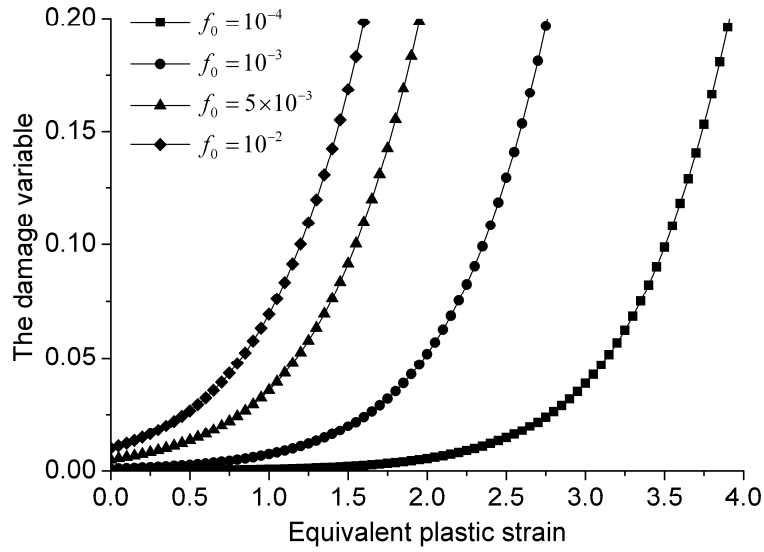


Figure 2-4 The damage evolution under shear by original Rousselier model.

2.2 The modified Rousselier damage model

The research results in [20, 28, 56] imply that the damage evolution law in Eq. (2-10) shows its inapplicability to localization and fracture for low triaxiality. According to the research of McClintock in[8], voids deform when shear occurs, while volume keeps constant in such case. The meaning of Eq. (2-10) is mass conservation's law of metal with voids during deformation as Figure 2-5. For any porous metal V in volume containing voids Vf and metal $(1-f)V$, when deformation occurs, metal will obey mass conservation's law. It can be derived as:

$$\frac{d[(1-f)V]}{dt} = 0 \quad (2-14)$$

resulting as

$$(1-f) \frac{dV}{dt} + V \frac{d(1-f)}{dt} = 0 \quad (2-15)$$

giving that

$$\frac{df}{dt} = (1-f) \frac{dV}{V} / dt = 3(1-f) \dot{\epsilon}_m^p \quad (2-16)$$

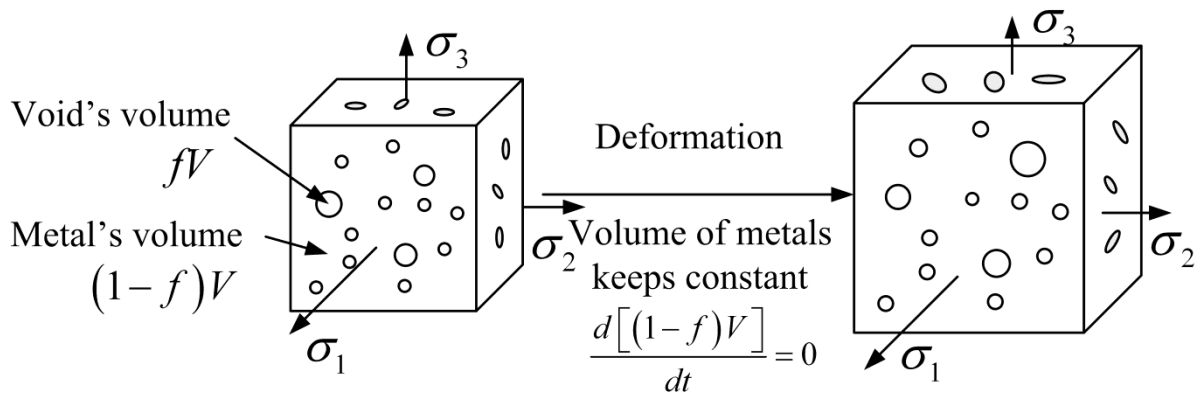


Figure 2-5 The deformation of metal with voids, noticing that metal obeys mass conservation's law.

So that, Eq. (2-10) doesn't stand by when the volume keeps constant e.g. shear deformation. So, some modifications is needed.

2.2.1 The Lode angle and shear metric of stress tensor

In the view of [16], the deformation state of material can be distinguished by Lode angle in the space of principle stresses. For any stress state $(\sigma_1, \sigma_2, \sigma_3)$ in the Cartesian coordinate system, it can be transformed to the corresponding cylindrical coordinate system (ρ, θ, z) as shown in Figure 2-6.

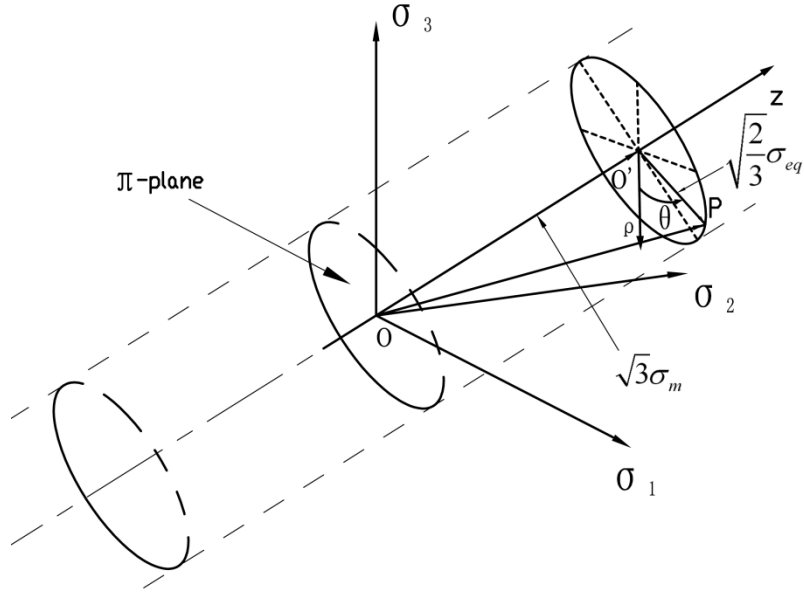


Figure 2-6 Cartesian and cylindrical coordinate systems in the space of principle stresses.

$$|\overline{OO'}| = \sqrt{3}\sigma_m = I_1/\sqrt{3} \quad (2-17)$$

$$|\overline{O'P}| = \sqrt{\frac{2}{3}}\sigma_{eq} = \sqrt{2J_2} \quad (2-18)$$

here, $I_1 = \sigma_1 + \sigma_2 + \sigma_3$ and $J_2 = \frac{1}{2}(s_1^2 + s_2^2 + s_3^2)$ are the first invariant of stress, the second invariant of deviatoric stress, $\sigma_m = I_1/3$ and $\sigma_{eq} = \sqrt{3J_2}$ are the mean stress and equivalent stress, respectively.

While a third variable or Lode angle or azimuth angle should be introduced at the same time, to determine the position in π plane. The azimuth angle can be defined as the angle to the positive direction of the s_1 axis, as shown in Figure 2-7.

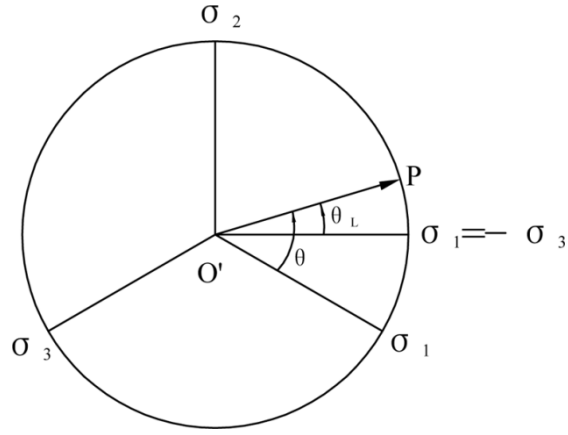


Figure 2-7 The definition of Lode angle and azimuth angle in π plane.

The expression was derived as Eq. (2-19) [6]:

$$\theta = \cot^{-1} \left[\frac{2}{\sqrt{3}} \left(\frac{1}{\chi} - \frac{1}{2} \right) \right] \quad (2-19)$$

where $\chi = \frac{s_2 - s_3}{s_1 - s_3}$. It can also be introduced as

$$\cos(3\theta) = \frac{27J_3}{2\sigma_{eq}^3} \quad (2-20)$$

here, θ is the Lode angle, as referenced in [16], $J_3 = s_1 s_2 s_3$ is the third invariant of deviatoric stress, s_1, s_2, s_3 are the deviatoric principle stresses. The transform relation between Cartesian and cylindrical coordinate systems in the space of principle stresses can be summarized as:

$$\begin{cases} z = I_1 / \sqrt{3} \\ \rho = \sqrt{3J_2} \\ \theta = \frac{1}{3} \arccos \left(\frac{3\sqrt{3}J_3}{2J_2^{3/2}} \right) \end{cases} \quad (2-21)$$

2.2.2 The non-dimensional metric of stress

The non-dimensional metric of stress $\omega(\underline{\underline{\sigma}})$ was introduced by [20] as

$$\omega(\underline{\sigma}) = 1 - \xi^2 = 1 - \left(\frac{27J_3}{2\sigma_{eq}^3} \right)^2 \quad (2-22)$$

here, $\xi = \frac{27J_3}{2\sigma_{eq}^3}$ is the Lode parameter in [7, 16], or normalized third invariant in [57] and lies in the range $-1 \leq \omega \leq 1$. Then the relation between the non-dimensional metric $\omega(\underline{\sigma})$ and the Lode angle could be introduced as:

$$\omega(\underline{\sigma}) = 1 - \cos^2(3\theta) = \sin^2(3\theta) \quad (2-23)$$

So, the non-dimensional metric is an even and periodic function of Lode angle in the π plane, lying in the range $0 \leq \omega \leq 1$, which can discriminate between axisymmetric and shear-dominated stress states. For any uniaxial tension or compression stress state, $\omega = 0$.

$$\sigma_1 \geq \sigma_2 = \sigma_3 \quad \text{or} \quad \sigma_1 = \sigma_2 \geq \sigma_3 \quad (2-24)$$

And for all states comprised of a pure shear stress plus a hydrostatic contribution, $\omega = 1$ (see details in [20]).

$$\sigma_1 = \tau + \sigma_m, \sigma_2 = \sigma_m, \sigma_3 = -\tau + \sigma_m \quad (2-25)$$

So, $\omega(\underline{\sigma})$ can be treated as a metric of stress tensor approaching shear state.

2.2.3 The distribution of shear metric under plane stress

Special attention is given to the plane stress state, as a series of classical specimens and test are done under $\sigma_3 = 0$. If $x = \sigma_{II}/\sigma_I$ is assumed as the ratio of second and first principle stresses, then σ_m and J_3 are derived as,

$$\sigma_m = \frac{1+x}{3} \sigma_I \quad (2-26)$$

$$\begin{aligned}
J_3 &= (\sigma_I - \sigma_m)(\sigma_{II} - \sigma_m)(\sigma_{III} - \sigma_m) = \sigma_I^3 \left(1 - \frac{1+x}{3}\right) \left(x - \frac{1+x}{3}\right) \left(-\frac{1+x}{3}\right) \\
&= \frac{\sigma_I^3}{27} (x-2)(2x-1)(x+1)
\end{aligned} \tag{2-27}$$

respectively. By $\sigma_{eq}^2 = \frac{3}{2} s_{ij} : s_{ij} = \sigma_x^2 + \sigma_y^2 - \sigma_x \sigma_y + 3\tau_{xy}^2$, obtaining

$$\sigma_{eq}^2 = (x^2 - x + 1) \sigma_I^2 \tag{2-28}$$

then the shear metric of stress tensor could be derived as

$$\omega(\underline{\underline{\sigma}}) = 1 - \left(\frac{27J_3}{2\sigma_{eq}^3} \right)^2 = 1 - \frac{(x-2)^2 (2x-1)^2 (x+1)^2}{4(x^2 - x + 1)^3} \tag{2-29}$$

Then the shear metric of stress tensor is a function of $x = \sigma_{II}/\sigma_I$. Special stress state and corresponding Lode angle are shown in Figure 2-8. $\omega(\underline{\underline{\sigma}}) = 0$ for uniaxial tension, where $\theta = 0^\circ$.

For equi-biaxial tension $\theta = 60^\circ$, $\omega(\underline{\underline{\sigma}}) = 0$. While for $\sigma_{II}/\sigma_I = 0.5$, which represents as a pure shear stress plus hydrostatic tension as Eq. (2-30),

$$\begin{bmatrix} \sigma_I = 2\sigma_{II} & 0 & 0 \\ 0 & \sigma_{II} & 0 \\ 0 & 0 & 0 \end{bmatrix} = \begin{bmatrix} \sigma_{II} & 0 & 0 \\ 0 & 0 & 0 \\ 0 & 0 & -\sigma_{II} \end{bmatrix} + \begin{bmatrix} \sigma_{II} & 0 & 0 \\ 0 & \sigma_{II} & 0 \\ 0 & 0 & \sigma_{II} \end{bmatrix} \tag{2-30}$$

and $\theta = 30^\circ$, then $\omega(\underline{\underline{\sigma}}) = 1$. Special attention should be taken that θ is defined in the π plane, which is perpendicular to z or σ_m axis.

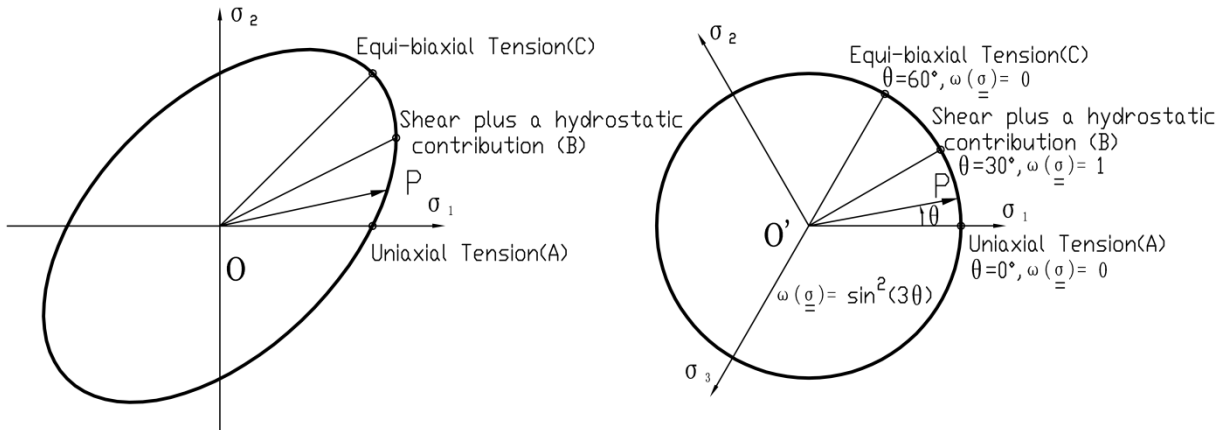


Figure 2-8 Lode angle and corresponding shear metric in plane stress on von Mises yield locus.

2.2.4 The modified Rousselier model concerning shear failure

According to research in [8, 17, 20, 49, 58], the void growth is no longer directly tied to the plastic volume change as Eq. (2-16). The total void deformation, such as growth, distortion, coalescence, etc. can be simply treated as a parameter measuring the damage accumulation. It is recommended that the void evolution rate can be written as Eq. (2-31) with an additional phenomenological term [20, 32, 57]. As mentioned above, the characterization of $\omega(\underline{\underline{\sigma}})$ makes it resulting in a maximum effect for pure shear while no effect for tension or compression stress states.

$$\dot{f} = 3(1-f)\dot{\epsilon}_m^p + k_\omega f \omega(\underline{\underline{\sigma}}) \frac{\underline{\underline{\sigma}}_d : \dot{\underline{\underline{\epsilon}}}_d^p}{\sigma_{eq}} \quad (2-31)$$

here, k_ω is the shear damage coefficient [20, 32, 57]. By substituting the Eq. (2-9) and Eq. (2-8) into Eq. (2-31), then a new damage evolution rule could be derived as Eq. (2-32):

$$\begin{aligned} \dot{f} &= 3(1-f)\dot{\epsilon}_m^p + k_\omega f \omega(\underline{\underline{\sigma}}) \frac{\underline{\underline{\sigma}}_d : \dot{\underline{\underline{\epsilon}}}_d^p}{\sigma_{eq}} = 3(1-f)\dot{\epsilon}_m^p + k_\omega f \omega(\underline{\underline{\sigma}}) \frac{\underline{\underline{\sigma}}_d}{\sigma_{eq}} \dot{p} \frac{3}{2} \frac{\underline{\underline{\sigma}}_d}{\sigma_{eq}} \\ &= Df(1-f) \exp\left(\frac{\sigma_m}{\rho\sigma_R}\right) \dot{p} + k_\omega f \omega(\underline{\underline{\sigma}}) \dot{p} \end{aligned} \quad (2-32)$$

Obviously, the additional phenomenological term in Eq. (2-32) does not comply with the mass conservation law. It is not a void growth term, which could be considered as a nucleation term. The decomposition can be rewritten as

$$\dot{f} = \dot{f}_{growth} + \dot{f}_{nucleation} \quad (2-33)$$

here

$$\dot{f}_{growth} = Df(1-f) \exp\left(\frac{\sigma_m}{\rho\sigma_R}\right) \dot{p} \quad (2-34)$$

$$\dot{f}_{nucleation} = k_\omega f \omega(\underline{\underline{\sigma}}) \dot{p} \quad (2-35)$$

2.3 The physical meaning of the damage evolution rule

Supposing the initial damaged material with initial void volume fraction f_0 , e.g. simple shear in Figure 2-3. For a specified loading path when the mean stress $\sigma_m = 0$ and $\omega(\underline{\underline{\sigma}})$ keeps as constant, Eq. (2-32) can be transferred to an ordinary differential equation

$$\frac{df}{dp} = Df(1-f) + k_\omega \omega(\underline{\underline{\sigma}})f \quad (2-36)$$

With $f|_{p=0} = f_0$ as the boundary condition, the analytical solution can be derived as:

$$f = \frac{(D + k_\omega \omega(\underline{\underline{\sigma}}))f_0}{(D + k_\omega \omega(\underline{\underline{\sigma}}) - Df_0)e^{-(D + k_\omega \omega(\underline{\underline{\sigma}}))p} + Df_0} \quad (2-37)$$

Then for the shear stress state, the solution can be particularized with $D = 2$, and $\omega(\underline{\underline{\sigma}}) = 1$ as

$$f = \frac{(2 + k_\omega)f_0}{(2 + k_\omega - 2f_0)e^{-(2 + k_\omega)p} + 2f_0} \quad (2-38)$$

By substituting $f_0 = 10^{-4}$ and different $k_\omega = 0.0, 0.5, 1.0, 1.5$ into Eq.(2-38), the evolution of damage variable with respect to the equivalent plastic strain p can be obtained as Figure 2-9. It can be seen that, for the original Rousselier model ($k_\omega = 0$), the damage variable increases with the equivalent plastic strain p even in shear deformation as shown in Eq. (2-13). The evolution of damage increases with the increasing shear damage coefficient k_ω .

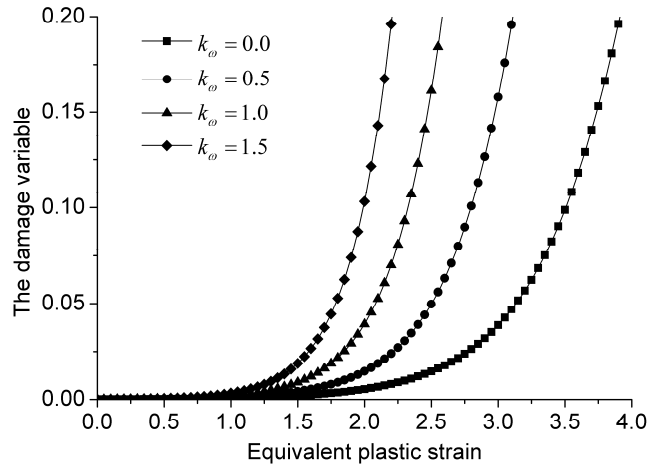


Figure 2-9 The damage variable evolutions with respect to the equivalent plastic strain p

under pure shear by modified model

Here, it should be noted one of the differences between Gurson and Rousselier models. With Gurson model, no void growth is obtained in pure shear. However, with Rousselier model, the void growth can be obtained in pure shear as presented in Figure 2-4 and 2-9. The additional phenomenological term in Eq. (2-32) could be considered as a nucleation term and not as a void growth term, because it does not comply with the mass conservation law.

The incremental of damage could be simply summed of growth and nucleation of current voids.

The $\dot{f}_{growth} = Df(1-f)\exp\left(\frac{\sigma_m}{\rho\sigma_1}\right)$ term is a monotonically nondecreasing function even for zero or negative mean stress. So, the original model can predict shear failure or compression failure possibly. But damage evolution rule may not comply with the mechanism as discussed below.

When porous metal deform, the voids may be expanded, rotated, distorted and link-up of nearby voids caused by shear stress or strain on some specific direction. The physical meaning of Eq. (2-33) can be simply illustrated as Figure 2-10. The new term $\dot{f}_{nucleation} = k_\omega f \omega(\underline{\underline{\sigma}})$ could be interpreted as:

For any unit plastic strain, the possibility for shear link-up of nearby voids is $k_{\omega}\omega(\underline{\underline{\sigma}})$.

The shear damage coefficient represents the nucleation potential of possible link-up of voids under shear. It is better to construct this behavior as *process with independent increments* or *Poisson process* in theory of probability. At least, the new term makes it possible to predict shear failure with only one more material constant.

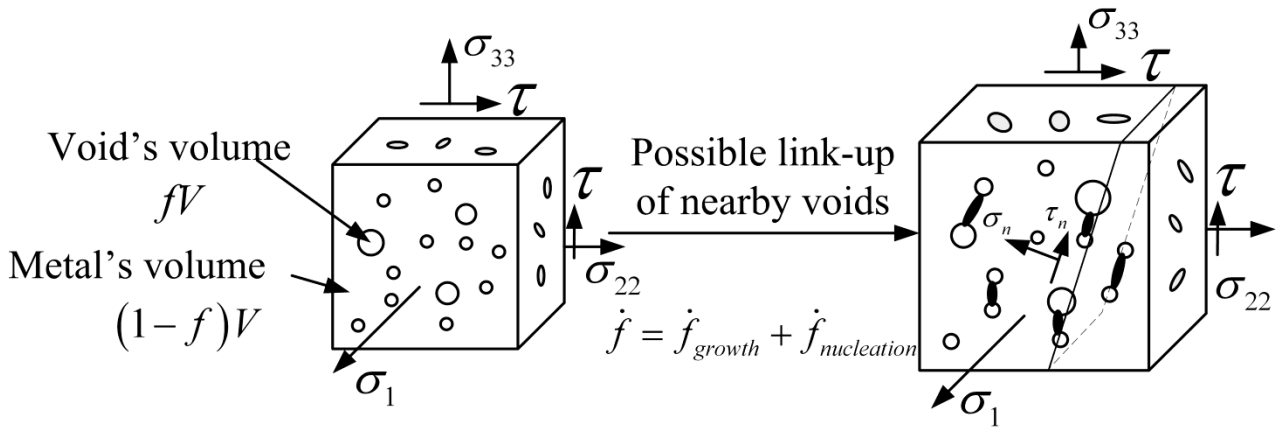


Figure 2-10 The physical meaning of the new damage evolution rule represented by possible shear link-up of nearby voids when porous metal deforms.

2.4 Brief summary

The applicability of original Rousselier model on shear is discussed and a modified model is proposed in this chapter.

1. Calibration methodology of material constants is given for original model. The yield surface in the principle stresses space are also postulated. The applicability of original Rousselier model on tension is discussed by analyzing the voids behavior under deformation.
2. A modified model is proposed by using of shear damage coefficient k_{ω} and Lode parameter $\omega(\underline{\underline{\sigma}})$ which is a metric of stress tensor approaching shear state. The incremental of damage is a summation of growth and nucleation of current voids.

3. The analytical solution of the modified model under specific loading path is derived. The effect of shear damage coefficient k_{ω} is discussed also discussed.
4. The new damage evolution rule is discussed by considering possible link-up of nearby voids under shear stress. The physical meaning is interpreted in theory of probability.

Chapter 3 Numerical implementation in FEA

In chapter 3, the numerical implementation of modified Rousselier model in finite element analysis (FEA) will be discussed. Three key subjects will be carried out. Firstly, the stress integration algorithm is deduced and briefly developed within computational plasticity framework. Secondly, the element deletion method, which can simulate the crack initiating and propagating, is briefly introduced. Thirdly, some benchmark simulations are also conducted to verify the stress integration algorithm and corresponding program.

3.1 Introduction to framework of computational plasticity

The numerical implementation of the constitutive model is well discussed in [59-61] and always developed within the framework of computational plasticity. An illustration of the basic strategy is given in Figure 3-1[59].

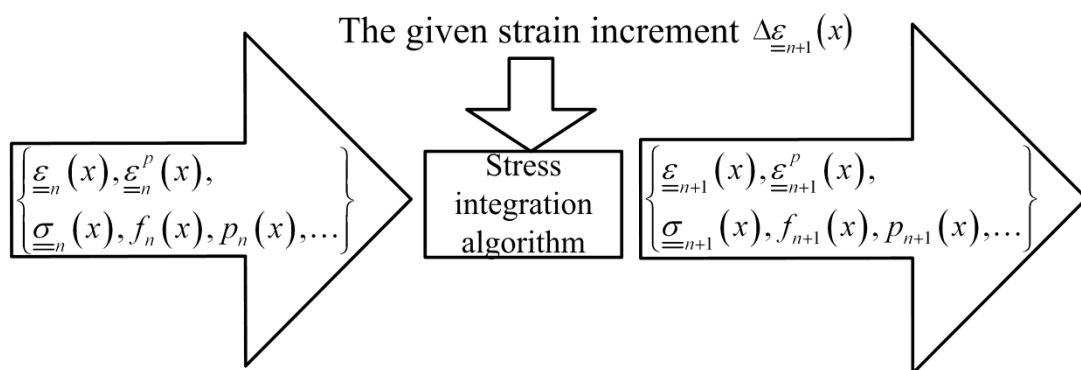


Figure 3-1 The role of stress integration algorithm.

The incremental integration of the rate-independent elastoplastic model over a time step $[t_n, t_n + \Delta t]$ is regarded as a strain-driven process[59-61] in which the total strain is the basic independent variable. The role of stress integration algorithm is to update the strain $\underline{\varepsilon}_n$, the plastic

strain $\underline{\underline{\varepsilon}}_n^p$ and other internal variables(including stress $\underline{\underline{\sigma}}_n$, damage variable f_n , equivalent plastic strain p_n , etc.) to $\underline{\underline{\varepsilon}}_{n+1}, \underline{\underline{\varepsilon}}_{n+1}^p$ ($\underline{\underline{\sigma}}_{n+1}, f_{n+1}, p_{n+1}$, etc.) by the given strain increment $\Delta \underline{\underline{\varepsilon}}_{n+1}$ as shown below:

$$\begin{cases} \underline{\underline{\varepsilon}}_{n+1} = \underline{\underline{\varepsilon}}_n + \Delta \underline{\underline{\varepsilon}}_{n+1} \\ \underline{\underline{\varepsilon}}_n^p \rightarrow \underline{\underline{\varepsilon}}_{n+1}^p, \underline{\underline{\sigma}}_n \rightarrow \underline{\underline{\sigma}}_{n+1}, f_n \rightarrow f_{n+1}, p_n \rightarrow p_{n+1} \end{cases} \quad (3-1)$$

3.2 Numerical aspect implementation

Here, stress integration algorithm and element deletion method will be briefly introduced.

3.2.1 Stress integration algorithm

The backward Euler scheme for the classical plasticity model was proposed and developed well in the past decades. The implicit algorithm was proposed for the porous model in [57, 59]. The so-called return-mapping algorithms for more general plasticity models were well discussed. All these algorithms provide higher accuracy and unconditional stability for integration of various plasticity models[57]. So, the stress integration algorithm for the modified Rousselier model is deduced and briefly developed as following within the same framework and employed in FE models.

According to Rousselier model[4, 13, 50], for an isotropic elastic material, the relation between the stress and the strain is given by

$$\underline{\underline{\sigma}} = \rho_i \underline{\underline{E}} : \underline{\underline{\varepsilon}} = \rho_i \left(\lambda Tr(\underline{\underline{\varepsilon}}) \underline{\underline{I}} + 2G \underline{\underline{\varepsilon}} \right) \quad (3-2)$$

Here, $\underline{\underline{\sigma}} = [\sigma_{11}, \sigma_{22}, \sigma_{33}, \sigma_{12}, \sigma_{23}, \sigma_{31}]^T$, $\underline{\underline{\varepsilon}} = [\varepsilon_{11}^e, \varepsilon_{22}^e, \varepsilon_{33}^e, 2\varepsilon_{12}^e, 2\varepsilon_{23}^e, 2\varepsilon_{31}^e]^T$, or written as matrix form,

$$\underline{\underline{\sigma}} = \begin{bmatrix} \sigma_{11} \\ \sigma_{22} \\ \sigma_{33} \\ \sigma_{12} \\ \sigma_{23} \\ \sigma_{31} \end{bmatrix} = \rho \begin{bmatrix} 2\mu + \lambda & \lambda & \lambda & 0 & 0 & 0 \\ \lambda & 2\mu + \lambda & \lambda & 0 & 0 & 0 \\ \lambda & \lambda & 2\mu + \lambda & 0 & 0 & 0 \\ 0 & 0 & 0 & \mu & 0 & 0 \\ 0 & 0 & 0 & 0 & \mu & 0 \\ 0 & 0 & 0 & 0 & 0 & \mu \end{bmatrix} \begin{bmatrix} \varepsilon_{11}^e \\ \varepsilon_{22}^e \\ \varepsilon_{33}^e \\ 2\varepsilon_{12}^e \\ 2\varepsilon_{23}^e \\ 2\varepsilon_{31}^e \end{bmatrix} = \rho \underline{\underline{E}} : \underline{\underline{\varepsilon}}^e \quad (3-3)$$

Here λ and μ are the bulk modulus and shear modulus, they can be expressed in terms of the Young's modulus E and the Poisson's ratio ν as $\mu = \frac{E}{2(1+\nu)}$ and $\lambda = \frac{\nu E}{(1+\nu)(1-2\nu)}$, respectively. According to the normality rule, the plastic strain rate tensor can be expressed as

$$\underline{\underline{\dot{\varepsilon}}}^p = \dot{p} \frac{\partial \Phi}{\partial (\underline{\underline{\sigma}}/\rho)} = \dot{p} \underline{\underline{a}} \quad (3-4)$$

Here $\underline{\underline{a}} = \frac{\partial \Phi}{\partial (\underline{\underline{\sigma}}/\rho)} = \frac{3\underline{\underline{\sigma}}_d}{2\underline{\underline{\sigma}}_{eq}} + \frac{1}{3} Df \exp\left(\frac{\sigma_m}{\rho\sigma_1}\right) \underline{\underline{I}}$ is the flow vector, may be written as,

$$\Delta \underline{\underline{\varepsilon}}^p = \left[\varepsilon_{11}^p, \varepsilon_{22}^p, \varepsilon_{33}^p, 2\varepsilon_{12}^p, 2\varepsilon_{13}^p, 2\varepsilon_{23}^p \right]^T = \Delta p \underline{\underline{a}} \quad (3-5)$$

The backward-Euler return algorithm is deduced by a fixed elastic predictor $\underline{\underline{\sigma}}^{tr}$,

$$\underline{\underline{\sigma}}^{tr} = \underline{\underline{\sigma}}_t + \rho_t \underline{\underline{E}} : \Delta \underline{\underline{\varepsilon}} = \underline{\underline{\sigma}}_t + \rho_t \left(\lambda Tr(\Delta \underline{\underline{\varepsilon}}) \underline{\underline{I}} + 2G \Delta \underline{\underline{\varepsilon}} \right) \quad (3-6)$$

Then the new current stress state $\underline{\underline{\sigma}}_c$ can be updated by

$$\underline{\underline{\sigma}}_c = \underline{\underline{\sigma}}^{tr} - \Delta p \rho_t \underline{\underline{E}} : \underline{\underline{a}} \quad (3-7)$$

Generally, $\underline{\underline{\sigma}}_c$ can satisfy the flow rule, while the yield condition may not be satisfied. The unknown variable Δp is required to solve by further iterations. A residual vector $\underline{\underline{r}}$, representing the difference between the current and backward Euler stress is introduced[57], in order to derive a loop to find the new stress state.

$$\underline{r} = \underline{\sigma} - \left(\underline{\sigma}^{tr} - \Delta p \rho_t \underline{E} : \underline{a} \right) \quad (3-8)$$

The only scalar variable Δp is easy to find rather than vector $\underline{\sigma}$. Assuming Δp has a small change δp , so that \underline{r} trend towards zero. So a Taylor expansion on \underline{r} can be derived as

$$\underline{r}_{new} = \underline{r}_{old} + \delta \underline{\sigma} + \delta p \rho_t \underline{E} : \underline{a} + \Delta p \rho_t \underline{E} : \left. \frac{\partial \underline{a}}{\partial \underline{\sigma}} \right|_c : \delta \underline{\sigma} \quad (3-9)$$

where $\delta \underline{\sigma}$ is the change in $\underline{\sigma}$. Setting the new residual \underline{r}_{new} to zero gives the relation of δp and $\delta \underline{\sigma}$,

$$\delta \underline{\sigma} = - \left(\underline{I} + \Delta p \rho_t \underline{E} : \left. \frac{\partial \underline{a}}{\partial \underline{\sigma}} \right|_c \right)^{-1} \left(\underline{r}_{old} + \delta p \rho_t \underline{E} : \underline{a} \right) = - \underline{Q} : \underline{r}_{old} - \left(+ \delta p \rho_t \underline{Q} : \underline{E} : \underline{a} \right) \quad (3-10)$$

here $\underline{Q} = \left(\underline{I} + \Delta p \rho_t \underline{E} : \left. \frac{\partial \underline{a}}{\partial \underline{\sigma}} \right|_c \right)^{-1}$. Further, a first-order Taylor expansion on yield condition gives,

$$\Phi(\underline{\sigma} + \delta \underline{\sigma}, f + \delta f, \Delta p + \delta p) = 0 \quad (3-11)$$

which can be expanded as

$$\Phi_{new} = \Phi_{old} + \frac{\partial \Phi}{\partial \underline{\sigma}} \delta \underline{\sigma} + \frac{\partial \Phi}{\partial f} \delta f + \frac{\partial \Phi}{\partial p} \delta p = 0 \quad (3-12)$$

Here,

$$\frac{\partial \Phi}{\partial \underline{\sigma}} = \frac{1}{\rho} \underline{a} \quad (3-13)$$

$$\frac{\partial \Phi}{\partial f} \delta f = \frac{\partial \Phi}{\partial f} \frac{\partial f}{\partial p} \delta p \quad (3-14)$$

$$\frac{\partial \Phi}{\partial f} = \sigma_{eq} \frac{1-f_0}{(1-f)^2} + D\sigma_1 \left(1 + f \frac{1-f_0}{(1-f)^2} \right) \exp \left(\frac{\sigma_m}{\sigma_1} \frac{1-f_0}{1-f} \right) \quad (3-15)$$

$$\frac{\partial f}{\partial p} = (1-f)Df \exp\left(\frac{\sigma_m}{\rho\sigma_1}\right) + k_\omega f \omega(\underline{\underline{\sigma}}) \quad (3-16)$$

$$\frac{\partial \Phi}{\partial p} = -\frac{\partial R(p)}{\partial p} \quad (3-17)$$

By solving Eq.(3-12), and the increment to plastic flow multiplier can be obtained,

$$\delta p = \frac{F_{old} - \frac{1}{\rho} \underline{\underline{a}} : \underline{\underline{Q}} : \underline{\underline{r}}_{old}}{\underline{\underline{a}}^T \underline{\underline{Q}} : \underline{\underline{E}} : \underline{\underline{a}} - \frac{\partial \Phi}{\partial f} \frac{\partial f}{\partial p} - \frac{\partial R(p)}{\partial p}} \quad (3-18)$$

Generally, an update of stress, plastic flow multiplier and damage variable must be performed and repeated according to

$$\underline{\underline{\sigma}}_c = \underline{\underline{\sigma}}_c + \delta \underline{\underline{\sigma}}_c, \Delta p = \Delta p + \delta p, f = f + \delta f \quad (3-19)$$

Finally, when the value of Φ is within a specified tolerance of zero, the iteration will be finished. The kernel of this method is that there is only one scalar variable need to solve, and can be shown in Figure 3-2.

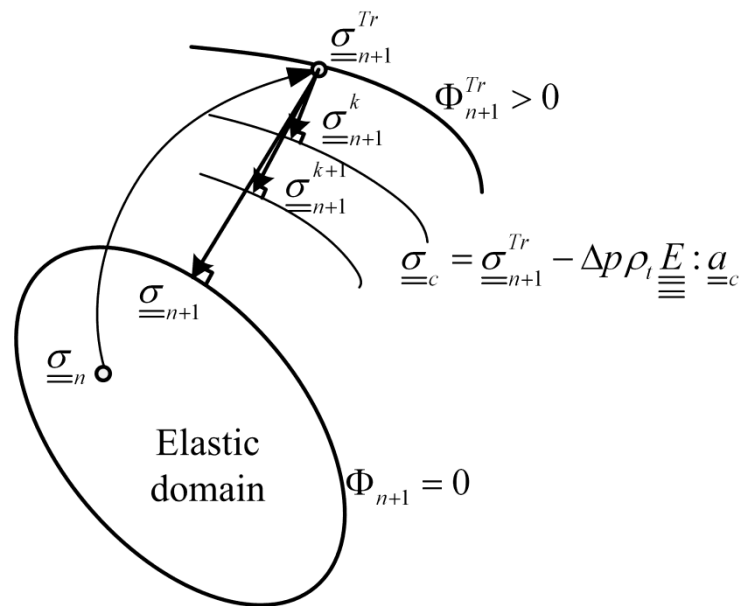


Figure 3-2 The schematic of iteration algorithm.

3.2.2 The element deletion method

This method is usually used to simulate crack in FEA[62], as shown in Figure 3-3. By setting a status variable, the element will be considered by the software (or FEA solver) when $STATUS=1$. While $STATUS=0$, the corresponding element will be deleted in the calculations forever[63, 64]. So, it is a popular way to simulate the ductile fracture[65], especially widely used of metal[20, 53, 57].

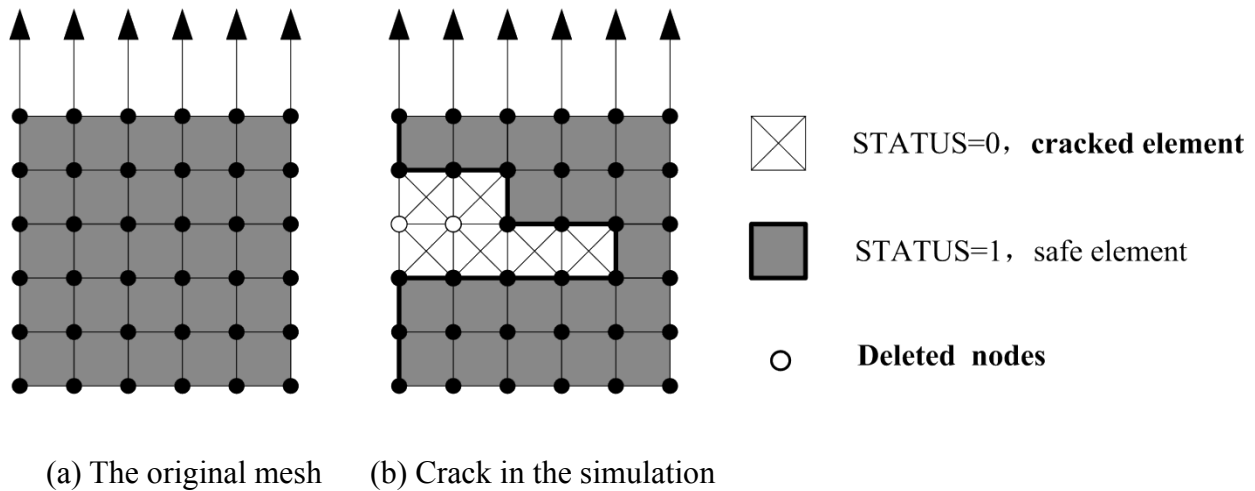


Figure 3-3 The schematic of element deletion method to simulate crack.

In this thesis, the crack criterion is set as

$$\begin{cases} STATUS = 0, & \text{if } f \geq f_c \\ STATUS = 1, & \text{if } f < f_c \end{cases} \quad (3-20)$$

here f_c is the critical void volume fraction (or damage variable).

In the commercial Abaqus/Explicit software, it is necessary to declare some state dependent variables(SDVs) in the preprocessor. The total number of SDVs is set by **Depvar*. At the same time, which variable is set as *STATUS* can also be assigned. The setting in this paper is:

**Material, name=Material-5052*

**Density*

2.7e-09,

*Depvar, delete=14

14,

*User Material, constants=34

*Element Output, directions=YES

EVF, LE, PE, PEEQ, PEEQVAVG, PEVAVG, S, SDV, STATUS, SVAVG

Here, 14 *SDVs* are declared and the 14th variable is used as *STATUS* variable. The value of all the *SDVs* are controlled by the program and some corresponding code is shown here:

```
STATEnew(13) = Dw                ! the value of  $\omega(\underline{\underline{\sigma}})$ 

if (f.le.fc) then

    STATEnew(14) = 1

else

    STATEnew(14) = 0

endif
```

Then, in the postprocessor, any variables like the distribution of $\omega(\underline{\underline{\sigma}})$ or others can be outputted. The constitutive model, corresponding numerical integration algorithm, and element deletion setting up were implemented in the Abaqus/Explicit finite element code via its VUMAT user material subroutine interface[51]. The flow chart of the subroutine is shown in Figure 3-4. It should be noticed that the crack imitation and propagation caused by damage is coupled. The developing rule for VUMAT can be found in the manual of Abaqus software[63, 64].

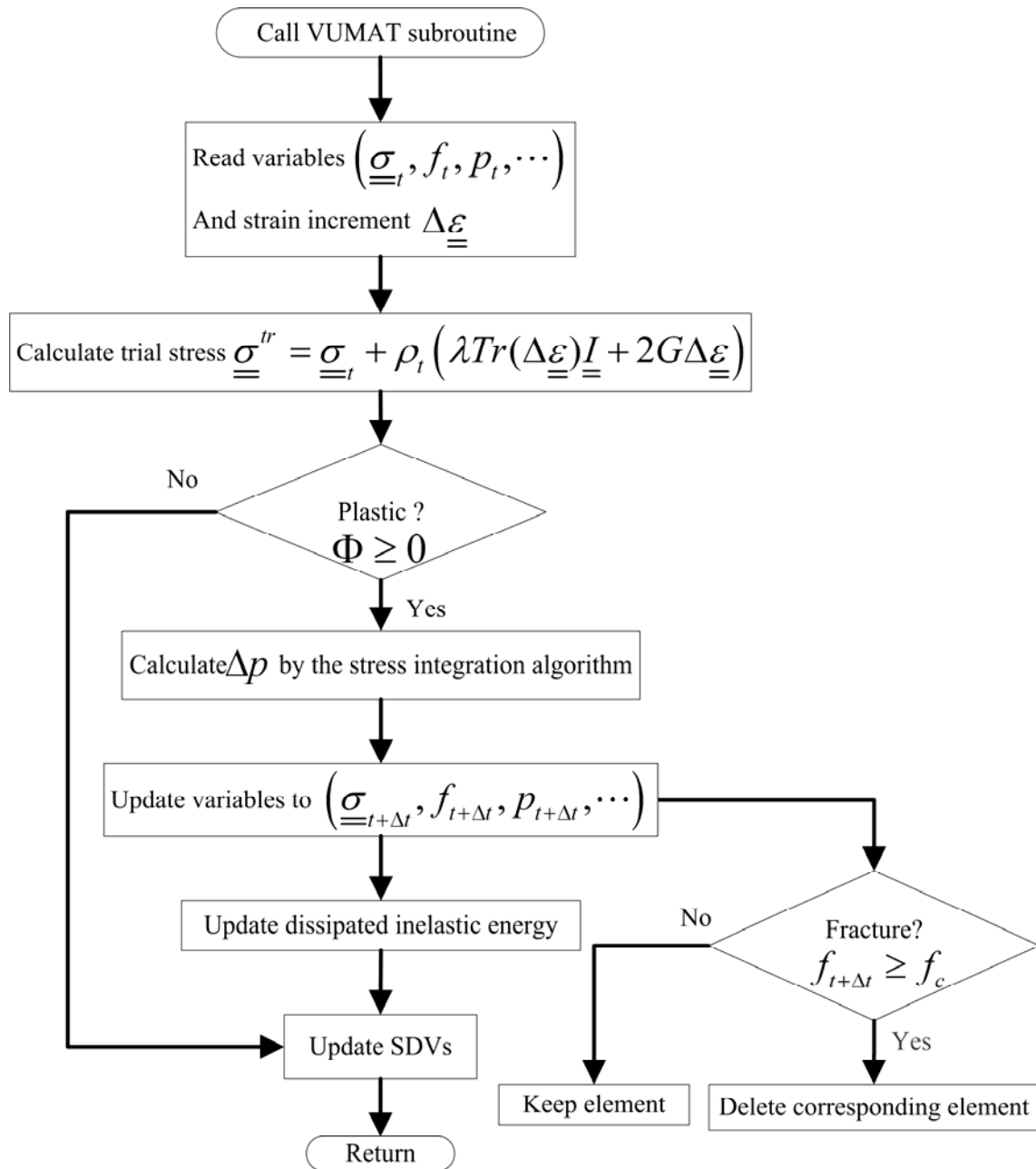


Figure 3-4 The flow chart of the program used in this paper.

3.3 Test simulations

The benchmark tests are always necessary to conduct to verify the user material subroutine[57, 66]. The verifications under shear and tension have been done. The boundary conditions in the tests should be as simple as possible and easy to compare with some know solution.

3.3.1 Verification under Shear

Here the analytical solution derived in Chapter 2 Section 2.2 is used. It can be seen that when initial void volume fraction f_0 and shear damage coefficient k_ω are determined, damage accumulation f is the sole function of equivalent plastic strain p . The f_0 is assumed as 10^{-4} . Then two different $k_\omega = 0.0, 1.5$ are chosen to simulate three different meshes for a certain material. The material size is the same cubic with dimension of $1 \text{ mm} \times 1 \text{ mm} \times 1 \text{ mm}$, while meshed by different configurations. The element type is C3D8R, which is a 3D eight node brick elements with reduced Gaussian integration and hour glass section control (provided by Abaqus/Explicit). Displacement loading are applied on the nodes of top surface, while the bottom nodes are pinned, which is a simple shear loading, as shown in Figure 3-5.

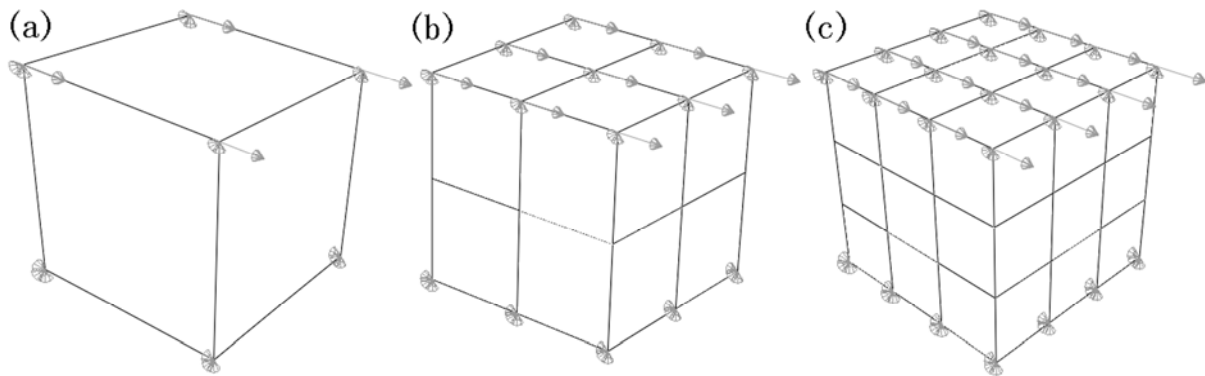


Figure 3-5 Three different mesh used to verify the user material subroutine. The same simple shear loading is applied. (a) One element, (b) Eight elements, (c) 27 elements.

The simulations are conducted in personal computer and the results are shown in Figure 3-6 and in Figure 3-7, where the evolution of damage variable is plotted as a function of the equivalent plastic strain, for $k_\omega = 0.0$ and $k_\omega = 1.5$ respectively. From these Figure 3-6 and Figure 3-7, agreement between simulations and analytical solutions can be found. The dispersivity between different meshes are negligible which implies the numerical solution is accurate to a certain extent.

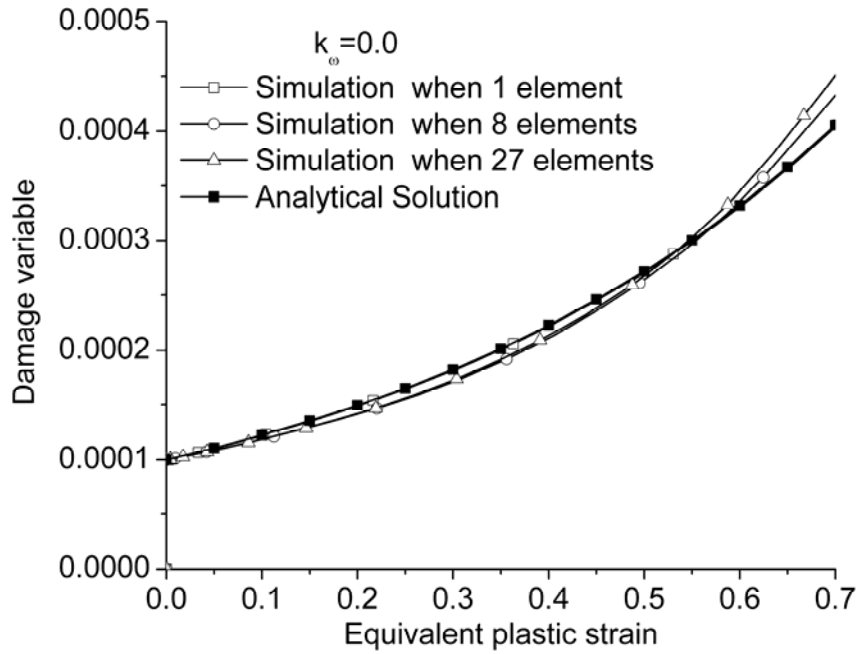


Figure 3-6 Comparison of simulation results for different mesh with analytical solution when $k_{\omega} = 0.0$.

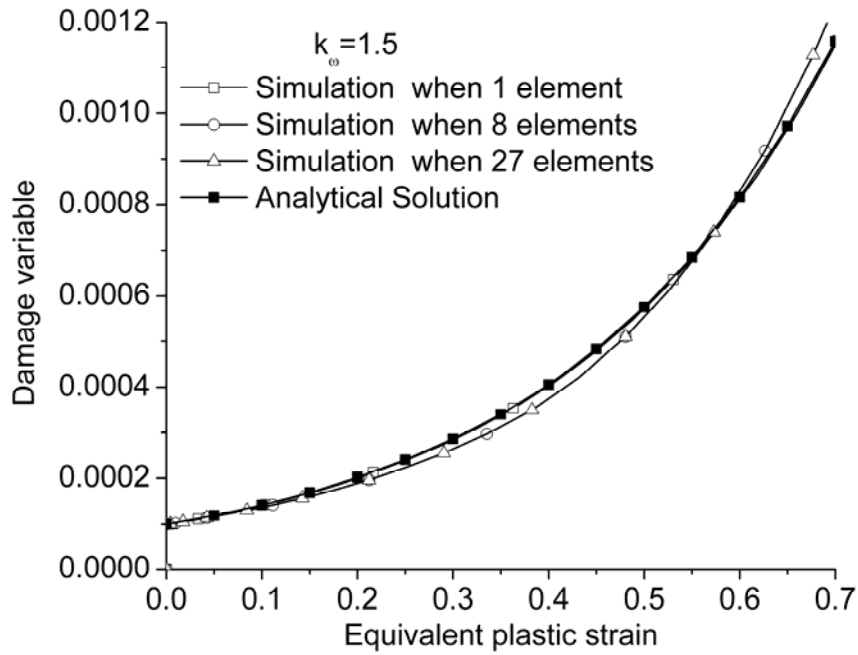


Figure 3-7 Comparison of simulation results for different mesh with analytical solution when $k_{\omega} = 1.5$.

3.3.2 Verification under Tension

Here the analytical solution is unavailable, only numerical solution under different meshes are

compared. The boundary conditions are shown in Figure 3-8. Tension loading are applied on the front surface.

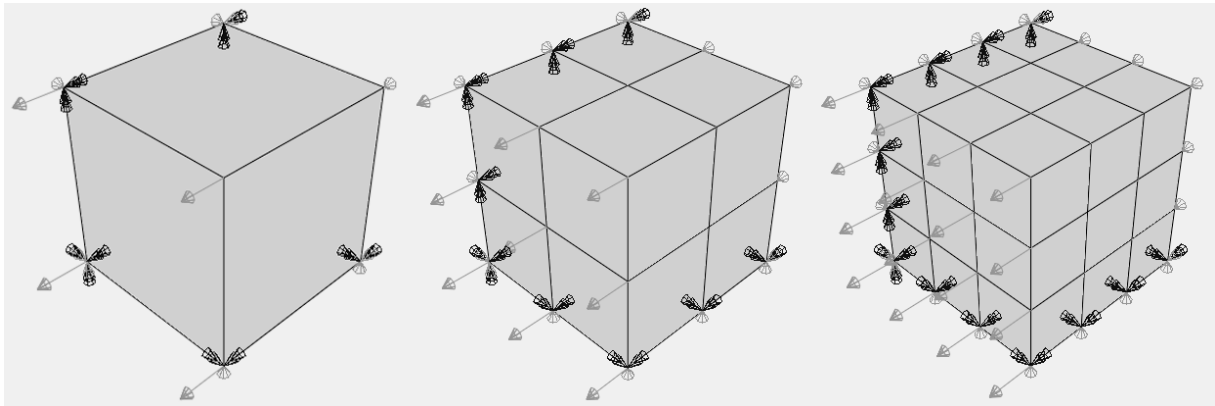


Figure 3-8 Three different mesh used to verify the user material subroutine. The same tensile loading is applied. (a) One element, (b) Eight elements, (c) 27 elements.

The Figure 3-9 shows the results for the uniaxial tensile test. The curves show the evolutions of the damage variable as a function of the equivalent plastic strain. In fact, in the case of the uniaxial tension $\xi = 1$, then the parameter $\omega(\underline{\underline{\sigma}}) = 0$. Agreement among different meshes can be found in Figure 3-9.

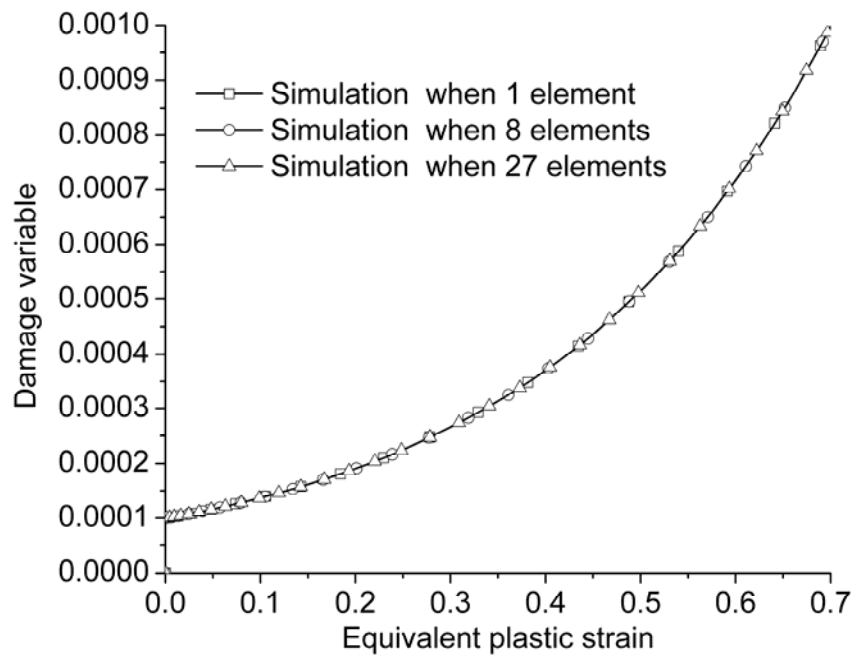


Figure 3-9 Comparison of simulation results for different mesh under tension.

3.4 Brief summary

In chapter 3, the numerical implementation aspect of modified Rousselier model is discussed.

1. The stress integration algorithm based on the return mapping method is developed. The element deletion method is employed. By using the user defined material subroutine VUMAT in the ABAQUS/Explicit platform, the integration algorithm was implemented into finite element models.

2. By using the analytical solution of damage accumulation in simple shear, the benchmark tests are conducted to verify the VUMAT subroutine and agreement between analytical solutions are achieved. The verification under tension is also conducted. The results show that the accuracy of the numerical solution is satisfied.

Chapter 4 Ductile fracture analysis of Al-alloy 5052BD-H14

In chapter 4, the ductile fracture of Al-alloy 5052BD-H14 is studied by experiments and simulations using the modified Rousselier model. The cup-cone fracture mode in tension test will be discussed.

4.1 The material and experimental procedure

Al-alloy 5052 was selected as the testing material, as it has good forming properties and is widely used in manufacturing of aircraft fuel tanks, electronic equipment panels, rivets and electrical enclosures, etc. The chemical composition is shown in Table 4-1. The major alloying element is magnesium.

Table 4-1 The chemical composition of Al-alloy 5052BD-H14 (in wt.%).

Si	Fe	Cu	Mn	Mg	Cr	Zn	Ti	Al
0.08	0.19	0.02	0.02	2.36	0.18	0.03	0.01	Re

A series of smooth round bar (SRB), notched round bars (NRB) and shear samples were prepared for a wide range of stress triaxiality[7, 14, 46]. The geometry and dimensions of specimen are presented in Figure 4-1[51]. The crosshead displacement velocity was set to 0.3 mm/min for all specimens to ensure a quasi-static deformation. The tension tests were performed by an INSTRON 1195 test machine at room temperature, using a 12.5 mm extensometer to measure the normal strain, see details in Figure 4-2. The shear tests were performed by a compression apparatus which contains a punch, a container and a basement, see details in Figure 4-3.

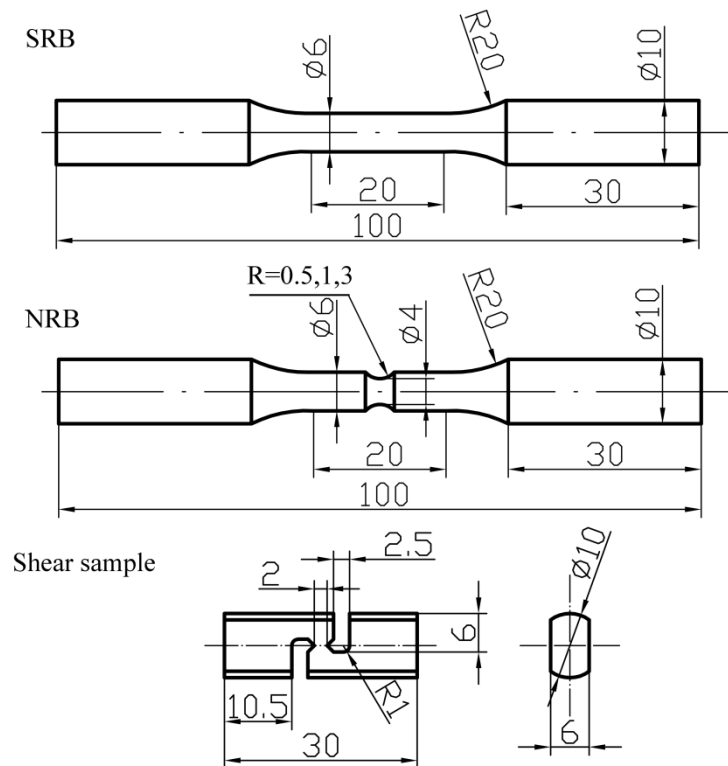


Figure 4-1 The geometry and dimensions of the Al-alloy 5052BD-H14 samples (in mm).

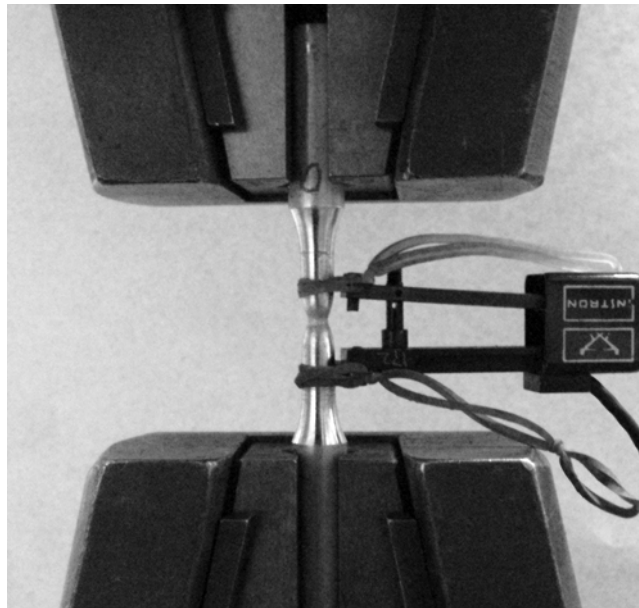


Figure 4-2 The tensile test setup.

The new type of shear test is different with the existing setup. The samples in [14, 15, 26, 67] need large dimensions. The torsion test in [68] can only be performed for tube specimens. The punch-out experiments in [32, 57] need a kind of fine blanking mold.

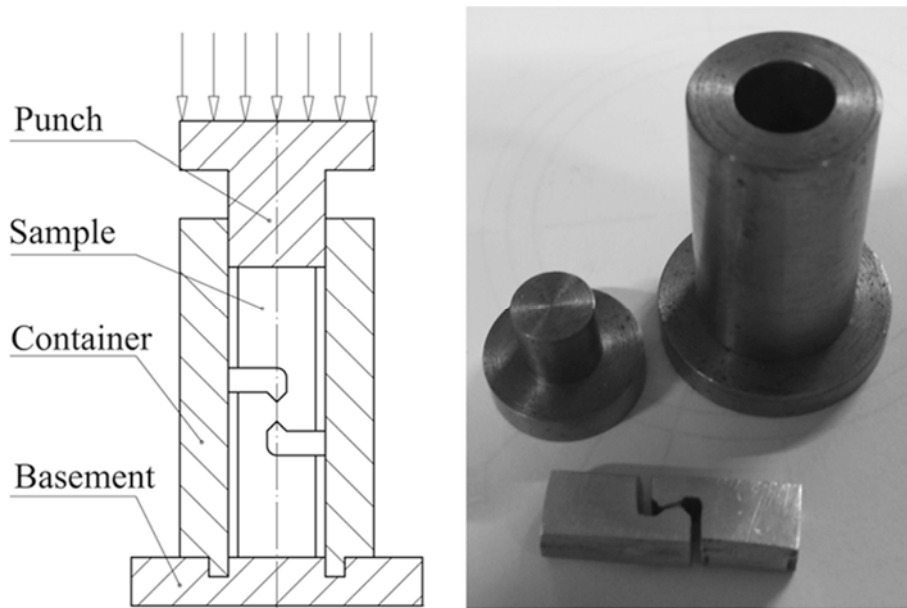


Figure 4-3 The new type of shear test.

The load F and the displacement Δl were recorded and presented in Figure 4-4. The displacements at fracture of the NRB samples show decline compared with the SRB, in other word, showing the notch sensitivity of ductile materials, for higher stress triaxiality in notched round bars[14, 15, 46].

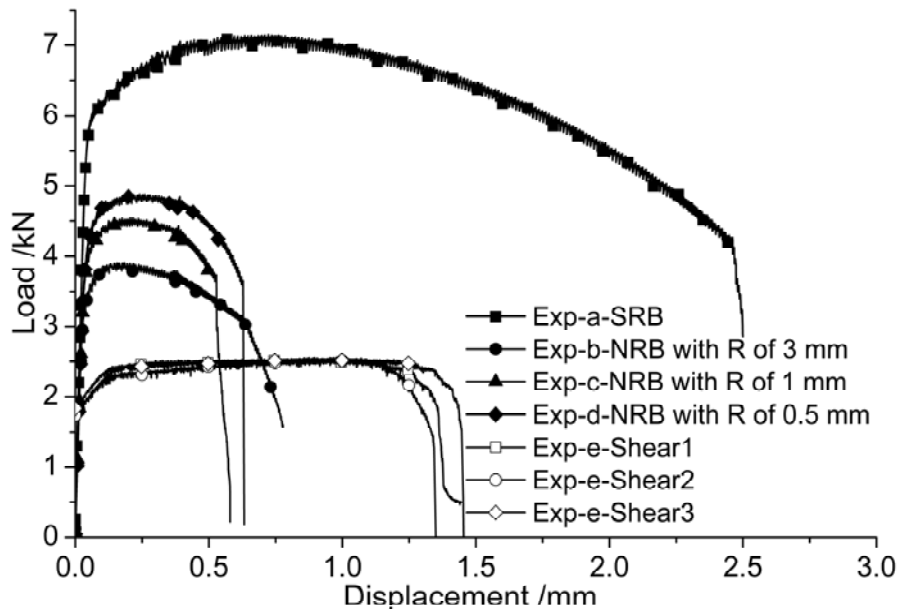


Figure 4-4 The load-displacement curves from tensile and shear tests.

4.2 SEM experiments and analysis

The fracture surfaces was observed by scanning electron microscope (SEM) to analysis the fracture mechanism. Figure 4-5, Figure 4-6 and Figure 4-7 show the SEM fractographs of tensile specimen. The cup-cone fracture mode was found in all of the SRB and NRB samples. Equi-axed ductile dimples can be found in the central region, which indicates void nucleation and growth by tensile stress or high stress triaxiality. While the cone region comprises highly elongated dimples, which indicates void coalescence by shear deformation.

The dimple characterization indicates the fracture occurs from the specimen center as the mode I crack and then grows radially (as in plane strain problem). Then the crack deviates from this path and adopts an shear path as mode II crack, thereby yielding a shear lip (as in plane stress problem). However, this explanation on the deviations in crack path or transition of crack mode is empirical rather than rigorous analysis. Some observations on the crack path or tip should be taken as a more direct approach.

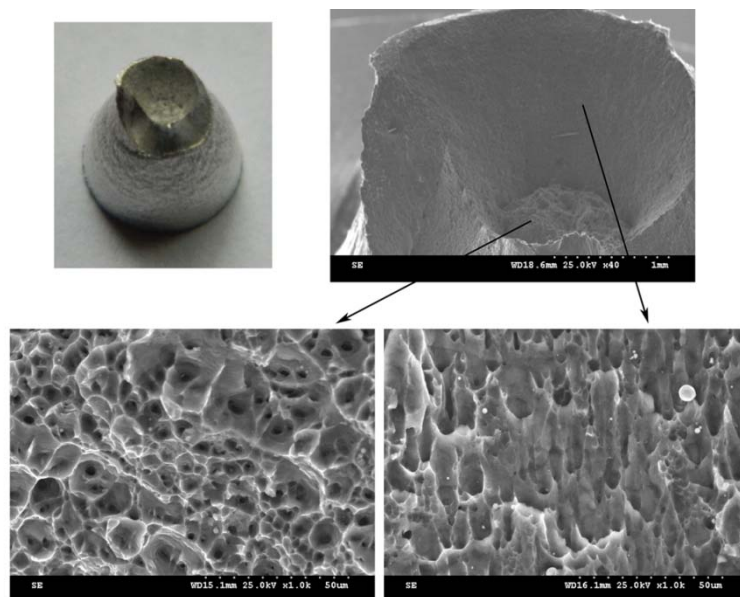


Figure 4-5 SEM fractographs of the SRB sample.

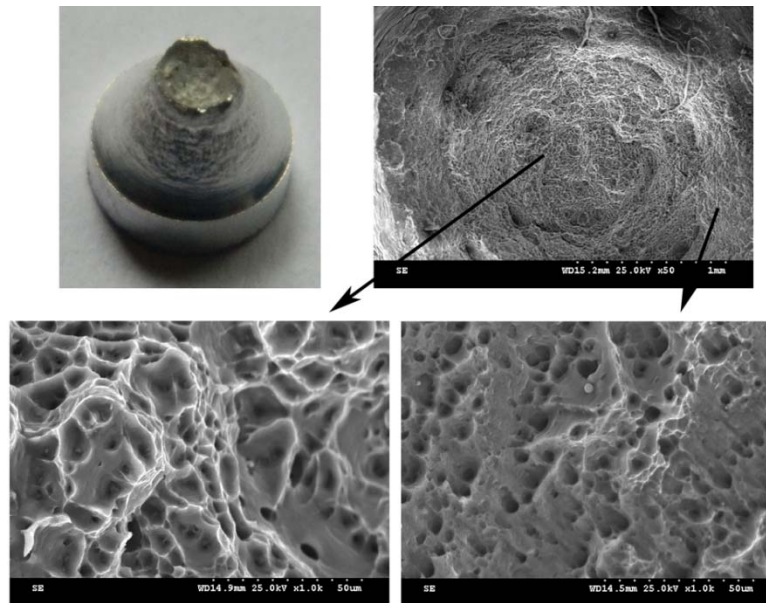


Figure 4-6 SEM fractographs of the NRB sample with R of 3 mm.

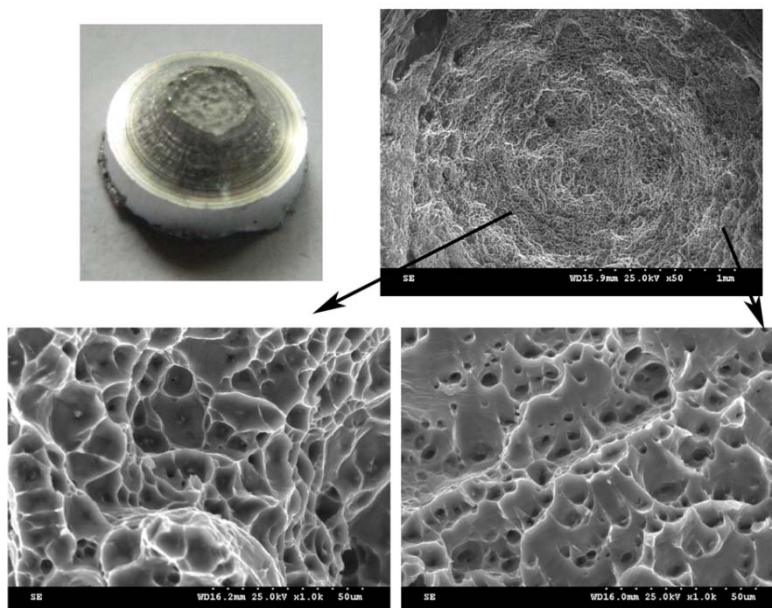


Figure 4-7 SEM fractographs of the NRB sample with R of 1 mm.

Figure 4-8 shows the longitudinal section of a sample which was not fully broken in experiment. By polishing it to the central section the SEM graph shows the center crack. It can verify that the crack occurs at the center and then grows radially. Figure 4-9 shows the void distribution near the crack tip. We can see the shear-link up of void and the potential crack propagation path. The transition from cup (mode I crack) to cone (mode II crack) is like branching

and bifurcation.

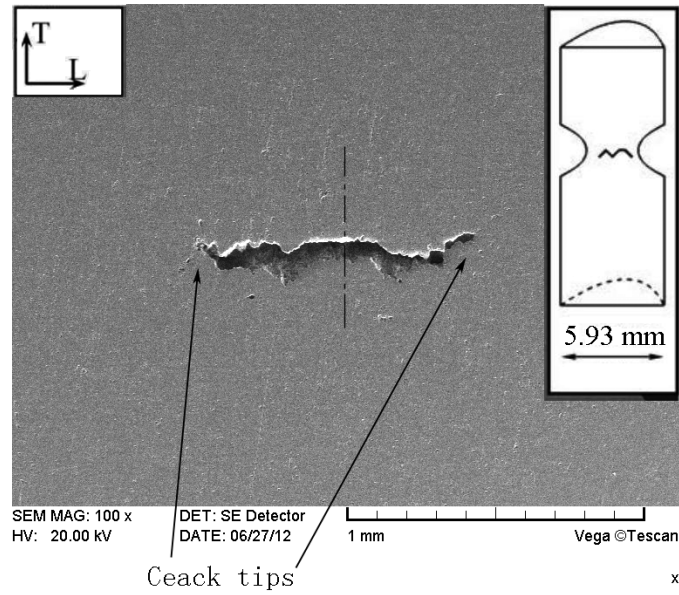


Figure 4-8 SEM graph of the center crack in SRB sample.

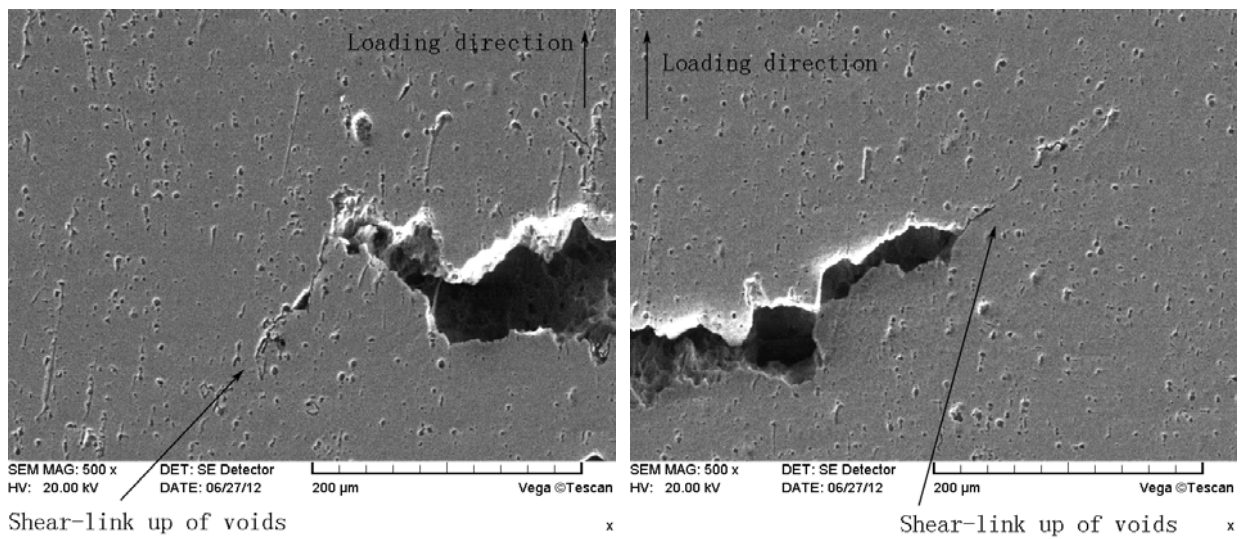


Figure 4-9 Distribution of voids at the crack tips in SRB sample.

In Figure 4-10, it can be seen that for shear specimen, there are elongated dimples, as analyzed before. However, the dimples do not cover the whole fracture surface like in the cone zone of Figure 4-5,6,7. Probably, in the shear localization region, the void grow up during shear deformation, indicating shear link-up mechanism combining with void growth.

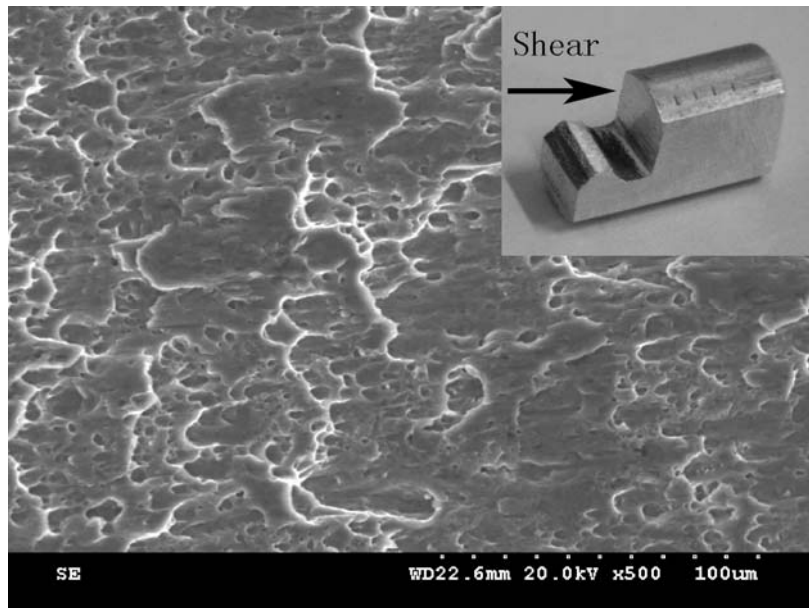


Figure 4-10 SEM fractographs of the shear sample.

4.3 Calibration material parameters

In this section, the main aims are to determine the material parameters such as the stress-strain curve in a wide range of plastic strain and the damage-related parameters. The FE meshes in this section is presented in Figure 4-11.

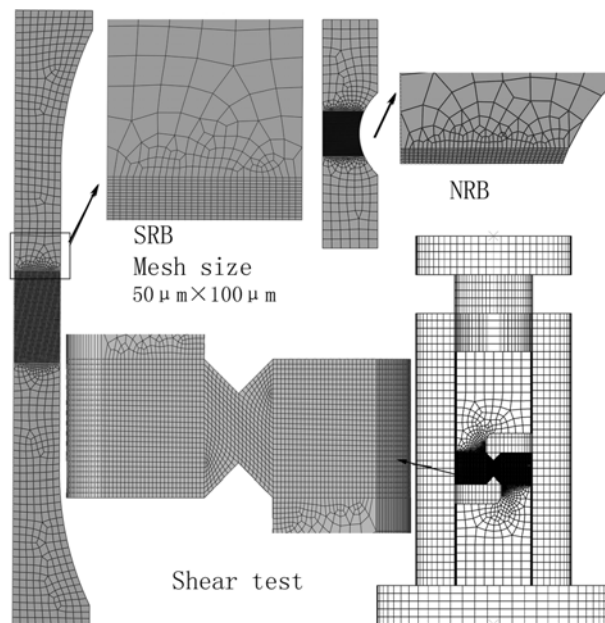


Figure 4-11 The meshes for SRB, NRB and shear test in the FEA .

4.3.1 Determination of hardening model

The material isotropy and strain-rate independence are assumed for Al-alloy 5052BD-H14. From the uniaxial tensile test, the engineering strain ε_N is obtained by $\varepsilon_N = \Delta l/l_0$ and engineering stress by $\sigma_N = F/A$, where A is the original section area of SRB sample. The engineering stress-strain curve is presented in Figure 4-12. This material shows uniform deformation, necking and fracture. Prior to necking the true strain is given by $\varepsilon_T = \ln(1 + \varepsilon_N)$, and the true stress by $\sigma_T = \sigma_N(1 + \varepsilon_N)$. Then the true plastic strain is obtained by:

$$p = \varepsilon_T - \sigma_T/E \quad (4-1)$$

E is Young's modulus, 68.9 GPa. For this material, the uniform deformation about 5%, so the Voce type hardening model is employed to extrapolate the true stress-true strain curve to a wide range.

$$R(p) = A - (A - B)\exp(-Cp) \quad (4-2)$$

By fitting, the material constants are $A = 272.2\text{MPa}$, $B = 209.6\text{MPa}$ and $C = 38.81$, respectively. The fitting results are also shown in Figure 4-12.

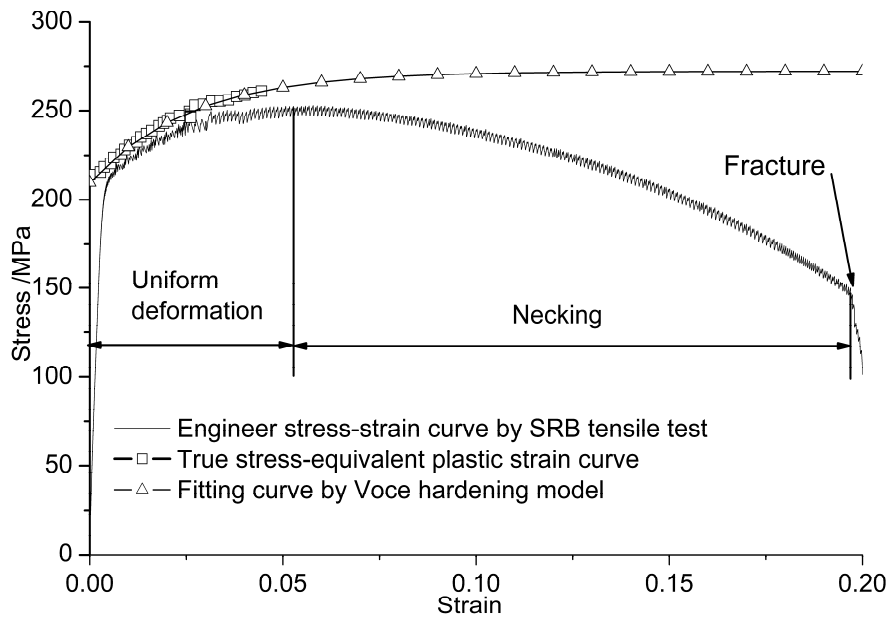


Figure 4-12 The stress-strain curve of Al-alloy 5052BD-H14 at room temperature from tensile tests.

4.3.2 Determination of σ_R and D

According to Eq. (2-4), the material parameter σ_1 can be calibrated as $\sigma_1 = 2A/3$ as 180MPa. The material parameter D is determined as 2 as in [4, 13, 50].

4.3.3 Determination of f_0 and f_c

Usually, the void consists of brittle intermetallic phase in the aluminum alloys [4, 69]. In order to identify the initial volume fraction of inclusions, metallographic investigation on polished surface of the specimens should be performed[7]. However, the exact value of initial void volume fraction f_0 is very low to determine, considering that the material is aluminum alloy. So in this section, the initial void volume fraction f_0 and the critical void volume fraction f_c are determined by a FE-based inverse fitting procedure.

According to the discussion in [31], the critical void volume fraction f_c at fracture can be chosen as 0.15 for this material and then the only unknown parameter is f_0 . Then the FE-based inverse fitting procedure in [31, 32] is employed here to determine the initial void volume fraction f_0 as follows. Three analyses were run first using the original Rousselier model, with initial void volume fraction $f_0 = 0.0001, 0.001, 0.005$ respectively. While the critical void volume fraction f_c is 0.15. The FE mesh is presented in Figure 4-10. The axis-symmetric boundary condition is chosen to simplify the simulation and the element size was $50 \times 100 \mu\text{m}$, providing 60 elements across the gauge radius. The element type is CAX4R provided by ABAQUS/Explicit, which is a bilinear axisymmetric and quadrilateral four-node element with reduced Gaussian integration.

The engineer strain-stress curves were outputted and plotted in Figure 4-13. The strain stress curves and the evolutions of the damage variable versus engineer strain obtained by simulations

with different f_0 are also shown. The damage variable increases monotonously with the deformation and the slope of the curve is very large in the end. And it can also be seen that, for $f_0 = 0.0001$, the difference between the simulation and experiment is acceptable and the damage variable evolution is in a reasonable range mentioned in other reference. So, the initial void volume fraction f_0 was calibrated as 10^{-4} for this material. The simulation results also show that the Voce model can describe the plastic hardening behavior properly.

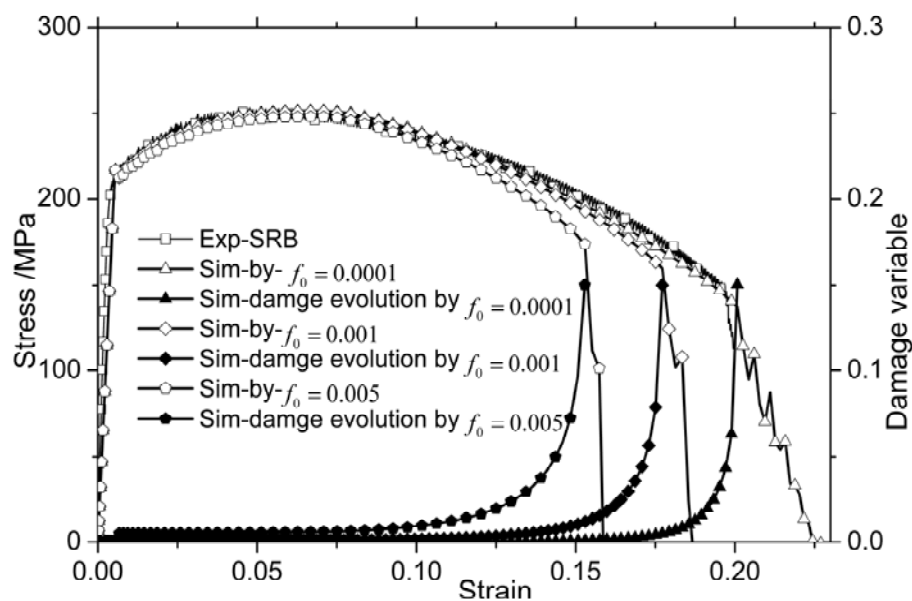


Figure 4-13 Determine the initial void volume fraction by SRB sample and FEA.

4.3.4 Determination of k_ω

In order to determine the shear damage coefficient k_ω , several analyses were run with $k_\omega = 0.0 \sim 1.5$ respectively. The displacement-load curve obtained by FE simulations are shown in Figure 4-14. It can be seen that, for increasing of the shear coefficient, the lower ductility obtained in simulation. The shear damage coefficient is fitted as $k_\omega = 1.5$ finally.

In Figure 4-15, the evolution of damage in shear test is shown as crack initiation, propagation, and final failure.

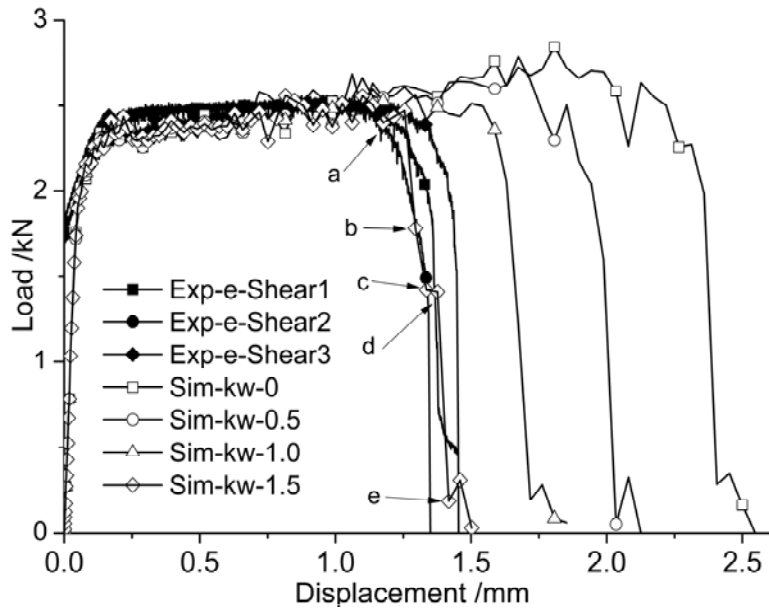


Figure 4-14 Determine the shear damage coefficient by shear test and FEA.

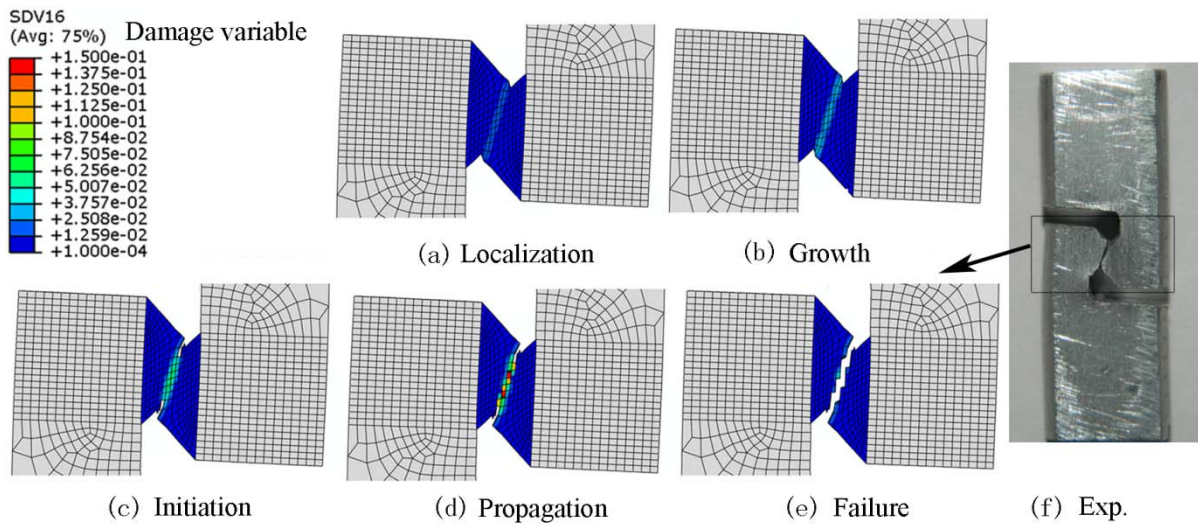


Figure 4-15 The crack initiation and propagation process in shear test by FEA.

4.4 Cup-cone fracture mode analysis

The predictive ability of the modified Rousselier model is discussed by studying the cup-cone fracture mode in SRB sample. The predicted crack trajectory of the SRB sample under tension from FEA by modified Rousselier model is shown in Figure 4-16, which indicates a cup-cone mode. Figure 4-16 also shows the distribution of the damage variable and the invariant measure $\omega(\underline{\underline{\sigma}})$.

We can see that the simulation results by the modified model can predict the fracture process of the specimen. First, the localization phenomenon occurs as a result of high triaxiality in the center. Then the porosity band branches to two shear bands, and the void evolution is influenced by shear localization. For the extended void evolution model incorporating with shear, the void coalescence along the shear bands so that the crack propagates along one of the shear bands correspondingly resulting as bifurcation. When one of the bands is selected and the symmetry of the structural is lost, finally the ultimate fracture is became cup-cone mode. We can see that for the modified Rousselier model, the new damage evolution function is influenced by the Lode parameter, so that the ductile damage evolution mechanisms under shear deformation can be described by the modified model.

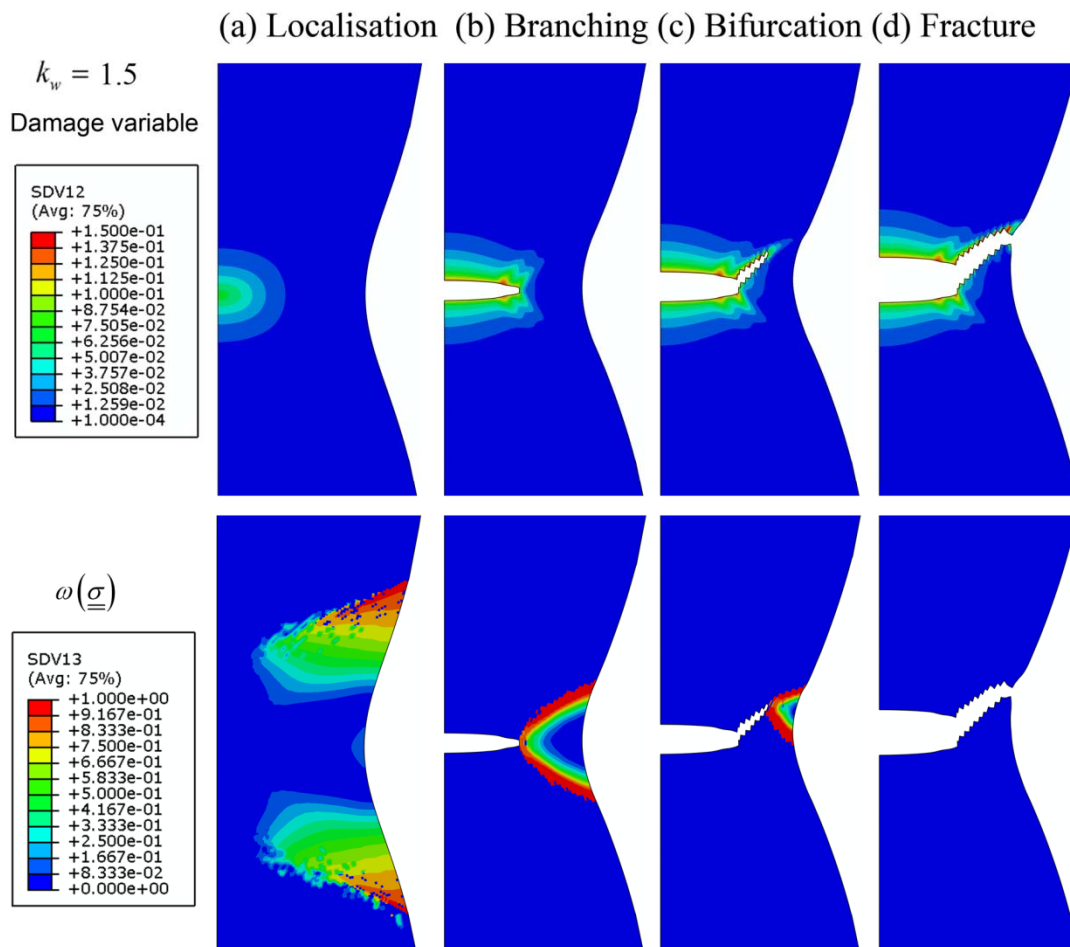


Figure 4-16 The ductile fracture process in SRB sample by FEA.

Figure 4-17 presents the comparison of the load-displacement curves from numerical simulations with the experimental results. Good agreement can be found between the numerical and the experimental results. The points marked in Figure 4-17 correspond to the stages (a) localization, (b) branching, (c) bifurcation and (d) fracture in Figure 4-16.

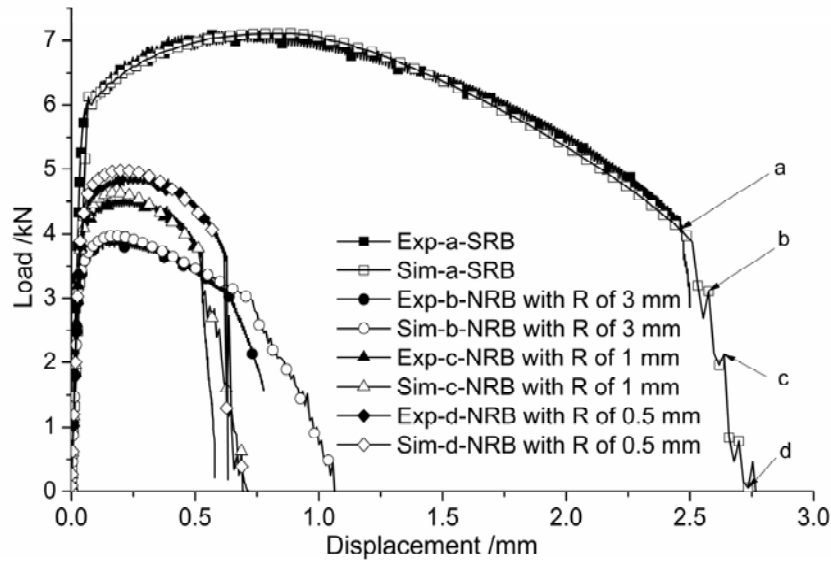


Figure 4-17 Comparisons of simulation and experimental results.

The fracture mechanism can be concluded as Figure 4-18, which is a schematic diagram of the stress and strain-driven ductile damage evolution mechanisms under large deformation. It can be seen that the micro-voids nucleate with plasticity deformation, although their growth is driven only by the tensile stress. Micro-voids can also coalesce by shear stress on some direction. The final distribution of micro-voids may be the summation of growth by tension and coalescence by shear.

4.5 Brief summary

1. The material parameters were calibrated by an FE based inverse method. By uniaxial tension test, the initial void volume fraction f_0 and critical void volume fraction f_c were calibrated as 0.0001 and 0.15 for Al-alloy5052BD-H14, respectively. By a new type of shear test, the shear

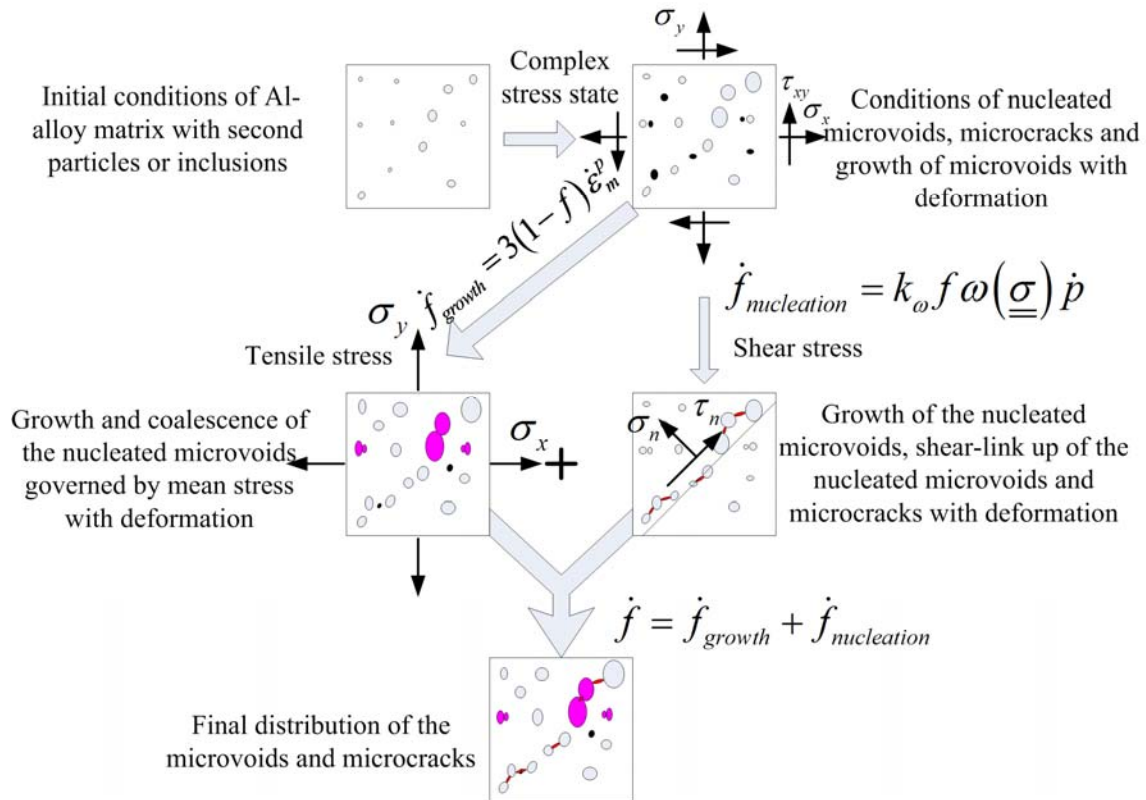


Figure 4-18 Ductile fracture mechanism of Al-alloy 5052-BD-H14.

coefficient k_ω was calibrated as 1.5 for this material. The simulation results show that the modified model can give accurate results for the shear type failure.

2. The predictive capability of this model was carried out by studying the cup-cone fracture mode in the tensile tests. The validity of this model was verified by comparing the experiments with the simulations and good agreement was achieved. The results show that the new damage evolution function which is influenced by the metric of the stress can describe the void evolution mechanisms under shear deformation. So, the predictive ability of the modified Rousselier model was improved by the extended damage evolution model.

3. The possible fracture mechanism under complex stress state is analyzed. The distribution of micro-voids may be the summation of growth by tension and coalescence by shear.

Chapter 5 Ductile fracture analysis of Al-alloy 5052P-H34

In chapter 5, the ductile analysis of Al-alloy 5052P-H34 will be started. The physical experiments were conducted and fracture mechanism was analyzed. Consequently, the material parameters were identified by an inverse method using these experimental data. A shear test was also performed to calibrate the new shear coefficient in the modified Rousselier model. A benchmark test was also performed to verify the model applicability.

5.1 The material and experimental procedure

The Al-alloy 5052P-H34 has good corrosion resistance, weld-ability, cold workability, and medium strength. The chemical composition is shown in Table 5-1. The major alloying element is magnesium. The material is sheet and 2.0 mm in thickness.

Table 5-1 The chemical composition of Al-alloy 5052P-H34 (in wt.%).

Si	Fe	Cu	Mn	Mg	Cr	Zn	Ti	Al
0.08	0.27	-	-	2.63	0.19	-	-	Re

A series of specimens, namely tensile specimen, notched tensile specimen, shear specimen, and center hole specimen, were prepared by Electrical Discharge Machining (EDM). The geometry and dimensions of specimen are presented in Figure 5-1 and Figure 5-2. The tensile specimen were sampled in three directions namely rolling direct(RD), transverse direction(TD), 45 degree with RD. This experimental design is a common way to obtain a wide range of stress triaxiality and different fracture mechanisms. For the structure material, the mode I crack is common and dangerous.

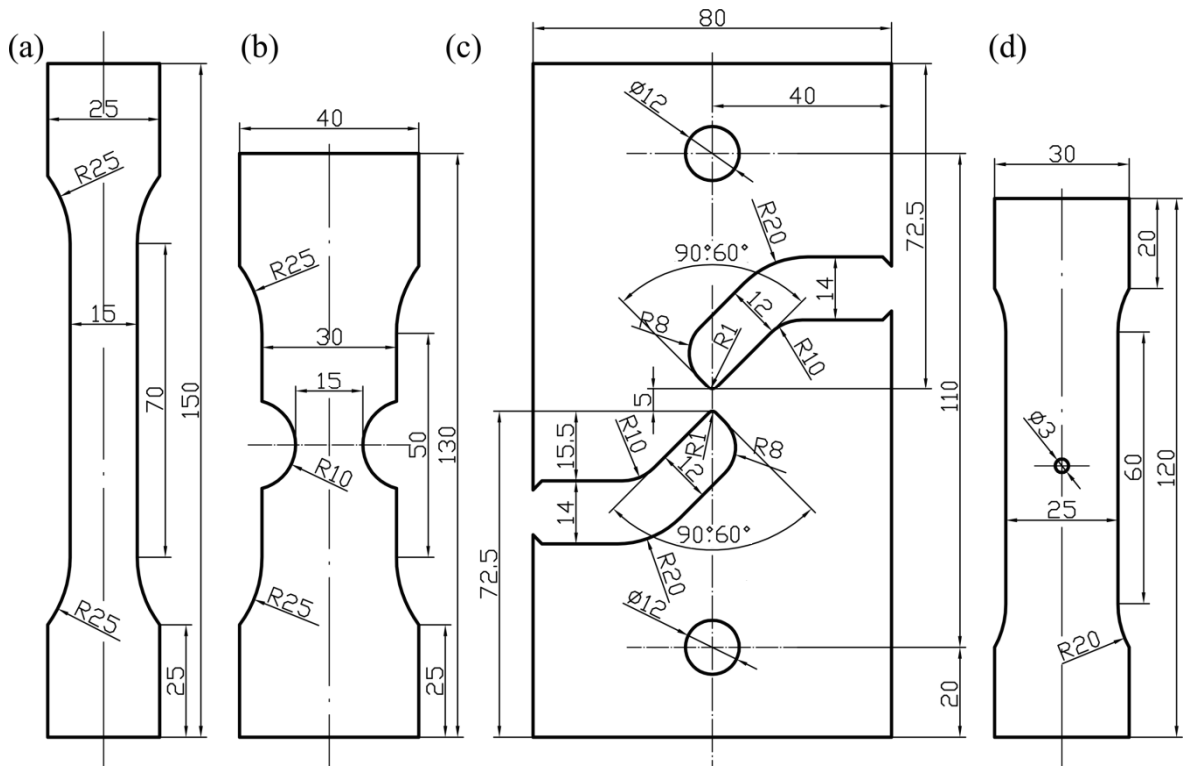


Figure 5-1 The geometry and dimensions of samples(in mm). (a) Tensile specimen, (b) Notched tensile specimen, (c) Shear specimen, (d) Center hole tensile specimen.

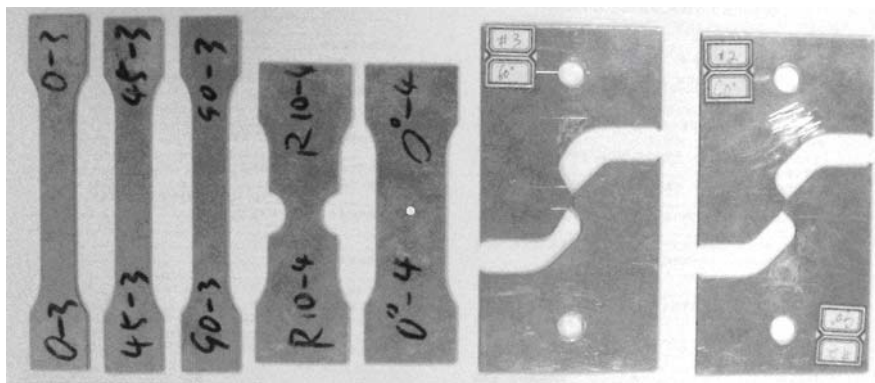


Figure 5-2 The samples prepared by EDM.

The tension tests were performed by an INSTRON 1195 test machine at room temperature. The crosshead displacement velocity was set to 2.0 mm/min for all tensile specimens and 0.3 mm/min for shear specimens, to ensure a quasi-static deformation, respectively. For the sample (a), (b), (d), the normal strain was measured using an extensometer over 50 mm within the gauge section (Figure 5-3a). But for the shear specimen, experimental setup concludes two fixtures, two pins and two

supports bounded on the samples. A general 10 mm crack opening displacement (COD) clip gauge, which is usually employed in COD test, is used to measure the displacement between two supports here(see details in Figure 5-3b).

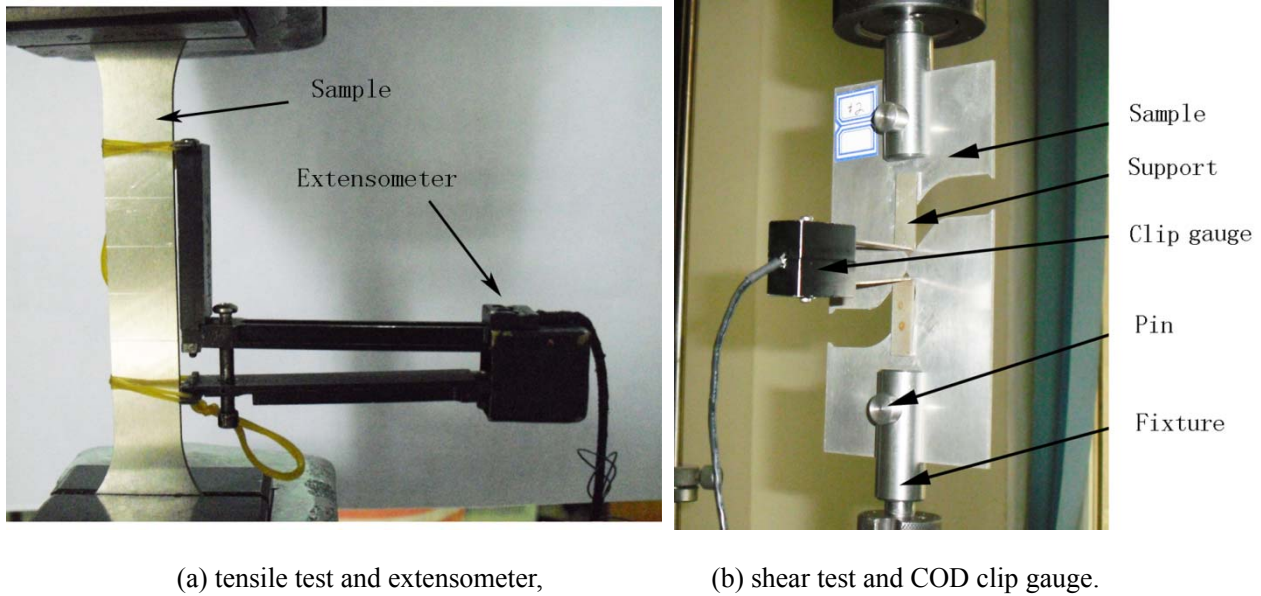


Figure 5-3 The experimental setting up.

5.2 Results and analysis

Figure 5-4 shows the macroscopic fracture phenomenon, the shear fracture is found in uniaxial tensile and shear tests. For Notched tensile specimen, failure type is tension fracture. For Center hole tensile specimen, the crack initiates at the hole for stress concentration and then mode I crack.

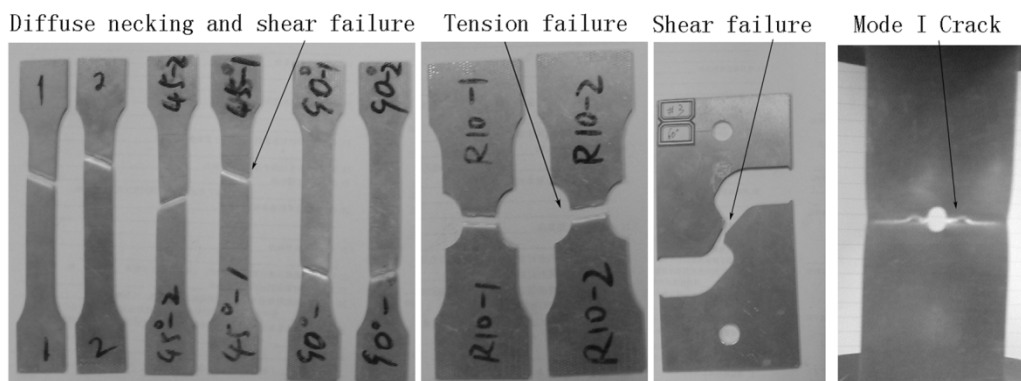


Figure 5-4 Macro morphology of different tests.

Figure 5-5 shows the SEM photograph of shear specimen, it can be seen that the crack surface comprises highly elongated dimples, which indicates the shear link-up mechanism.

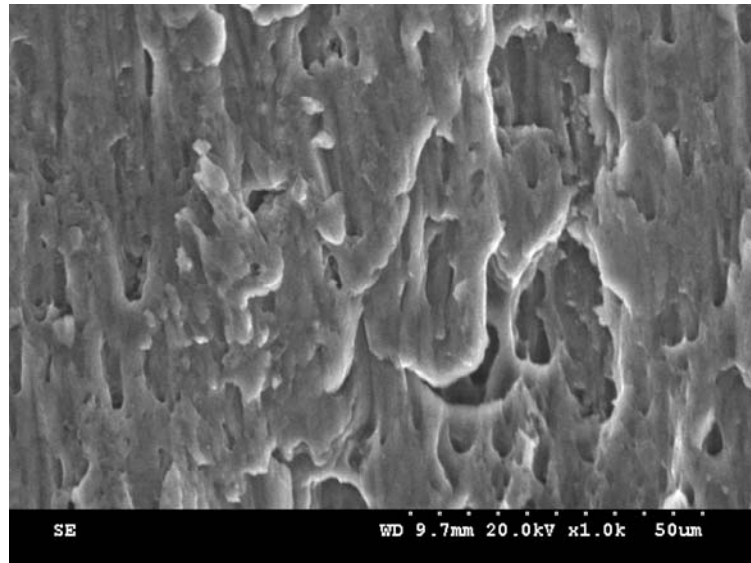


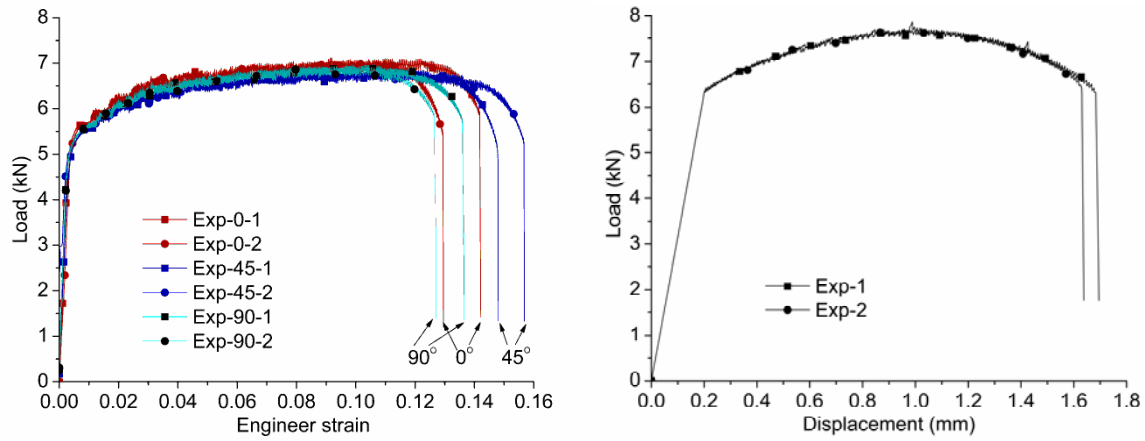
Figure 5-5 SEM photographs of the shear specimen.

The relation between test category and ductile fracture features are summarized in Table 5-2.

Table 5-2 Test category and ductile fracture features.

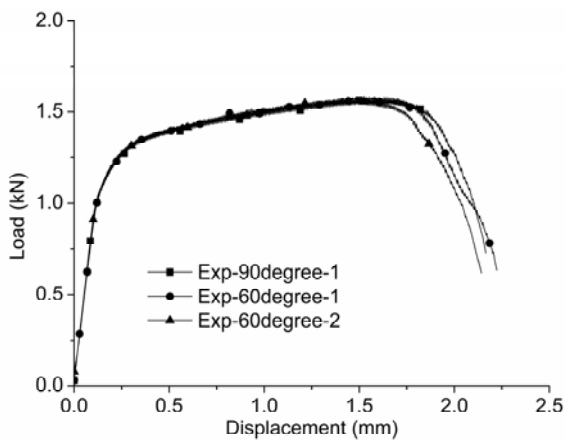
Test category	Number	Triaxiality	Ductile fracture feature
Uniaxial tensile test	a	1/3	Diffused necking to shear failure
Notched tensile test	b	0.65	Tension failure
Shear test	c	0	Shear failure
Center hole tensile test	d	1/3	Stress concentration to mode I crack

The load F and the displacement Δl over the gauge section were recorded and presented in Figure 5-6. Noting that the uniaxial tensile tests results along three directions are closed to each other, then the material isotropy is conceived. There is a decline of ductility in notched and center hole specimen, for high stress concentration in the center. The results in all shear tests are closed to each other.

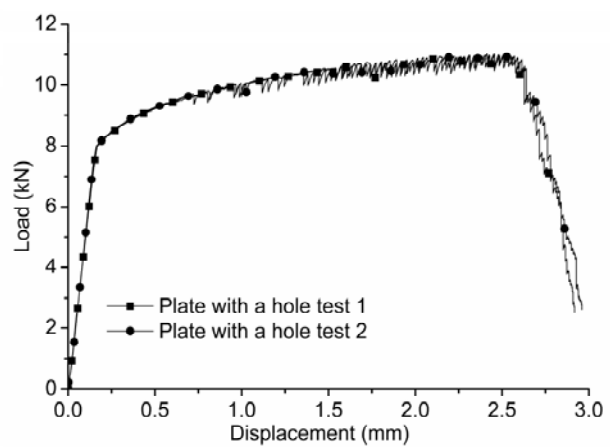


(a) Uniaxial tensile test along three directions,

(b) Notched specimen tensile test.



(c) shear test,



(d) Center hole tensile test.

Figure 5-6 The experimental displacement-load curves.

5.3 Determination of the material constants

In this section, the main aims are to determine the material parameters by a FE-based inverse procedure. Firstly, the stress-strain curve in a wide range of plastic deformation will be determined. Secondly, σ_R and D are determined. Thirdly, the initial void volume fraction f_0 and the critical damage variable f_c are calibrated by notched tensile test. Finally, the shear damage coefficient k_ω is determined from shear test.

The FE meshes and boundary conditions are shown in Figure 5-7. The elements type is S4R for

uniaxial tensile specimen, with 5 integration points across the thickness. For other specimens, the element type is C3D8R (in ABAQUS/Explicit), which is a linear 8-node element with reduced Gaussian integration. The clamps were modeled as reference points and coupling with the hole surfaces. The movement of the crosshead is represented by a displacement boundary condition. The smooth step is chosen as 0.01 s to ensure a quasi-static deformation. For the shear region, severe element distortion occurs, and the arbitrary Lagrange-Euler (ALE) adaptive mesh control is used.

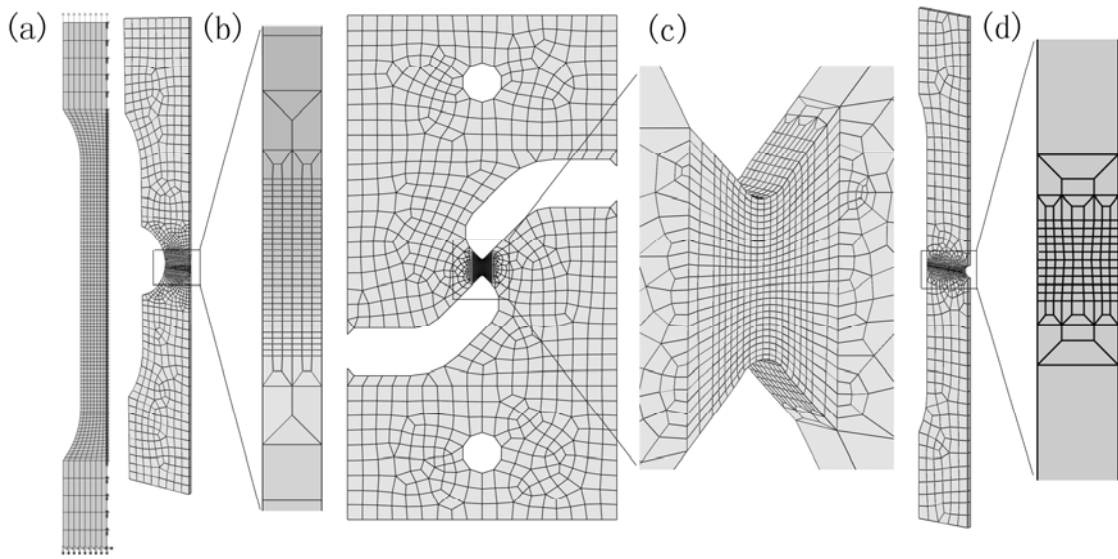


Figure 5-7 Mesh of different tests. Noting that mesh graduation is employed to reduce simulation time.

5.3.1 Determination of hardening model

From the uniaxial tensile test, the nominal strain ε_N can be obtained by $\varepsilon_N = \Delta l/l_0$ and nominal stress by $\sigma_N = F/A$, where l_0 is the gauge length and A is the section area of the sample. Prior to necking the true strain is given by $\varepsilon_T = \ln(1 + \varepsilon_N)$, and the true stress by $\sigma_T = \sigma_N (1 + \varepsilon_N)$. By using Hook's law,

$$\varepsilon_T^p = \varepsilon_T - \sigma_T/E \quad (5-1)$$

the true plastic strain and true stress relation can be get. Here ε_T^p is the true plastic strain or

equivalent plastic strain and E is the Young's modulus. The true stress-equivalent plastic strain curves are presented in Figure 4-7. For this material, the Voce hardening model [52] was employed to fit the true stress-true strain curve before necking

$$R(p) = A - (A - B)\exp(-Cp) \quad (5-2)$$

By fitting, the constants are $A = 264.5$ MPa, $B = 182.8$ MPa, $C = 24.51$ respectively.

The strain hardening behavior can only be determined up to an equivalent plastic strain of 10% from a uniaxial tensile experiment (due to the onset of necking). An inverse approach is taken to extrapolate the hardening curve to large strains based on the experimental data[70]. First, the extend part is presented as a constant hardening modulus k was assumed. An FE-based optical method is employed to find the most suitable value of k [32]. A preliminary estimate of k was obtained by a least squares fit of the small strain data. A series of FE computations was then performed to find k , which satisfy the experiments results. Finally, the fitting result is $k = 66.25$ MPa and also shown in Figure 5-8. The verification simulation results are shown in Figure 5-9 and agreement can be found.

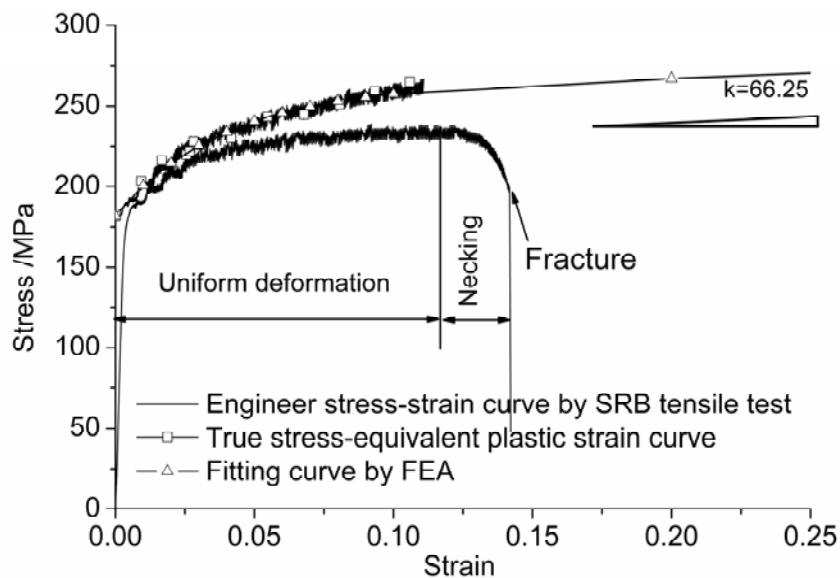


Figure 5-8 The true stress-strain curve of A5052P-H34 at room temperature from tensile tests. The fitting curve by the Voce hardening models and fitted hardening modulus from FEA are also shown.

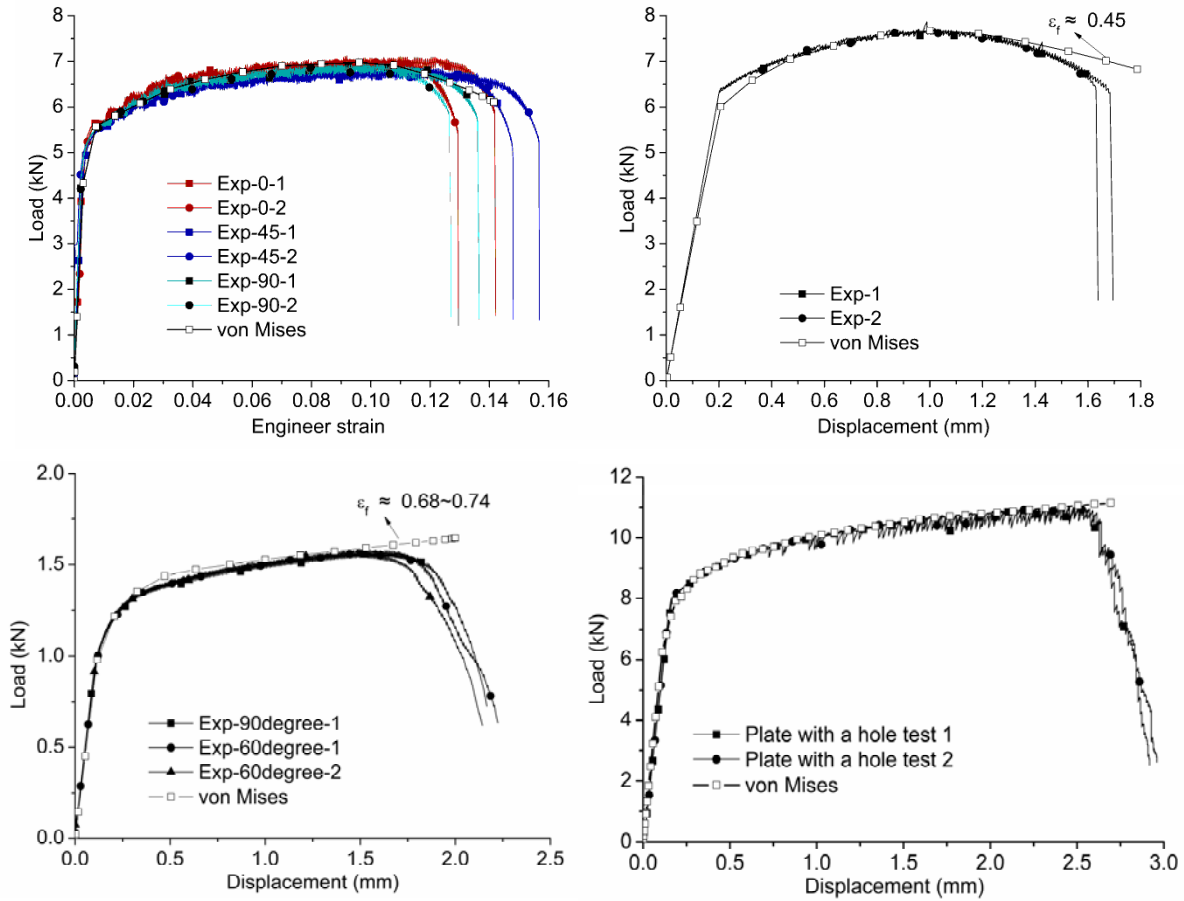


Figure 5-9 The materials response calculated by FEA and comparing with experimental results.

5.3.2 Determination of σ_R and D

As mentioned in Eq. (2-4), $\sigma_R \approx 2A/3$, then $\sigma_R \approx 177$ MPa. And $D = 2$ is selected[13].

5.3.3 Determination of f_0 and f_c

The critical damage variable f_c is chosen as 0.15 for that the initial void volume fraction f_0 is always small according to [31]

$$f_c = 0.15 + 2f_0 \quad (5-3)$$

Then f_0 is fitted by a fixed f_c using FE simulations. The notched specimen tensile test data is employed since the ductile fracture feature is tensile deduced. The fitting results are shown in Figure 5-10. f_0 is chosen as 0.001 finally.

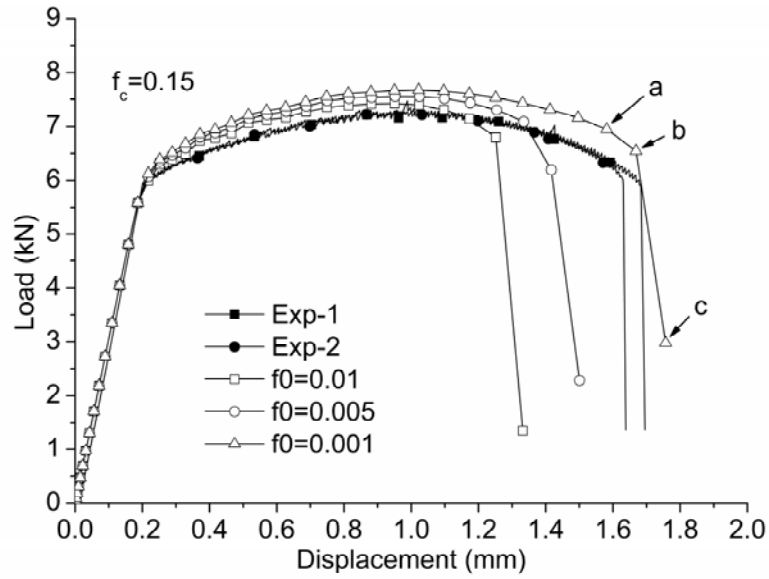


Figure 5-10 The fitting procedure for f_0 by a fixed f_c .

5.3.4 Determination of k_ω

Five plane strain analyses were run with $k_\omega = 0.0 \sim 2.0$, respectively. As shown in Figure 5-11, the Rousselier model can predict shear failure, for $k_\omega = 0$. But the displacement-load curve shows that the ductility is over-estimated. From the Figure 5-10, k_ω can be determined as 1.5~2.0.

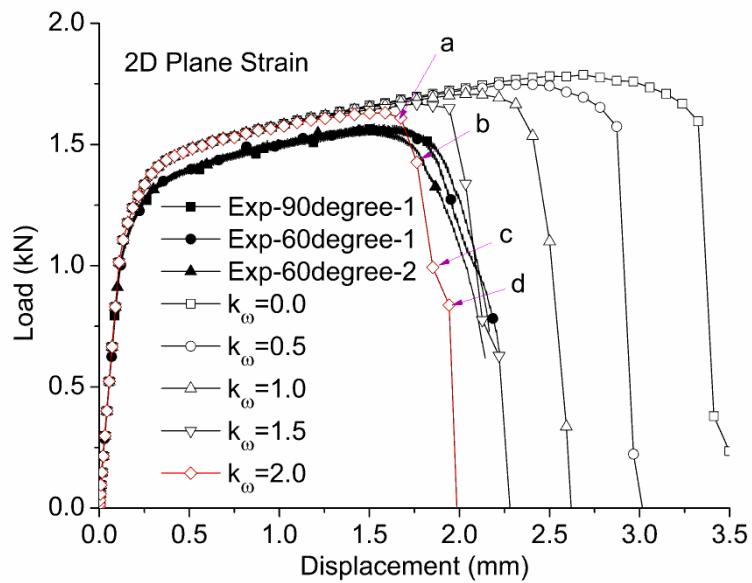


Figure 5-11 The fitting procedure for k_ω by 2D plane strain simulations.

The load is greater than tests for that not all the material is plane strain along thickness. More detailed analysis by 3D simulation gives that $k_{\omega} = 2.0$, as shown in Figure 5-12. The damage initiation, crack propagation, and final failure in shear obtained by modified Rousselier model are presented in Figure 5-13. It should be noted that the cracks initiate at the round corner for stress concentration.

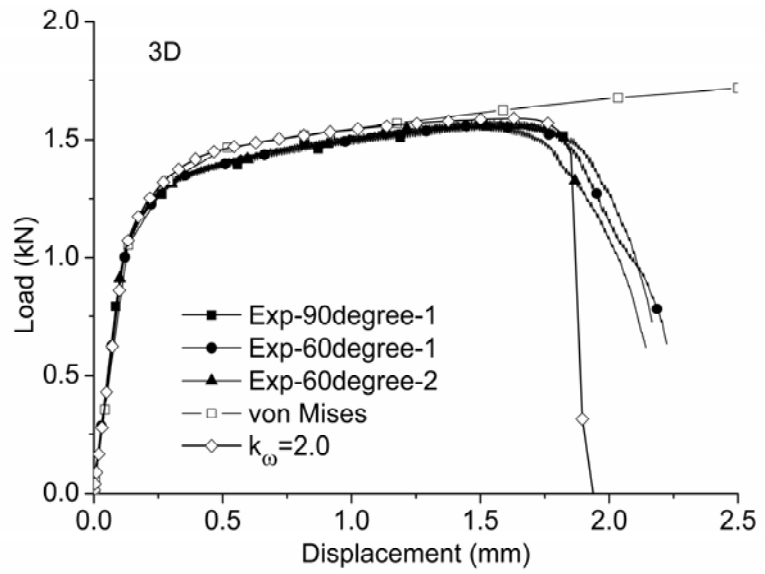
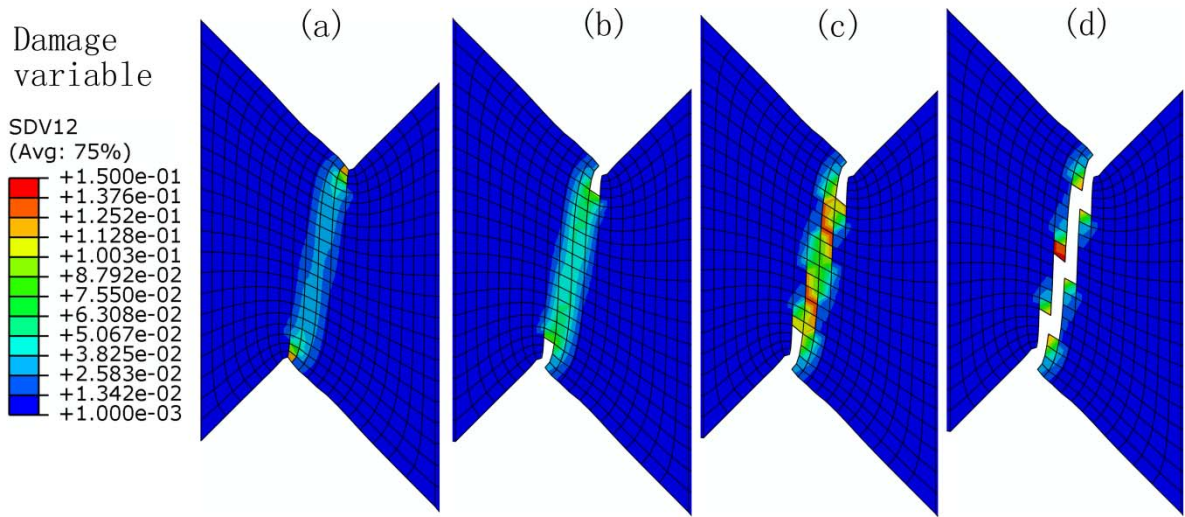


Figure 5-12 The fitting procedure for k_{ω} by 3D simulation.



(a) Concentration, (b) Crack initiation, (c) Crack propagation, (d) Final failure

Figure 5-13 The damage evolution of shear test by modified model.

5.4 Verification and Sandia test

5.4.1 Verification

As a verification, the center hole sample with tension load is also simulated to obtain damage distribution and shown in Figure 5-14. The comparison of displacement-load curves from experiments and simulations are also shown in Figure 5-15 and agreement was achieved.

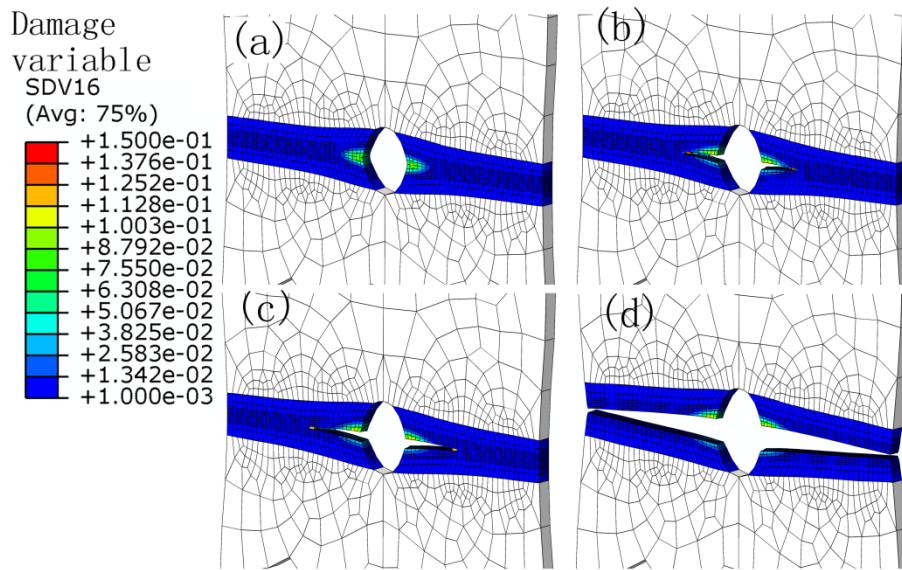


Figure 5-14 The damage evolution of center hole sample.

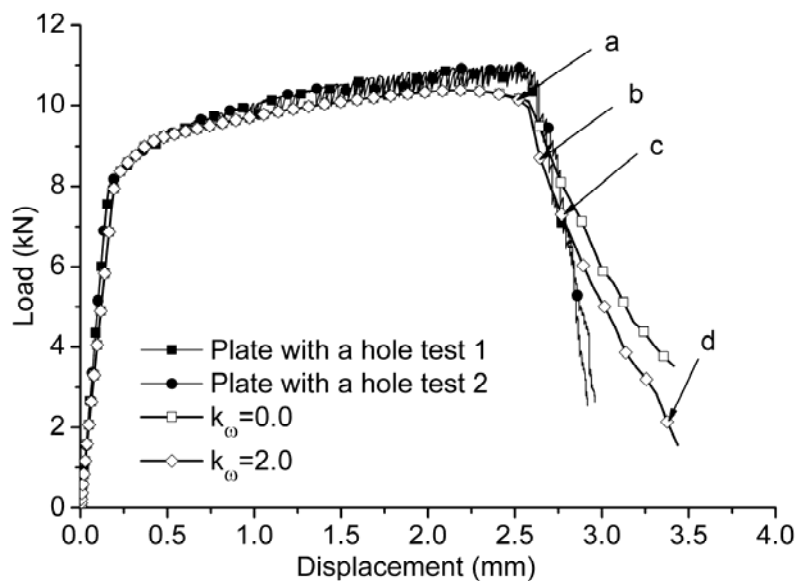


Figure 5-15 The comparison of experiments and simulations for center hole sample. |

5.4.2 Sandia test

Figure 5-16 is the schematic of Sandia benchmark test. There is a notch A and three holes near the notch, try to find the crack path and verify the applicability of ductile fracture model.

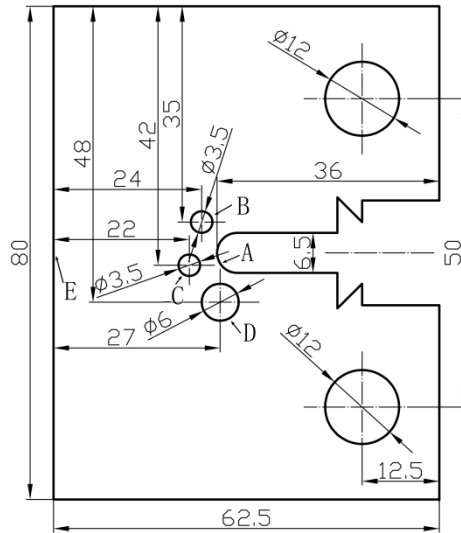


Figure 5-16 The schematic of Sandia benchmark test.

The simulation boundary conditions are shown in Figure 5-17. The element type is C3D8R. There are nine elements along the thickness. The simulation and experimental results are shown in Figure 5-18.

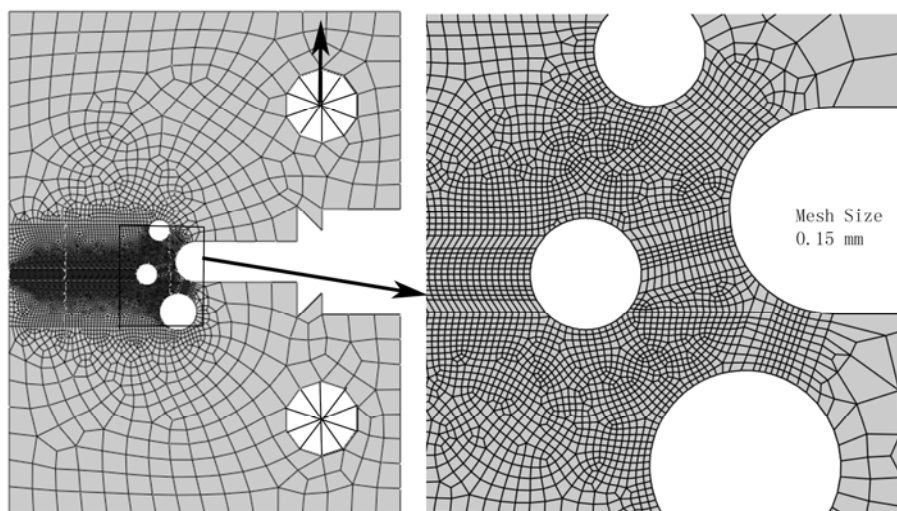


Figure 5-17 The simulation condition of Sandia benchmark test.

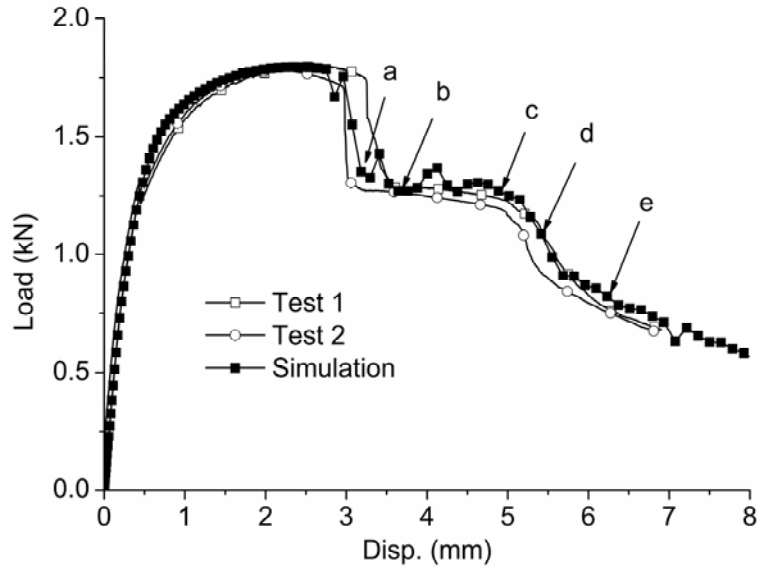


Figure 5-18 The experimental and simulation curves.

The crack progress are shown in Figure 5-19, indicating path A-C-E. The fracture between notch A and hole C, corresponding to the declines at (a) point in load curve. The second crack occurs at the left part of hole C.

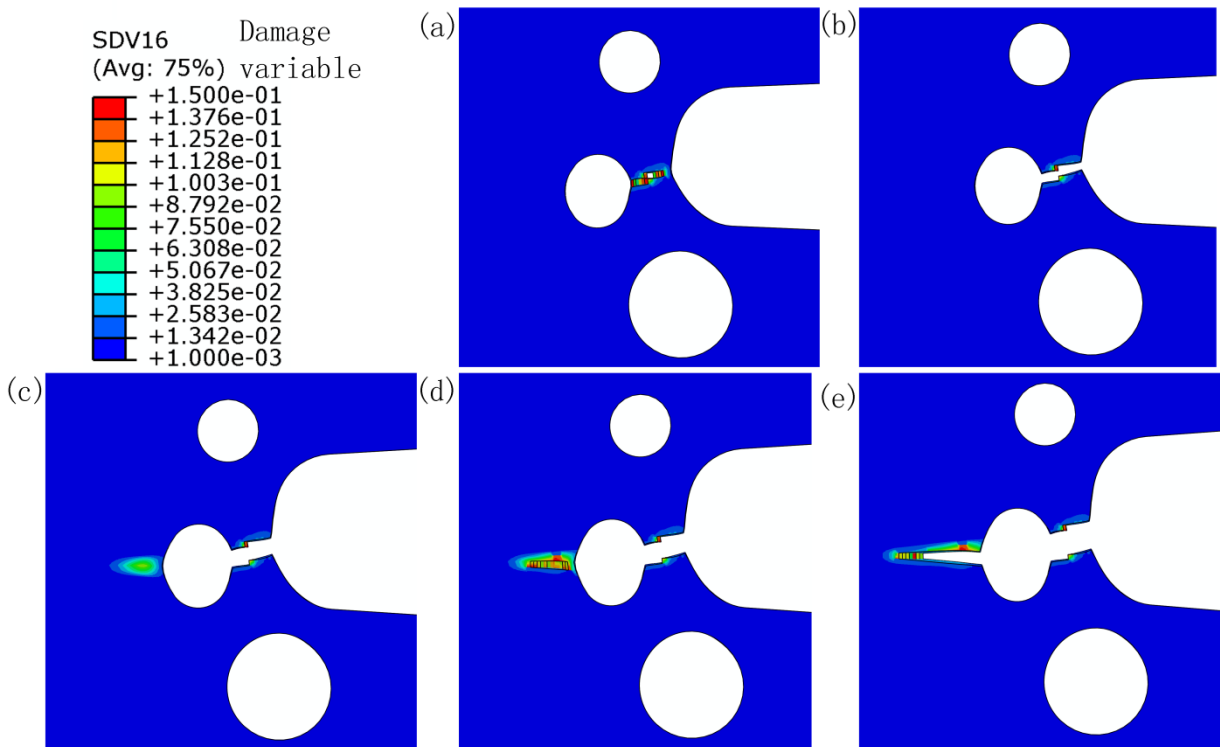


Figure 5-19 The crack process obtained form FEA.

The comparison of simulation and tests are shown in Figure 5-20, and agreement can be found.

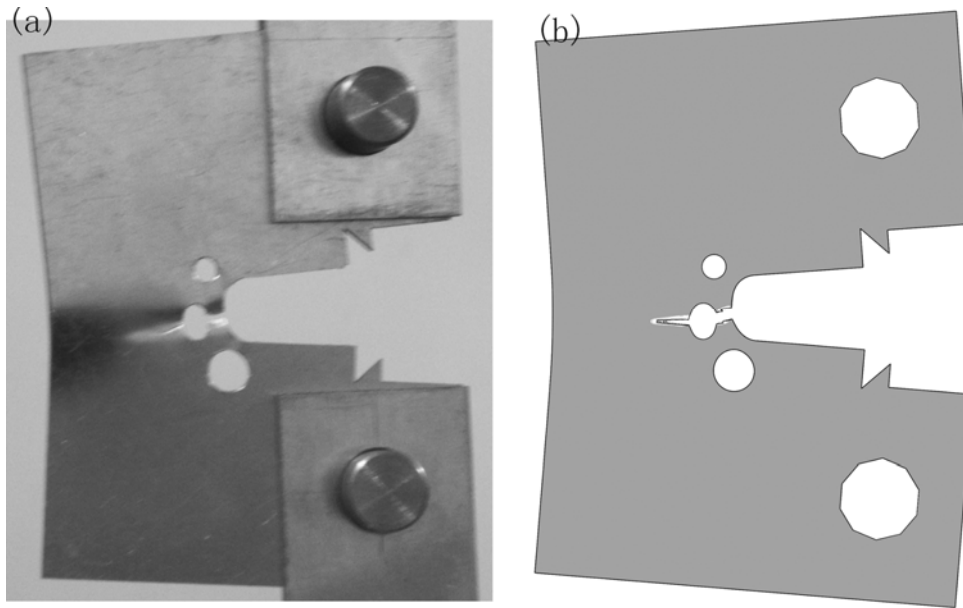


Figure 5-20 The comparison of experiment and simulation for Sandia test sample.

5.5 Brief summary

The fracture mode and mechanism of Al-alloy 5052P-H34 were investigated by physical experiments and numerical simulations.

1. The fracture feature under different load was briefly analyzed. The results show that damage mechanism influenced by geometry of the sample.

2. By a finite element based inverse method, the material constants were obtained. The voce type hardening model was employed as $R(p) = A - (A - B)\exp(-Cp)$, $A = 264.5$ MPa, $B = 182.8$ MPa, $C = 24.51$. The extend hardening modulus was determined as 66.25 MPa. The initial void volume fraction f_0 is calibrated as 0.001 by a fixed $f_c = 0.15$. The shear damage coefficient was calibrated as $k_o = 2.0$ by a new type of shear test.

3. The simulation results show that the modified model can give more accurate results for both of the tension and shear type failure. So, the predictive ability of the modified model was improved

by the shear coefficient k_{ϕ} .

4. The simulation results for Sandia test show that the modified model can predict crack initiation and propagation in complex structure.

Chapter 6 Conclusions and future work

6.1 Main conclusions

In this chapter, a brief summary of the whole research and major conclusions obtained in this study are given.

1. A modified Rousselier model is proposed by using a recent extended damage evolution law considering Lode parameter $\omega(\underline{\underline{\sigma}})$ with a shear coefficient k_{ω} . The new damage evolution rule by considering possible link-up of nearby voids under shear stress is discussed.

2. The analytical solution of the modified model under specific loading is obtained. The applicability of this model on tension and shear is discussed by analyzing the deformation behavior of metal with voids. The physical meaning is interpreted in theory of probability as: for any unit plastic strain, the possibility for shear link-up of nearby voids is $k_{\omega}\omega(\underline{\underline{\sigma}})$.

3. The numerical implementation aspect of modified Rousselier model is performed. The stress integration algorithm based on the return mapping method is developed and implemented into finite element models using the user defined material subroutine VUMAT in the ABAQUS/Explicit platform. The benchmark simulations are conducted to verify the material subroutine and good agreement between analytical solutions mentioned above were achieved.

4. The fracture mechanism of Al-alloy 5052BD-H14 were studied by experiments and numerical simulations. The fracture mechanism under tension is void nucleation, growth, coalescence, while for shear is growth and shear link-up. The material constants and damage related parameters are calibrated by the user defined VUMAT subroutine and physical experiments. The

hardening function is determined as a Voce type as $R(\bar{\varepsilon}^p) = 272.2 - 62.6 \exp(-38.81\bar{\varepsilon}^p)$. The material constants σ_r is calibrated as 180 MPa. The initial void volume fraction is determined by a finite element based inverse method as $f_0 = 10^{-4}$, while the critical void volume fraction as 0.15. The shear damage coefficient is also calibrated as $k_\omega = 1.5$ by a new type of shear test setup. The predictive capability of this model was carried out by studying the cup-cone fracture mode in the tensile tests. The validity of this model was verified by comparing the experiments with the simulations and good agreement was achieved. The results show that the new damage evolution function which is influenced by the metric of the stress can describe the void evolution mechanisms under shear deformation. The applicability of the constitutive model is improved for both tension and shear failure by the new material parameter k_ω .

5. The fracture mode and mechanism of Al-alloy 5052P-H34 were investigated by physical experiments and numerical simulations. The fracture feature under different load was briefly analyzed. The results show that damage mechanism influenced by geometry of the sample, when the same loading is applied. By a finite element based inverse method, the material constants were obtained. The voce type hardening model was employed as $R(\bar{\varepsilon}^p) = A - (A - B) \exp(-C\bar{\varepsilon}^p)$, $A = 264.5$ MPa, $B = 182.8$ MPa, $C = 24.51$. The extend hardening modulus was determined as 66.25 MPa. The initial void volume fraction f_0 is calibrated as 0.001 by a fixed $f_c = 0.15$. The shear damage coefficient was calibrated as $k_\omega = 2.0$. The Sandia crack tests was performed to verify the applicability of the modified model. Both the crack initiation, propagation and path can be predicted by the modified model.

6. The simulation results show that the modified model can give more accurate results for both of the tension and shear type failure. So, the predictive ability of the modified model was improved

by the shear coefficient k_{ϕ} .

6.2 Future work

Although some work has been done, the future work can be focused on the following aspects.

1. The proposed damage model can only predict tension and shear failure, while the applicability on *compression* is still unclear. Special attention has been taken to such failure mode. More detailed researches by considering Lode angle and mean stress should be carried out, to verify the modified model.
2. Maybe, it is difficult to handle various fracture mode solely by CDM, which is abstracted from the idea of metal consistency. More attention will be taken to soil or concrete mechanics and metallography, in which some latest ideas are helpful.
3. The fracture mechanism discussed in this paper is the behavior of the voids in porous metal. The shape of voids is always assumed as spherical or ellipsoidal in the former researches although it is variety. In the modified Rousselier model, the shape of void is neglected and nucleation law can be interpreted by probability theory. So, in the future, a better constitutive law could be proposed in probability theory which is independent of void shape or quantity, rather than empirical analysis.
4. Some wrong results may be obtained when the element deletion method is employed in compression simulations. The discontinuity among material points show its drawback as it has been proposed. The ideal methodology is Extended Finite Element Method(XFEM), however, can not be used for porous material. The combination of XFEM and CDM may be a better way.

References

1. Meyers, M.A. and K.K. Chawla, *Mechanical Behavior of Materials*. 2008, New York: Cambridge University Press.
2. Hooputra, H., et al., *A comprehensive failure model for crashworthiness simulation of aluminium extrusions*. International Journal of Crashworthiness, 2004. **9**(5): p. 449-464.
3. Besson, J., *Continuum Models of Ductile Fracture: A Review*. International Journal of Damage Mechanics, 2009. **19**(1): p. 3-52.
4. Lemaitre, J., ed. *Handbook of Materials Behavior Models*. Vol. 2. 2001, Academic Press: San Diego.
5. Yu, M.-H., et al., *Advances in Unified Strength Theory and its Generalization*. Procedia Engineering, 2011. **10**: p. 2508-2513.
6. Xue, L., *Ductile Fracture Modeling-Theory Experimental Investigation and Numerical Verification*. 2007, Massachusetts Institute of Technology Massachusetts.
7. Li, H., et al., *Ductile fracture: Experiments and computations*. International Journal of Plasticity, 2011. **27**(2): p. 147-180.
8. McClintock, F., S. Kaplan, and C. Berg, *Ductile fracture by hole growth in shear bands*. International Journal of Fracture Mechanics 1966. **2**(4): p. 614-627.
9. McClintock, F.A., *A Criterion for Ductile Fracture by the Growth of Holes*. Journal of Applied Mechanics, 1968. **35**(2): p. 363-371.
10. Rice, J.R. and D.M. Tracey, *On the ductile enlargement of voids in triaxial stress fields*. Journal of the Mechanics and Physics of Solids, 1969. **17**(3): p. 201-217.
11. Gurson, A.L., *Continuum theory of ductile rupture by void nucleation and growth. Part I. Yield criteria and flow rules for porous ductile media*. Journal of Engineering Materials Technology, 1975. **99**: p. 2-15.
12. Lemaitre, J. and R. Desmorat, *Engineering damage mechanics*. 2005, New York:: Springer.
13. Rousselier, G., *Ductile fracture models and their potential in local approach of fracture*. Nuclear Engineering and Design, 1987. **105**(1): p. 97-111.
14. Bao, Y. and T. Wierzbicki, *On fracture locus in the equivalent strain and stress triaxiality space*. International Journal of Mechanical Sciences, 2004. **46**(1): p. 81-98.
15. Wierzbicki, T., et al., *Calibration and evaluation of seven fracture models*. International Journal of

- Mechanical Sciences, 2005. **47**(4-5): p. 719-743.
16. Bai, Y. and T. Wierzbicki, *A new model of metal plasticity and fracture with pressure and Lode dependence*. International Journal of Plasticity, 2008. **24**(6): p. 1071-1096.
 17. Teng, X., *Numerical prediction of slant fracture with continuum damage mechanics*. Engineering Fracture Mechanics, 2008. **75**(8): p. 2020-2041.
 18. Lin, J., L.C. Chan, and L. Wang, *Prediction of forming limit diagrams based on shear failure criterion*. International Journal of Solids and Structures, 2010. **47**(21): p. 2855-2865.
 19. Morgeneyer, T.F. and J. Besson, *Flat to slant ductile fracture transition: Tomography examination and simulations using shear-controlled void nucleation*. Scripta Materialia, 2011. **65**(11): p. 1002-1005.
 20. Nahshon, K. and J.W. Hutchinson, *Modification of the Gurson Model for shear failure*. European Journal of Mechanics - A/Solids, 2008. **27**(1): p. 1-17.
 21. Cockcroft, M.G. and D.J. Latham, *Ductility and workability of metals*. Journal of the Institute of Metals, 1968. **96**: p. 33-39.
 22. Oyane, M., *Criteria of ductile fracture strain*. Bull. JSME, 1972. **15**: p. 1507–1513.
 23. Ayada, M., T. Higashino, and K. Mori. *Central bursting in extrusion of inhomogeneous materials*. in *Proceedings of the First ICTP*. 1984.
 24. Johnson, G.R. and W.H. Cook, *Fracture characteristics of three metals subjected to various strains, strain rates, temperatures and pressures*. Engineering Fracture Mechanics, 1985. **21**(1): p. 31-48.
 25. Takuda, H., K. Mori, and N. Hatta, *The application of some criteria for ductile fracture to the prediction of the forming limit of sheet metals*. Journal of materials processing technology, 1999. **95**(1): p. 116-121.
 26. Reyes, A., et al., *Assessment of yield and fracture criteria using shear and bending tests*. Materials & Design, 2009. **30**(3): p. 596-608.
 27. Fagerholt, E., et al., *Experimental and numerical investigation of fracture in a cast aluminium alloy*. International Journal of Solids and Structures, 2010. **47**(24): p. 3352-3365.
 28. Tvergaard, V. and A. Needleman, *Analysis of the cup-cone fracture in a round tensile bar*. Acta Metallurgica, 1984. **32**(1): p. 157-169.
 29. Gao, X., et al., *Ductile tearing in part-through cracks: experiments and cell-model predictions*. Engineering Fracture Mechanics, 1998. **59**(6): p. 761-777.
 30. Gullerud, A.S., et al., *Simulation of ductile crack growth using computational cells: numerical aspects*. Engineering Fracture Mechanics, 2000. **66**(1): p. 65-92.

31. Zhang, Z.L., C. Thaulow, and J. Ødegård, *A complete Gurson model approach for ductile fracture*. Engineering Fracture Mechanics, 2000. **67**(2): p. 155-168.
32. Xue, Z., et al., *Calibration procedures for a computational model of ductile fracture*. Engineering Fracture Mechanics, 2010. **77**(3): p. 492-509.
33. Lievers, W.B., A.K. Pilkey, and D.J. Lloyd, *Using incremental forming to calibrate a void nucleation model for automotive aluminum sheet alloys*. Acta Materialia, 2004. **52**(10): p. 3001-3007.
34. Oh, C.-K., et al., *A phenomenological model of ductile fracture for API X65 steel*. International Journal of Mechanical Sciences, 2007. **49**(12): p. 1399-1412.
35. Tasan, C.C., J.P.M. Hoefnagels, and M.G.D. Geers, *Identification of the continuum damage parameter: An experimental challenge in modeling damage evolution*. Acta Materialia, 2012. **60**(8): p. 3581-3589.
36. Zhang, T., et al., *Application of the Plasticity Models That Involve Three Stress Invariants*. International Journal of Applied Mechanics, 2012. **04**(02): p. 1250021.
37. Han, W. and B.D. Reddy, *Plasticity, Mathematical Theory and Numerical Analysis*. 1999, Verlag New York, Inc.: Springer.
38. Lubliner, J., *Plasticity Theory*. 2006, University of California at Berkeley: Pearson Education, Inc.
39. Wu, H.-C., *Continuum Mechanics and Plasticity*. 2004, New York: A CRC Press Company.
40. Bridgman, P.W., *Studies in Large Plastic Flow and Fracture With Special Emphasis on the Effects of Hydrostatic Pressure*. 1952, New York: McGraw-Hill.
41. Wilson, C.D., *A Critical Reexamination of Classical Metal Plasticity*. Journal of Applied Mechanics, 2002. **69**(1): p. 63.
42. Richmond, O. and W.A. Spitzig. *Pressure Dependence and Dilatancy of Plastic Flow*. in *International Union of Theoretical and Applied Mechanics Conference Proceedings*. 1980.
43. Drucker, D.C. and W. Prager, *Soil Mechanics and Plastic Analysis for Limit Design*. Quarterly of Applied Mathematics, 1952. **10**: p. 157-165.
44. Malcher, L., F.M. Andrade Pires, and J.M.A. César de Sá, *An assessment of isotropic constitutive models for ductile fracture under high and low stress triaxiality*. International Journal of Plasticity, 2012. **30-31**: p. 81-115.
45. Gao, X., et al., *On stress-state dependent plasticity modeling: Significance of the hydrostatic stress, the third invariant of stress deviator and the non-associated flow rule*. International Journal of Plasticity, 2011. **27**(2): p. 217-231.

46. Bao, Y. and T. Wierzbicki, *A Comparative Study on Various Ductile Crack Formation Criteria*. Journal of Engineering Materials and Technology, 2004. **126**(3): p. 314.
47. Xue, L., *Damage accumulation and fracture initiation in uncracked ductile solids subject to triaxial loading*. International Journal of Solids and Structures, 2007. **44**(16): p. 5163-5181.
48. Xue, L. and T. Wierzbicki, *Ductile fracture initiation and propagation modeling using damage plasticity theory*. Engineering Fracture Mechanics, 2008. **75**(11): p. 3276-3293.
49. Xue, L. and T. Wierzbicki, *Ductile fracture characterization of aluminum alloy 2024-t351 using damage plasticity theory*. International Journal of Applied Mechanics, 2009. **1**: p. 267–304.
50. Rousselier, G., *Dissipation in porous metal plasticity and ductile fracture*. Journal of the Mechanics and Physics of Solids, 2001. **49**(8): p. 1727-1746.
51. Guo, J., et al., *Experimental and numerical investigation for ductile fracture of Al-alloy 5052 using modified Rousselier model*. Computational Materials Science, 2013. **71**: p. 115-123.
52. Voce, E., *A Practical Strain Hardening Function*. Metallurgia, 1955. **51**: p. 219-226.
53. Besson, J., D. Steglich, and W. Brocks, *Modeling of crack growth in round bars and plane strain specimens*. International Journal of Solids and Structures, 2001. **38**(46–47): p. 8259-8284.
54. WILSIUS, J., *Void growth and damage models for predicting ductile fracture in welds*. Fatigue Fract Engng Mater Struct, 1999. **23**: p. 105-112.
55. Besson, J., D. Steglich, and W. Brocks, *Modeling of plane strain ductile rupture*. International Journal of Plasticity, 2003. **19**(10): p. 1517-1541.
56. Tvergaard, V., *On localization in ductile materials containing spherical voids*. International Journal of Fracture, 1982. **18**: p. 237-252.
57. Nahshon, K. and Z. Xue, *A modified Gurson model and its application to punch-out experiments*. Engineering Fracture Mechanics, 2009. **76**(8): p. 997-1009.
58. Gruben, G., O.S. Hopperstad, and T. Børvik, *Simulation of ductile crack propagation in dual-phase steel*. International Journal of Fracture, 2012.
59. J.C. Simo, T.J.R.H., *Computational Inelasticity (Interdisciplinary Applied Mathematics)*. 1998, New York: Springer.
60. Dunne, F. and N. Petrinic, *Introduction to Computational Plasticity*. 2005, New York: Oxford University.
61. Neto, E.d.S., D. Peric, and D. Owen, *Computational Methods for Plasticity Theory and Applications*. 2008, United Kingdom: John Wiley & Sons Ltd.

62. Lee, H.C., et al., *Application of element deletion method for numerical analyses of cracking*. Journal of Achievements in Materials and Manufacturing Engineering, 2009. **35**: p. 154-161.
63. HKS, *Abaqus User Subroutines Reference Manual*. 2010: Dassault Systèmes Simulia Corp.
64. HKS, *Abaqus Theory Manual*. 2010: Dassault Systèmes Simulia Corp.
65. Mediavilla, J., R.H.J. Peerlings, and M.G.D. Geers, *A robust and consistent remeshing-transfer operator for ductile fracture simulations*. Computers & Structures, 2006. **84**(8-9): p. 604-623.
66. Achouri, M., et al., *Numerical integration of an advanced Gurson model for shear loading: Application to the blanking process*. Computational Materials Science, 2013. **72**: p. 62-67.
67. Bai, Y. and T. Wierzbicki, *Application of extended Mohr–Coulomb criterion to ductile fracture*. International Journal of Fracture, 2009. **161**(1): p. 1-20.
68. Barsoum, I. and J. Faleskog, *Rupture mechanisms in combined tension and shear—Experiments*. International Journal of Solids and Structures, 2007. **44**(6): p. 1768-1786.
69. Ghahremaninezhad, A. and K. Ravi-Chandar, *Ductile failure behavior of polycrystalline Al 6061-T6 under shear dominant loading*. International Journal of Fracture, 2013.
70. Luo, M., M. Dunand, and D. Mohr, *Experiments and modeling of anisotropic aluminum extrusions under multi-axial loading – Part II: Ductile fracture*. International Journal of Plasticity, 2012. **32-33**: p. 36-58.

Acknowledgement

I would like to take this opportunity to express my sincere gratitude to my advisors Prof. Dr. Ri-ichi Murakami from the University of Tokushima and Prof. Dr. Shengdun Zhao from Xi'an Jiaotong University for their encouragements, consistent help and their valuable instructions in the academic area. The accomplishment of this degree would be impossible without their supports and guidance. The special appreciation is given to Dr. Shunlai Zang for his time on reading and evaluating my thesis. Their comments and suggestions have improved the quality of my research work.

I would like to thank my colleagues, including Dongyan Zhang, Pangpang Wang, Jingxiang Li, Bo Wu, Xiaobo Zhang and others during the past years of my PhD life. Here, I would also like to thank all of the people who have supported me and helped me. Especially thanks to Kai Zhang for introduction of Lode parameter and simulation ideas in Abaqus software. Discussions on the academic issues with them always enlightened me to approach the research objectives.

Secondly, I would like to thank the Double Degree Program between the University of Tokushima and Xi'an Jiaotong University for their financial supports. I would like to thank all the members in CICEE, Ms. Asada Sawa, Dr. Pankaj Koinka, and Dr. Walter Carpenter, for taking care of my administrative issues during those years. Special appreciation is given to our Japanese language teacher Kohno Nayoko and her husband.

Finally, I want to thank my parents for their endless love and support. Especially, thanks my wife for her love and accompanying.

Publications

Journals

1. Junhang Guo, Shengdun Zhao, Ri-ichi Murakami, and Shunlai Zang, Experimental and numerical investigation for ductile fracture of Al-alloy 5052 using modified Rousselier model. *Comput. Mater. Sci.* 71, 115-123(2013).
2. Junhang Guo, Shengdun Zhao, Ri-ichi Murakami, Rixian Ding and Shuqin Fan, Modeling the hot deformation behavior of Al alloy 3003. *J. Alloys Compd.*, (2013).

International Conferences

1. Junhang Guo, Ri-ichi Murakami, and Shengdun Zhao, A New Constitutive Model for Anisotropic Sheet Metal with Isotropic Ductile Damage, *Advanced Materials Research*, Vols. 291-294 (2011) pp 1154-1160, The 2nd International Conference on Advanced Engineering Materials and Technology, July 29-30, 2011, Sanya, China (oral)
2. Junahang Guo, Ri-ichi Murakami, and Shengdun Zhao, A Study On Experiments And Simulations For Ductile Fracture Of Isotropic Material Using Rousselier's Damage Model, the 6th international Conference on Advanced Materials Development and Performance, July 15-18, 2011, Tokushima, Japan (oral).
3. Junhang Guo, Shengdun Zhao and Ri-ichi Murakami, Simulation of Ductile Fracture in an Aluminum Alloy Using Various Criteria, *Advanced Materials Research*, Vols. 560-561 (2012) pp 973-978, 2012 Spring World Congress on Engineering and Technology, May 27-30, 2012, Xi'an, China (oral)